ISSN 2074-272X

науково-практичний журнал 2021/6

Електротехніка і Електромеханіка

Electrical Engineering & Electromechanics

Інженерна електрофізика.
Техніка сильних електричних та магнітних полів
Електричні машини та апарати
Електротехнічні комплекси та системи
Електроізоляційна та кабельна техніка
Електричні станції, мережі і системи

Журнал включено до найвищої категорії «А» Переліку фахових видань України

29 липня 2021 р. отримано позитивне рішення щодо включення журналу до Scopus

З 2015 р. журнал індексується у Web of Science Core Collection: Emerging Sources Citation Index

Electrical Engineering & Electromechanics

Scientific Journal was founded in 2002
Founders are:
National Technical University «Kharkiv Polytechnic Institute» (Kharkiv, Ukraine)
State Institution «Institute of Technical Problems of Magnetism of the NAS of Ukraine» (Kharkiv, Ukraine)

29th of July 2021 Journal «Electrical Engineering & Electromechanics» has been accepted for Scopus.

Journal «Electrical Engineering & Electromechanics» from no. 1 2015 is indexing in Web of Science Core Collection : Emerging Sources Citation Index (ESCI).

Also included in DOAJ (Directory of Open Access Journals), in EBSCO's database, in ProQuest's databases – Advanced Technologies & Aerospace Database and Materials Science & Engineering Database, in Gale/Cengage Learning databases.

Editorial office address:
National Technical University «Kharkiv Polytechnic Institute», Kyrpychova Str., 2, Kharkiv, 61002, Ukraine
phones: +380 57 7076281, +380 67 3594696, **e-mail:** a.m.grechko@gmail.com (**Grechko O.M.)**

ISSN (print) 2074-272X
ISSN (online) 2309-3404

Printed 03 December 2021. Format 60 × 90 ⅛. Paper – offset. Laser printing. Edition 200 copies.
Printed by Printing house «Madrid Ltd» (18, Gudanova Str., Kharkiv, 61024, Ukraine)

Electrical Engineering & Electromechanics
Scientific Journal

no. 6, 2021

Table of Contents

UDC 621.313:536.2.24:539.2 https://doi.org/10.20998/2074-272X.2021.6.01

V.F. Bolyukh, I.S. Shchukin

Influence of limiting the duration of the armature winding current on the operating indicators of a linear pulse electromechanical induction type converter

Introduction. *Linear pulse electromechanical converters of induction type (LPECIT) are used in many branches of science and technology as shock-power devices and electromechanical accelerators. In them, due to the phase shift between the excitation current in the inductor winding and the induced current in the armature winding, in addition to the initial electrodynamic forces (EDF) of repulsion, subsequent EDF of attraction also arise. As a result, the operating indicators of LPECIT are reduced.* ***The purpose*** *of the article is to increase the performance of linear pulse electromechanical induction-type converters when operating as a shock-power device and an electromechanical accelerator by limiting the duration of the induced current in the armature winding until its polarity changes.* ***Methodology.*** *To analyze the electromechanical characteristics and indicators of LPECIT, a mathematical model was used, in which the solutions of equations describing interrelated electrical, magnetic, mechanical and thermal processes are presented in a recurrent form.* ***Results.*** *To eliminate the EDF of attraction between the LPIECIT windings, it is proposed to limit the duration of the induced current in the armature winding before changing its polarity by connecting a rectifier diode to it. It was found that when the converter operates as a shock-power device without limiting the armature winding current, the value of the EDF pulse after reaching the maximum value decreases by the end of the operating cycle. In the presence of a diode in the armature winding, the efficiency criterion, taking into account the EDF pulse, recoil force, current and heating temperature of the inductor winding, increases. When the converter operates as an electromechanical accelerator without limiting the armature winding current, the speed and efficiency decrease, taking into account the kinetic energy and voltage of the capacitive energy storage at the end of the operating cycle. In the presence of a diode in the armature winding, the efficiency criterion increases, the temperature rise of the armature winding decreases, the value of the maximum efficiency increases, reaching 16.16 %.* ***Originality****. It has been established that due to the limitation of the duration of the armature winding current, the power indicators of the LPECIT increase when operating as a shock-power device and the speed indicators when the LPECIT operates as an electromechanical accelerator.* ***Practical value.*** *It was found that with the help of a rectifier diode connected to the multi-turn winding of the armature, unipolarity of the current is ensured, which leads to the elimination of the EDF of attraction and an increase in the performance of the LPECIT.* References 22, figures 5.

Key words: **linear pulse electromechanical converter of induction type, shock-power device, electromechanical accelerator, performance indicators, limiting the duration of the armature winding current.**

Вступ. *Лінійні імпульсні електромеханічні перетворювачі індукційного типу (ЛІЕПІТ) використовуються в багатьох галузях науки і техніки як ударно-силові пристрої та електромеханічні прискорювачі. У них через фазовий зсув між струмом збудження в обмотці індуктора і індукованим струмом в обмотці якоря крім початкових електродинамічних сил (ЕДС) відштовхування виникають і наступні ЕДС тяжіння. Внаслідок цього робочі показники ЛІЕПІТ знижуються.* ***Метою*** *статті є підвищення робочих показників лінійних імпульсних електромеханічних перетворювачів індукційного типу при роботі в якості ударно-силового пристрою та електромеханічного прискорювача за рахунок обмеження тривалості індукованого струму в обмотці якоря до зміни його полярності.* ***Методика.*** *Для аналізу електромеханічних характеристик та показників ЛІЕПІТ використана математична модель, в якій розв'язки рівнянь, що описують взаємопов'язані електричні, магнітні, механічні та теплові процеси, представлені в рекурентному вигляді.* ***Результати.*** *Для усунення ЕДС тяжіння між обмотками ЛІЕПІТ запропоновано обмеження тривалості індукованого струму в обмотці якоря до зміни його полярності шляхом підключення до неї випрямного діода. Встановлено, що при роботі перетворювача в якості ударно-силового пристрою без обмеження струму обмотки якоря величина імпульсу ЕДС після досягнення максимального значення знижується до кінця робочого циклу. За наявності діода в обмотці якоря критерій ефективності, що враховує імпульс ЕДС, силу віддачі, струм і температуру нагрівання обмотки індуктора, підвищується. При роботі перетворювача в якості електромеханічного прискорювача без обмеження струму обмотки якоря відбувається зменшення швидкості і ККД, що враховує кінетичну енергію і напругу ємнісного накопичувача енергії в кінці робочого циклу. За наявності діода в обмотці якоря критерій ефективності підвищується, перевищення температури обмотки якоря зменшується, величина максимального ККД збільшується, досягаючи 16,16 %.* ***Наукова новизна.*** *Встановлено, що за рахунок обмеження тривалості струму обмотки якоря підвищуються силові показники ЛІЕПІТ при роботі в якості ударно-силового пристрою та швидкісні показники при роботі ЛІЕПІТ в якості електромеханічного прискорювача.* ***Практична цінність.*** *Встановлено, що за допомогою випрямного діода, підключеного до багатовиткової обмотки якоря, забезпечується однополярність струму, що зумовлює усунення ЕДС тяжіння і підвищення робочих показників ЛІЕПІТ.* Бібл. 22, рис. 5.

Ключові слова: **лінійний імпульсний електромеханічний перетворювач індукційного типу, ударно-силовий пристрій, електромеханічний прискорювач, робочі показники, обмеження тривалості струму обмотки якоря.**

Введение. *Линейные импульсные электромеханические преобразователи индукционного типа (ЛИЭПИТ) используются во многих отраслях науки и техники в качестве ударно-силовых устройств и электромеханических ускорителей. В них из-за фазового сдвига между током возбуждения в обмотке индуктора и индуцированным током в обмотке якоря помимо первоначальных электродинамических усилий (ЭДУ) отталкивания возникают и последующие ЭДУ притяжения. Вследствие этого рабочие показатели ЛИЭПИТ снижаются.* ***Целью статьи*** *является повышение рабочих показателей линейных импульсных электромеханических преобразователей индукционного типа при работе в качестве ударно-силового устройства и электромеханического ускорителя за счет ограничения длительности индуцированного тока в обмотке якоря до изменения его полярности.* ***Методика.*** *Для анализа электромеханических характеристик и показателей ЛИЭПИТ*

использована математическая модель, в которой решения уравнений, описывающих взаимосвязанные электрические, магнитные, механические и тепловые процессы, представлены в рекуррентном виде. ***Результаты.*** *Для устранения ЭДУ притяжения между обмотками ЛИЭПИТ предложено ограничение длительности индуцированного тока в обмотке якоря до изменения его полярности путем подключения к ней выпрямительного диода. Установлено, что при работе преобразователя в качестве ударно-силового устройства без ограничения тока обмотки якоря величина импульса ЭДУ после достижения максимального значения снижается к концу рабочего цикла. При наличии диода в обмотке якоря критерий эффективности, учитывающий импульс ЭДУ, силу отдачи, ток и температуру нагрева обмотки индуктора, повышается. При работе преобразователя в качестве электромеханического ускорителя без ограничения тока обмотки якоря происходит уменьшение скорости и КПД, учитывающего кинетическую энергию и напряжение емкостного накопителя энергии в конце рабочего цикла. При наличии диода в обмотке якоря критерий эффективности повышается, превышение температуры обмотки якоря уменьшается, величина максимального КПД увеличивается, достигая 16,16 %.* ***Научная новизна.*** *Установлено, что за счет ограничения длительности тока обмотки якоря повышаются силовые показатели ЛИЭПИТ при работе в качестве ударно-силового устройства и скоростные показатели при работе ЛИЭПИТ в качестве электромеханического ускорителя.* ***Практическая ценность.*** *Установлено, что при помощи выпрямительного диода, подключенного к многовитковой обмотке якоря, обеспечивается однополярность тока, что приводит к устранению ЭДУ притяжения и повышению рабочих показателей ЛИЭПИТ.* Библ. 22, рис. 5.
Ключевые слова: **линейный импульсный электромеханический преобразователь индукционного типа, ударно-силовое устройство, электромеханический ускоритель, рабочие показатели, ограничение длительности тока обмотки якоря.**

Introduction. Linear pulse electromechanical converters of induction type (LPECITs) are widely used both for acceleration of an actuator to high speed on a short active site, and for creation of powerful power pulses on object of influence at insignificant movement of an actuator [1-4]. Such converters are widely used in many fields of science and technology as shock-power devices and electromechanical accelerators.

As shock-power devices LPECITs are used for electromagnetic hammers and perforators in construction, for drills and vibrators in the mining industry, for shock seismic sources in exploration, for hammers with a wide range of impact energy and devices for electrodynamic processing of welded joints in mechanical engineering, for vibrating mixers in the chemical and medical-biological industry, for testing devices that provide testing of critical equipment for shock loads, for magnetic-pulse devices that provide pressing of special ceramic powders, for devices that provide cleaning of technological tanks from the adhesion of bulk materials, for devices that ensure the destruction of important information on the drives in case of unauthorized access, etc. [5-9].

As electromechanical accelerators LPECITs are used for high-speed electric devices, for ballistic laser gravimeters, for the systems providing start of unmanned aerial vehicles, for the defensive devices providing protection of responsible objects from the approaching devices, for accelerators in aerospace engineering. etc. [10-15].

In LPECIT, a pulsed current flows in the stationary winding of the inductor when connected to a capacitive energy storage (CES) device which induces a current in the armature winding by means of a magnetic field. Since at the initial moment of time the currents in the windings have the opposite polarity, repulsive electrodynamic forces (EDF) arise between them [16].

When the converter operates as an electromechanical accelerator, the armature winding, which moves under the action of the repulsion EDF, accelerates the actuator. And when operating as a shock-power device, the armature winding with a slight movement provides the transmission of a power pulse to the actuator.

In LPECIT short-circuited armature winding can be made single-turn or multi-turn. In the single-turn design, the armature winding is usually a massive conductive disk. However, the induced current on such a disk is distributed significantly nonuniformly. In the multi-turn design, the armature winding is tightly wound with a wire of relatively small cross section and impregnated with an epoxy-based compound. In such a winding, the induced current is distributed uniformly throughout the cross section, which provides a more uniform force on the actuator.

Studies show that due to the phase shift between the excitation current in the inductor winding and the induced current in the short-circuited armature winding, in addition to the initial repulsion EDF, the following attractive EDF occurs [17]. As a result, the operating performance of the converter is reduced [18]. Attractive EDF occur due to a change in the polarity of the induced current in the armature winding, while the polarity of the excitation current in the inductor winding may remain unchanged.

The attractive EDF can be eliminated by limiting the duration of the induced current in the armature winding before changing its polarity. To do this, it is possible to connect a rectifier diode *VD* to the armature winding (Fig. 1). Current limitation in a magnetic pulse unit to change the effect of EDF on the secondary conductive element using a controlled vacuum discharger is described in [19]. But in that study, the goal was to increase the attractive EDF, whereas for LPECIT such forces are undesirable.

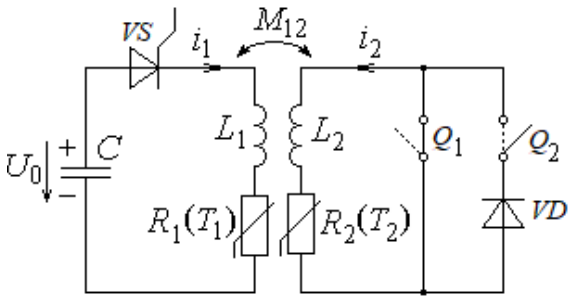

Fig. 1. LPECIT electrical circuit in the absence (Q_1, Q_2 – solid lines) and the presence (Q_1, Q_2 – dashed lines) of the diode *VD* in the armature winding

Ensuring one polarity of the induced current can be realized by connecting the diode *VD* to the multi-turn armature winding, so below we will consider it. However, here the feasibility of limiting the duration of the induced current in the armature winding to change its polarity during the operation of LPECIT as a shock-power device and electromechanical accelerator has not been studied.

The goal of the paper is to increase the performance of linear pulse electromechanical converters of induction type when operating as a shock-power device and electromechanical accelerator by limiting the duration of the induced current in the armature winding to change its polarity.

Consider **the mathematical model** of the LPECIT which uses the lumped parameters of the multi-turn windings of the inductor and armature. To take into account the interconnected electrical, magnetic, mechanical and thermal processes, as well as a number of nonlinear dependencies, the solution of equations describing these processes, are present in recurrent form.

We assume that when operating as a shock-power device, the movement of the armature winding with the actuator is absent, and when operating as an electromechanical accelerator, the armature moves a considerable distance with the actuator, which has a relatively small mass.

To excite LPECIT from CES, we use a unipolar current pulse in the inductor winding formed by the starting thyristor *VS* (Fig. 1). This allows to store some part of the energy in the CES until the end of the operating cycle. To limit the duration of the induced current in the armature winding before changing its polarity, we use a rectifier diode *VD*. We believe that for semiconductor devices *VS* and *VD* the resistance in the forward direction is zero, and in the opposite direction is infinitely large.

Electrical processes in LPECIT when operating as a shock-power device can be described by a system of equations:

$$R_1(T_1)i_1 + L_1\frac{di_1}{dt} + \frac{1}{C_0}\int_0^t i_1 dt + M_{12}\frac{di_2}{dt} = 0, \quad (1)$$

$$\frac{1}{C_0}\int_0^t i_1 \cdot dt = U_0, \quad (2)$$

$$R_2(T_2)\cdot i_2 + L_2\frac{di_2}{dt} + M_{21}\frac{di_1}{dt} = 0, \quad (3)$$

where n = 1, 2 are the indices of the windings of the inductor and armature, respectively; R_n, L_n, T_n, i_n are the active resistance, inductance, temperature and current of the n-th winding, respectively; M_{12}=M_{21} is the mutual inductance between the windings; C_0, U_0 are the capacity and initial (charging) voltage of CES.

When LPECIT operates as an electromechanical accelerator, equations (1), (3) take the form:

$$R_1(T_1)i_1 + L_1\frac{di_1}{dt} + \frac{1}{C_0}\int_0^t i_1 dt + M_{12}(z)\frac{di_2}{dt} + v_z(t)i_2\frac{dM_{12}}{dz} = 0; \quad (4)$$

$$R_2(T_2)\cdot i_2 + L_2\frac{di_2}{dt} + M_{21}(z)\frac{di_1}{dt} + i_1 v(t)\frac{dM_{12}}{dz} = 0. \quad (5)$$

Solutions of the equations for currents in the converter windings in recurrent form are presented in [18]. The displacement h_z and the speed v_z of the armature winding relative to the inductor winding, presented in a recurrent form [10], take into account the instantaneous value of the axial EDF between the windings:

$$f_z(z,t) = i_1(t)i_2(t)\frac{dM_{12}}{dz}(z), \quad (6)$$

the masses of the armature winding and the actuator, the density of the moving medium and the coefficient of drag.

When LPECIT operates as a shock-power device, between the windings there is a thermal contact through the insulating gasket. The temperature of the windings can be described by recurrent relations [4], which take into account the thermal conductivity and the thickness of the gasket, the coefficients of heat transfer and heat capacities of the windings.

To calculate the characteristics and indicators of LPECIT, we use the algorithm of cyclic action [20], which allows to take into account a set of interconnected electrical, magnetic, mechanical and thermal processes and various nonlinear dependencies, such as $R_n(T_n)$, $M_{12}(z)$. When calculating the workflow is divided into a number of numerically small time intervals $\Delta t = t_{k+1} - t_k$, within which all values are considered constant. According to the current values obtained at time t_{k+1}, we calculate the temperature of the windings T_1 and T_2, the displacements h_z and the speed v_z of the armature winding, the mutual inductance M_{12} between the windings. With this approach, linear equations and relations can be used to determine the currents in the calculation time interval Δt. The value of Δt is chosen so that it does not significantly affect the calculation results, while ensuring the required accuracy.

Initial conditions of the mathematical model:
$T_n(0) = T_0$ – the temperature of the n-th winding;
$i_n(0) = 0$ – the current of the n-th winding;
$h_z(0) = h_{z0}$ – the distance between windings;
$u_c(0) = U_0$ – the CES voltage;
$v_z(0) = 0$ – the speed of the armature winding along the z axis.

The main parameters of LPECIT. Consider LPECIT in which the inductor winding (n=1) and the armature winding (n=2) are made in the form of monolithic disk coils, tightly wound with copper wire of circular cross section with diameter d_0=1.3 mm and impregnated with epoxy compound. The outer diameter of the windings D_{ex}=100 mm, their inner diameter D_{in}=10 mm. The axial height of the inductor winding H_1=6 mm and of the armature winding H_2=3 mm. The number of turns of the inductor winding N_1=120 and of the armature winding N_2=60. The initial distance between the windings h_{z0}=1 mm. CES has energy W_0=500 J and its capacitance

C_0 varies in the range from 0.5 to 5 mF with a corresponding change in initial voltage $U_0 = \sqrt{2W_0C_0^{-1}}$. When LPECIT operates as an electromechanical accelerator, the mass of the actuator m_a=0.5 kg.

We analyze the electromechanical characteristics and performance of LPECIT which has in the armature winding limiting the duration of the induced current before changing its polarity (Q_1 open, Q_2 closed), compared with LPECIT which has no such limitation (Q_1 closed, Q_2 open) (see Fig. 1).

When analyzing the operation of LPECIT, we take into account the following operating indicators: excitation current, heating temperature of the windings and recoil force. The maximum excitation current is proportional to the amplitude of the current density in the inductor winding j_{1m}, the heating temperature of the inductor winding – to the rise of its temperature θ_1, and the recoil force – to the amplitude of the EDF f_{zm}. The maximum excitation current affects the parameters of the electronic source, the heating temperature – the duration of the converter operation in cyclic mode, and the recoil force – the mechanical reliability. For example, for hand-held shock instruments and various stand-alone starters, the recoil force has a negative effect on both the device itself and the service personnel. The force of recoil is especially negative in measuring devices. For example, a ballistic laser gravimeter designed to measure the acceleration of free fall uses an electromechanical catapult, which provides a vertical throw of the angular optical reflector [21]. The recoil force causes autoseismic oscillations that reduce the accuracy of the gravimeter's measurement [22].

When LPECIT operates as a shock-power device, its efficiency will be evaluated by the largest value of the EDF impulse $P_z = \int_0^t f_z(t)dt$ at the minimum values of recoil force, excitation current and heating temperature of the inductor winding.

Figure 2 presents the electromechanical characteristics of LPECIT in the absence (solid lines) and the presence (lines with circles) of limiting the duration of the induced current in the armature winding to change its polarity.

When using CES with capacity of C_0 = 0.5 mF the maximum current density in the inductor winding is j_{1m}=1.03 kA/mm^2, and in the armature winding j_{2m}=1.41 kA/mm^2 (Fig. 2,*a*). The amplitude of the EDF f_{zm}=30.85 kN. In the absence of limitation of the induced current in the short-circuited armature winding (without diode *VD* in Fig. 1) by the end of the operating cycle the temperature rise of the inductor winding is θ_1=1.58 °C, and the temperature rise of the armature winding is θ_2=2.87 °C. Due to the attractive EDF, the value of the impulse of these forces, reaching the maximum value P_{zm}=12.5 N·s, by the end of the operating cycle decreases to P_{zf}=12.19 N·s.

When using CES of higher capacity (C_0=2.5 mF), and hence lower voltage U_0, the maximum values of current densities in the inductor winding is reduced to j_{1m}=0.67 kA/mm^2, in the armature winding to j_{2m}=0.78 kA/mm^2, EDF to f_{zm}=10.58 kN (Fig. 2,*b*). But by the end of the operating cycle, the temperature rise of the inductor winding increases to θ_1=2.15 °C, and the temperature rise of the armature winding decreases to θ_2=1.86 °C. The value of the EDF impulse, reaching the maximum value P_{zm}=9.61 N·s, by the end of the operating cycle is reduced to P_{zf}=7.94 N·s.

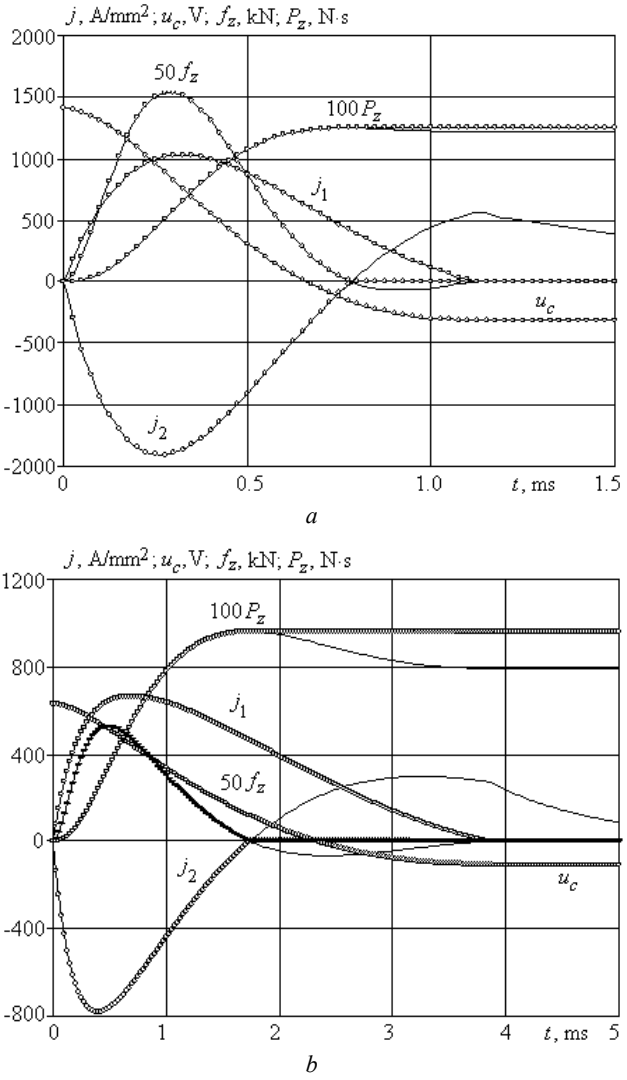

Fig. 2. Electromechanical characteristics of LPECIT when operating as a shock-power device at C_0: 0.5 mF (*a*) and 2.5 mF (*b*)

With increasing capacity C_0 of CES and constant energy W_0=500 J, the voltage U_0 decreases, which causes a change in the main performance of LPECIT (Fig. 3,*a*).

With increasing C_0 from 0.5 to 5 mF, the amplitude of the EDF f_{zm} decreases by about 5 times (from 30.85 to 6.06 kN), but the value of the maximum impulse of the EDF P_{zm} decreases by about 1.5 times (from 12.5 to 7.7 N·s). With such an increase in capacitance C_0, the temperature rise of the inductor winding θ_1 increases from 1.58 to 2.47 °C. These indicators do not practically depend on the presence or absence of limitation of the

duration of the induced current in the armature winding before changing its polarity. However, the limitation of the current duration affects the temperature rise of the armature winding θ_2. In the converter without current limitation of the short-circuited armature winding, the value θ_2 decreases from 2.87 to 1.27 °C. In the presence of the specified limitation due to connection of the diode *VD* the value θ_2 is lower, than in its absence, and decreases from 2.24 to 0.96 °C.

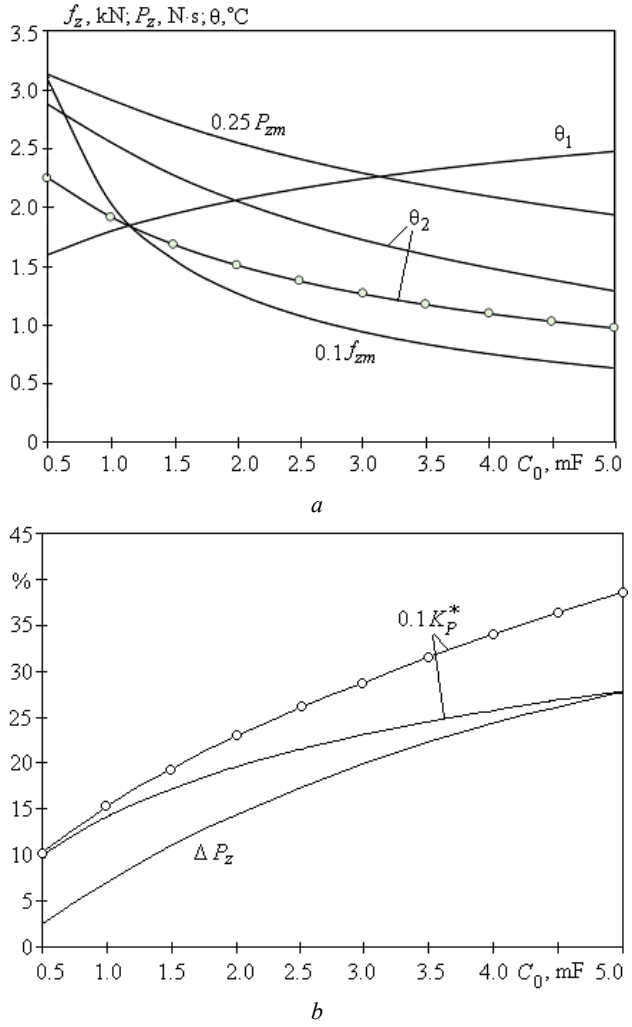

Fig. 3. Dependence of LPECIT performance at operation as a shock-power device on the capacity of CES when W_0=500 J

In order to evaluate the efficiency of LPECIT operation as a shock-power device depending on the value of the capacity C_0 of CES at W_0=500 J we use the value of the relative reduction of the EDF impulse $\Delta P_z = 100\left(P_{zm} - P_{zf}\right)P_{zm}^{-1}, \%$ and the relative criterion of efficiency $K_P^* = 100\dfrac{P_{zf}^*}{j_{1m}^* f_{zm}^* \theta_1^*}, \%$. As a basic variant for K_P^* we use the converter excited from CES with capacity C_0=0.5 mF without current limitation in the short-circuited armature winding. With an increase in C_0 from 0.5 to 5 mF and the absence of current limitation in the armature winding, the relative decrease in the EDF impulse increases from 2.5 to 27.6 % (Fig. 3,*b*). However, the efficiency criterion of LPECIT K_p* increases by 2.78 times primarily due to the reduction of the amplitude of the current density in the inductor winding j_{1m} and the amplitude of the EDF f_{zm}.

If there is imitation of the current duration in the armature winding due to the connection of the diode *VD* due to the absence of EDF impulse decrease, the value of the efficiency criterion K_p* increases (by 38.6 % at C_0=0.5 mF) This shows the prospects of this technical solution at LPECIT operation as a shock-power device.

When LPECIT operates as an electromechanical accelerator, its effectiveness will be evaluated by the highest value of efficiency

$$\eta = 100 C_0^{-1}\left(m_2 + m_a\right)v^2\left(U_0^2 - U_1^2\right)^{-1}, \%,$$

which takes into account the kinetic energy of the armature together with the actuator and the residual voltage of the CES at the end of the operating cycle U_1.

Figure 4 presents the electromechanical characteristics of LPECIT in the absence (solid lines) and the presence (lines with circles) of the limitation of the induced current in the armature winding.

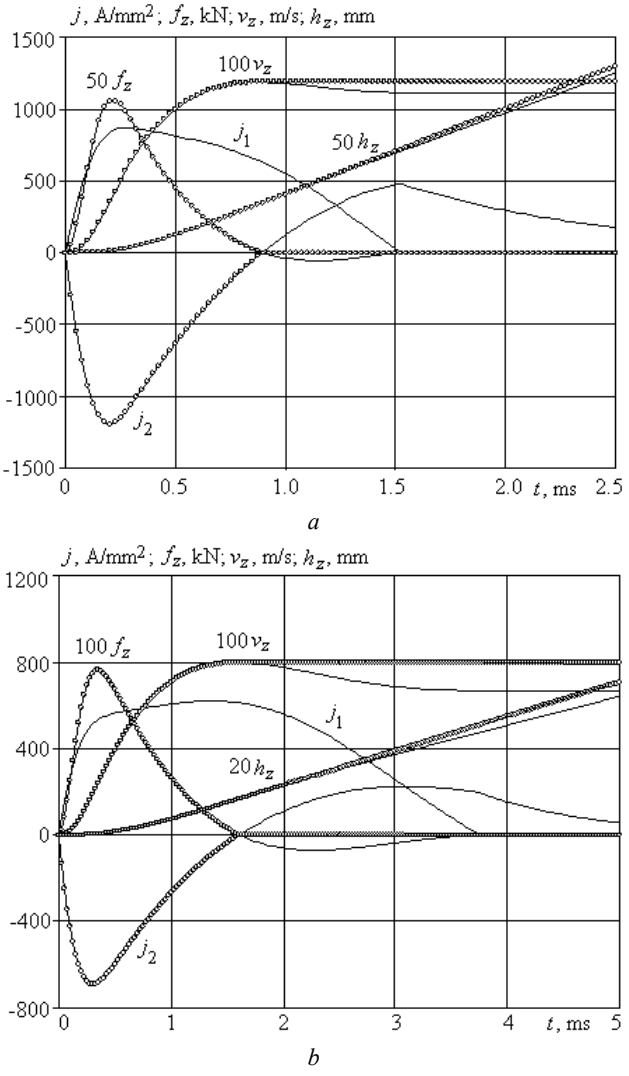

Fig. 4. Electromechanical characteristics of LPECIT at operation as an electromechanical accelerator at C_0: 0.5 mF (*a*) and 2.5 mF (*b*)

When using CES with capacity of C_0=0.5 mF, the maximum current density in the inductor winding is j_{1m}=0.87 kA/mm^2, and in the armature winding is j_{2m}= 1.19 kA/mm^2 (Fig. 4,*a*), i.e. they are lower than when LPECIT operates as a shock-power device. Accordingly, the amplitude of the EDF is smaller: f_{zm}=21.16 kN.

In the converter without current limitation in the short-circuited armature winding, the maximum speed v_m=11.86 m/s by the end of the operating cycle is practically not reduced, which provides the efficiency of the electromechanical accelerator η=14.24 %. The temperature rise of the inductor winding is θ_1=1.84 °C, and the temperature rise of the armature winding θ_2=2.02 °C. When using CES with capacity of C_0=2.5 mF, the maximum value of the current density in the inductor winding is reduced to j_{1m}=0.621 kA/mm^2, and in the armature winding to j_{2m}=0.69 kA/mm^2, EDF to f_{zm}=7.62 kN (Fig. 4,*b*).

By the end of the operating cycle, the temperature rise of the inductor winding increases to θ_1=2.6 °C, and the temperature rise of the armature winding decreases to θ_2=1.12 °C. The speed of the armature winding, reaching the maximum value v_{zm}=7.97 m/s, by the end of the operating cycle is significantly reduced, amounting to v_{zf}=6.69 m/s. As a result, the efficiency of the converter, reaching the maximum value η_m=5.29 %, by the end of the operating cycle is reduced to η_f=3.65 %.

In order to evaluate the effectiveness of LPECIT when operating as an electromechanical accelerator, we use the values of the relative reduction of speed $\Delta v = 100\left(v_{zm} - v_{zf}\right)v_f^{-1},\%$ and efficiency $\Delta\eta = 100\left(\eta_m - \eta_f\right)\eta_m^{-1},\%$, as well as the relative criterion of efficiency $K_v^* = 100\dfrac{v_f^*}{j_{1m}^* f_{zm}^* \theta_1^*},\%$. As a basic variant we used CES with capacity C_0=0.5 mF in the absence of current limitation in the short-circuited armature winding.

With increasing capacity C_0 from 0.5 to 5 mF (W_0=500 J) and no limitation of the armature winding current (smooth lines in Fig. 5), the maximum speed v_{zm} decreases from 11.86 to 6.19 m/s, which leads to reduce the maximum efficiency η_m from 14.24 to 4.02 %, increase the temperature rise of the inductor winding θ_1 from 1.84 to 2.87 °C and reduce the same value for the armature winding θ_2 from 2.02 to 0.78 °C. The value of the relative decrease in the speed of the armature winding Δv increases from 5.9 to 21.97 %. The value of the relative decrease in efficiency $\Delta\eta$ is manifested only after increasing the capacity C_0 over 1 mF. It increases to $\Delta\eta$=57 % at C_0=5 mF. The relative criterion of the efficiency of the converter K_v^* is almost doubled primarily by reducing the amplitude of the current density in the winding of the inductor j_{1m} from 870.1 to 551.5 A/mm^2 and the amplitude of the EDF f_{zm} from 21.16 to 4.62 kN.

In the presence of current limitation in the armature winding due to the connection of the diode *VD* (line with circles in Fig. 5), the efficiency criterion K_v* increases, and to a greater extent with increasing capacity of the energy storage. At C_0=5 mF and in the absence of a diode K_v*=2.01, and in the presence of a diode K_v*=2.56. The value of the relative decrease in efficiency $\Delta\eta$ decreases significantly. It occurs only after increasing the capacity above C_0=2.5 mF and increases to $\Delta\eta$=28.86 % at C_0=5 mF. The maximum efficiency η_m increases only in the range of C_0 from 0.5 to 2.0 mF and equals to η_m=16.16 % at C_0=0.5 mF. The temperature rise of the armature winding θ_2 decreases, varying in the specified range from 1.48 to 0.61 °C.

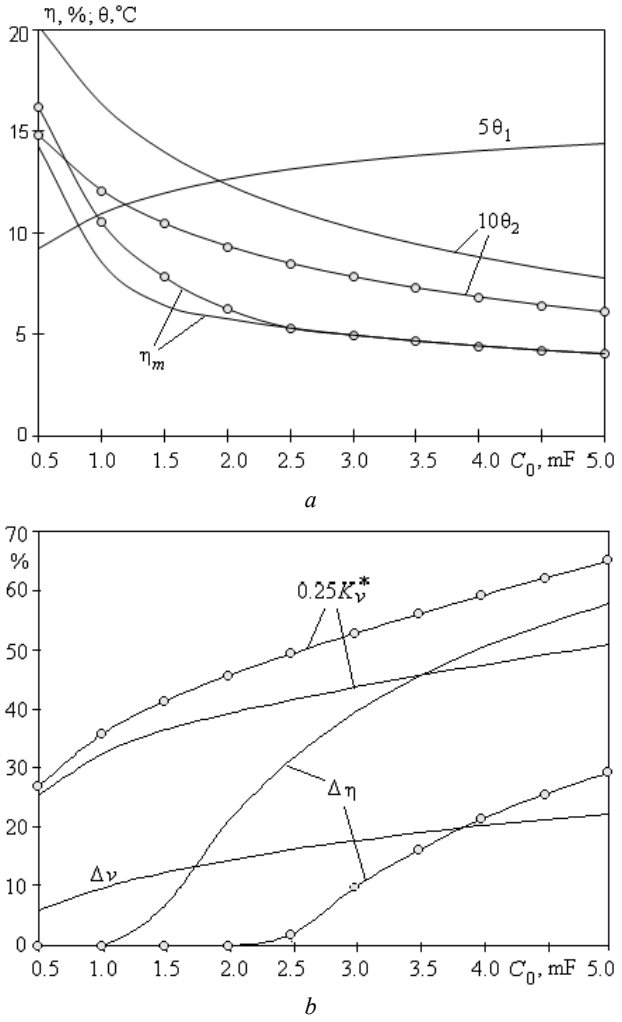

Fig. 5. Dependence of LPECIT performance at operation as an electromechanical accelerator on the capacity of CES at W_0=500 J

Thus, limiting the duration of the induced current in the armature winding before changing its polarity by connecting a rectifier diode to it increases the power performance of LPECIT as a shock-power device and increases the speed indicators of the converter operating as an electromechanical accelerator.

Conclusions.

1. To eliminate the attractive EDF between the windings of LPECIT, it is proposed to limit the duration of the induced current in the armature winding before changing its polarity by connecting a rectifier diode to it.

2. When LPECIT operates as a shock-power device, due to the attractive EDF the value of the moment of these forces, reaching the maximum value, decreases by the end of the operating cycle. When the duration of the current in the armature winding is limited, the value of the efficiency criterion, which takes into account the EDF impulse, recoil force, current and heating temperature of the inductor winding, increases (by 38.6 % at C_0=0.5 mF).

3. When LPECIT operates as an electromechanical accelerator without current limitation in the short-circuited armature winding, there is a decrease in speed and efficiency, which takes into account the kinetic energy and voltage of the CES at the end of the operating cycle. When the induced current in the armature winding is limited due to the connection of the rectifier diode, the efficiency criterion increases, and the temperature rise of the armature winding decreases. The maximum efficiency increases only in the range from 0.5 to 2 mF, amounting to 16.16 % at C_0=0.5 mF. The relative decrease in efficiency from the maximum to the final value decreases and occurs only after increasing the capacity C_0 over 2.5 mF.

Conflict of interest. The authors of the paper declare no conflict of interest.

REFERENCES

1. Balikci A., Zabar Z., Birenbaum L., Czarkowski D. Improved performance of linear induction launchers. *IEEE Transactions on Magnetics*, 2005, vol. 41, no. 1, pp. 171-175. doi: https://doi.org/10.1109/TMAG.2004.839283.

2. Go B., Le D., Song M., Park M., Yu I. Design and Electromagnetic Analysis of an Induction-Type Coilgun System With a Pulse Power Module. *IEEE Transactions on Plasma Science*, 2019, vol. 47, no. 1, pp. 971-976. doi: https://doi.org/10.1109/TPS.2018.2874955.

3. Vilchis-Rodriguez D.S., Shuttleworth R., Barnes M. Modelling Thomson Coils With Axis-Symmetric Problems: Practical Accuracy Considerations. *IEEE Transactions on Energy Conversion*, 2017, vol. 32, no. 2, pp. 629-639. doi: https://doi.org/10.1109/TEC.2017.2651979.

4. Bolyukh V.F., Katkov I.I. Cryogenic Cooling System "KrioBlast" Increased Efficiency and Lowered the Operation Time of Protective Electrical Induction-Induced Devices. *Proceedings of the ASME 2013 International Mechanical Engineering Congress and Exposition. Volume 8B: Heat Transfer and Thermal Engineering*. San Diego, California, USA. November 15-21, 2013. V08BT09A003. ASME. doi: https://doi.org/10.1115/imece2013-62383.

5. Zhou Y., Huang Y., Wen W., Lu J., Cheng T., Gao S. Research on a novel drive unit of fast mechanical switch with modular double capacitors. *The Journal of Engineering*, 2019, vol. 2019, no. 17, pp. 4345-4348. doi: https://doi.org/10.1049/joe.2018.8148.

6. Liu X., Yu X., Ban R., Li Z. Analysis of the Capacitor-Aided Meat Grinder Circuits for an Inductive Pulsed Power Supply. *IEEE Transactions on Plasma Science*, 2017, vol. 45, no. 7, pp. 1339-1346. doi: https://doi.org/10.1109/TPS.2017.2705179.

7. Kondratenko I.P., Zhyltsov A.V., Pashchyn N.A., Vasyuk V.V. Selecting induction type electromechanical converter for electrodynamic processing of welds. *Technical Electrodynamics*, 2017, no. 5, pp. 83-88. (Ukr). doi: https://doi.org/10.15407/techned2017.05.083.

8. Soda R., Tanaka K., Takagi K., Ozaki K. Simulation-aided development of magnetic-aligned compaction process with pulsed magnetic field. *Powder Technology*, 2018, vol. 329, pp. 364-370. doi: https://doi.org/10.1016/j.powtec.2018.01.035.

9. Gorodzha K.A., Podoltsev A.D., Troshchynckyi B.O. Electromagnetic processes in pulsed electrodynamic emitter to excite elastic vibrations in concrete structures. *Technical Electrodynamics*, 2019, no. 3, pp. 23-28. (Ukr). doi: https://doi.org/10.15407/techned2019.03.023.

10. Bolyukh V.F., Oleksenko S.V. The influence of the parameters of a ferromagnetic shield on the efficiency of a linear induction–dynamic converter. *Russian Electrical Engineering*, 2015, vol. 86, no. 7, pp. 425-431. doi: https://doi.org/10.3103/S1068371215070044.

11. Puumala V., Kettunen L. Electromagnetic design of ultrafast electromechanical switches. *IEEE Transactions on Power Delivery*, 2015, vol. 30, no. 3, pp. 1104-1109. doi: https://doi.org/10.1109/tpwrd.2014.2362996.

12. Bolyukh V.F., Schukin I.S., Lasocki J. Influence of the initial winding displacement on the indicators of the electromechanical induction accelerator of cylindrical configuration. *Electrical Engineering & Electromechanics*, 2021, no. 5, pp. 3-10. doi: https://doi.org/10.20998/2074-272X.2021.5.01.

13. Niu X., Li W., Feng J. Nonparametric Modeling and Parameter Optimization of Multistage Synchronous Induction Coilgun. *IEEE Transactions on Plasma Science*, 2019, vol. 47, no. 7, pp. 3246-3255. doi: https://doi.org/10.1109/tps.2019.2918157.

14. Kondratiuk M., Ambroziak L. Concept of the magnetic launcher for medium class unmanned aerial vehicles designed on the basis of numerical calculations, *Journal of Theoretical and Applied Mechanics*, 2016, vol. 54, no. 1, pp. 163-177. doi: https://doi.org/10.15632/jtam-pl.54.1.163.

15. Angquist L., Baudoin A., Norrga S., Nee S., Modeer T. Low-cost ultra-fast DC circuit-breaker: Power electronics integrated with mechanical switchgear. *2018 IEEE International Conference on Industrial Technology (ICIT)*, 2018, pp. 1708-1713. doi: https://doi.org/10.1109/icit.2018.8352439.

16. Bolyukh V.F., Dan'ko V.G., Oleksenko S.V. The Effect of an External Shield on the Efficiency of an Induction-Type Linear-Pulse Electromechanical Converter. *Russian Electrical Engineering*, 2018, vol. 89, no. 4, pp. 275-281. doi: https://doi.org/10.3103/S106837121804003X.

17. Bolyukh V.F., Katkov I.I. Influence of the Form of Pulse of Excitation on the Speed and Power Parameters of the Linear Pulse Electromechanical Converter of the Induction Type. *Volume 2B: Advanced Manufacturing*, Nov. 2019, 8 p. doi: https://doi.org/10.1115/imece2019-10388.

18. Bolyukh V.F., Shchukin I.S. Influence of an excitation source on the power indicators of a linear pulse electromechanical converter of induction type. *Technical Electrodynamics*, 2021, no. 3, pp. 28-36. doi: https://doi.org/10.15407/techned2021.03.028.

19. Ljutenko L.A., Mikhailov V.M. Expansion of cylindrical tubular workpieces on high-voltage magnetic-pulse installation with controlled vacuum discharger. *Electrical Engineering & Electromechanics*, 2021, no. 3, pp. 42-46. doi: https://doi.org/10.20998/2074-272X.2021.3.07

20. Bolyukh V.F., Kashanskyi Y.V., Shchukin I.S. Comparative analysis of power and speed indicators linear pulse electromechanical converters electrodynamic and induction

types. *Technical Electrodynamics*, 2019, no. 6, pp. 35-42. (Rus). doi: https://doi.org/10.15407/techned2019.06.035.
21. Bolyukh V.F., Vinnichenko A.I. Concept of an Induction-Dynamic Catapult for a Ballistic Laser Gravimeter. *Measurement Techniques*, 2014, vol. 56, no. 10, pp. 1098-1104. doi: https://doi.org/10.1007/s11018-014-0337-z.
22. Bolyukh V.F., Omel'chenko A.V., Vinnichenko A.I. Effect of Self-Seismic Oscillations of the Foundation on the Readout of a Ballistic Gravimeter with an Induction-Dynamic Catapult. *Measurement Techniques*, 2015, vol. 58, no. 2, pp. 137-142. doi: https://doi.org/10.1007/s11018-015-0675-5.

V.F. Bolyukh[1], *Doctor of Technical Science, Professor,*
I.S. Shchukin[2], *PhD, Associate Professor,*
[1] National Technical University «Kharkiv Polytechnic Institute»,
2, Kyrpychova Str., Kharkiv, 61002, Ukraine,
e-mail: vfbolyukh@gmail.com (Corresponding Author)
[2] Firm Tetra, LTD,
18, Gudanova Str., Kharkiv, 61024, Ukraine,
e-mail: tech@tetra.kharkiv.com.ua

Received 26.10.2021
Accepted 27.11.2021
Published 03.12.2021

How to cite this article:
Bolyukh V.F., Shchukin I.S. Influence of limiting the duration of the armature winding current on the operating indicators of a linear pulse electromechanical induction type converter. *Electrical Engineering & Electromechanics*, 2021, no. 6, pp. 3-10. doi: https://doi.org/10.20998/2074-272X.2021.6.01.

UDC 621.331 https://doi.org/10.20998/2074-272X.2021.6.02

S. Goolak, Ie. Riabov, V. Tkachenko, S. Sapronova, I. Rubanik

Model of pulsating current traction motor taking into consideration magnetic losses in steel

*The **aim** of the work is to develop a mathematical model of the traction motor of the pulsating current of an electric locomotive taking into account the magnetic losses in the motor steel to determine the starting parameters depending on the voltage of the armature winding. **Methodology**. Mathematical modeling of electromagnetic processes in a traction motor of pulsating current is applied taking into account the nonlinear nature of the armature inductance, the inductance of the excitation winding and the nonlinear nature of the universal magnetic characteristic. The magnetic losses in the steel of the traction motor were taken into account by establishing the dependence of these losses on the frequency of reversal, the magnetic flux in the magnetic circuit of the motor and the geometric dimensions of the motor. **Results**. The mathematical model of calculation of starting parameters of the traction engine of the pulsating current of the traction drive of the electric locomotive of alternating current taking into account the equation of instantaneous value of losses in engine steel is developed. The dynamic characteristics of the traction motor with pulsating current are obtained. It allows to investigate starting parameters of the traction engine on the basis of the received mathematical model and to design elements of the traction drive of the electric locomotive according to the specification, to choose optimum design parameters. **Originality**. For the first time a comprehensive study of the pulsating current traction motor was carried out taking into account the nonlinear nature of the armature inductance, excitation winding inductance and nonlinear nature of the universal magnetic characteristic and taking into account the magnetic losses in the motor steel. **Practical significance.** The model of the traction motor of pulsating current taking into account losses in steel of the engine on the basis of the carried-out calculation is developed. Experimental studies have confirmed the adequacy of the model, which allows to apply the obtained model to develop a mathematical model of an AC electric locomotive to study the electrodynamic processes in it at different modes of operation of the electric locomotive.* References 20, tables 2, figures 9.
Keywords: **pulsating current traction motor, eddy currents, magnetic losses, magnetic circuit.**

Запропоновано підхід до імітаційного моделювання тягових електродвигунів пульсуючого струму, заснований на врахуванні нелінійного характеру магнітної характеристики, індуктивностей якоря та обмотки збудження. Розроблено модель магнітних втрат у магнітопроводі якоря електродвигуна та досліджено їх вплив на характер електромагнітних процесів у електродвигуні. Показано, що отримані при цьому рішення узгоджуються з отриманими раніше результатами, але відкриваються додаткові можливості при дослідженні роботи двигуна в складі тягового електроприводу електровозу однофазно-постійного струму. Бібл. 20, табл. 2, рис. 9.
Ключові слова: **тяговий двигун пульсуючого струму, вихрові струми, магнітні втрати, магнітне коло.**

Introduction. Development and modeling of control algorithms for traction electric drives of single-phase DC electric locomotives with pulsating current traction motors require a reasonable choice of the model of traction electric motors. Simulation of work performed by pulsating current traction electric motors and systems used to control these motors should give a possibility to take into account a number of uncertainties. These uncertainties are related to the nonlinear nature of motor magnetization curve, occurrence of eddy currents in the magnetic circuit, and magnetic losses in the motor magnetic circuit caused by these currents. In addition, traction electric motor can operate with both full and attenuated excitation.

In this regard, one important circumstance can be noted. Taking into account a large number of works devoted to development of a model of pulsating current traction electric motor demanded models are those that take into account nonlinearity of magnetization characteristics and occurrence of eddy currents and magnetic losses in the motor magnetic circuit. This can be confirmed by works on approximation of magnetization characteristic [1, 2] and simulation of pulsating current traction electric motors of pulsating current taking into consideration influence of eddy currents on the nature of the magnetization curve [3]. Simulation models obtained in the result of applying these methods give an opportunity to determine with high accuracy such traction motor parameters as motor shaft speed at any load, currents flowing in traction motor circuits, electromotive force (EMF) generated by the motor, but taking into account all power losses in traction motor. This indicates that the subject of researches on development of a model of a pulsating current traction motor taking into account the nonlinear nature of the magnetization curve and the magnetic system as well as power losses in the traction motor is topical.

When modeling a direct current traction motor (DCM) of series excitation the main problem is to reproduce the dependence of magnetic flux on currents of field winding and armature currents; and this implies presence of load characteristics. In the work by [1] the authors propose to use universal magnetization curve for DCM of series excitation, and on the basis of universal magnetic characteristic to calculate universal expressions for the intrusive parameters of direct current traction electric machines and those of pulsating current traction motors. Since the universal magnetic characteristic is built for machines working under load, in order to reduce the error of approximation the author proposed to approximate the universal magnetic characteristic by means of two functions: magnetomotive force of the field winding and magnetomotive force of the armature reaction. For a particular rating of attenuation of excitation, it is possible to convert this expression into a function of one variable, such as armature current.

With an obviously correct approach to modeling the dependence of the magnetic flux on field winding currents this approach is not very convenient for modeling. This is due to the need to change the model parameters for each excitation attenuation mode.

The solution of this problem is given in the work by [2] where it is proposed to calculate the weber-ampere characteristic at certain coefficients of field attenuation based on electromechanical and mechanical characteristics of DCM. Also this work proposes a model for determining the dependence of magnetic flux on field winding currents and the armature winding currents. The transfer function with unknown parameters in this model is considered as an adaptive model with coefficients adapted to the experimental data.

Since DCM used for traction purposes have certain peculiarities of design and magnetic system, the use of universal magnetic characteristics is not always correct. Motor magnetic circuits consist of electrical materials that have both high magnetic conductivity and high electrical conductivity. These materials are characterized by eddy currents that occur during change of magnetic flux. These processes significantly affect the change of magnetic flux in the motor steel and, accordingly, the nature of electromagnetic processes occurring in it. In works by [1, 2] the influence caused by eddy currents in the motor magnetic circuit on the change of magnetic flux is not taken into account. Solution of this problem can be found in the work by [3]. In this study the authors propose a mathematical model of the pulsating current traction motor taking into account influence of eddy currents on the nature of electrodynamic processes occurring in the electric motor.

Since DC motors of series excitation always operate in the loaded mode, electrodynamic processes in the electric motor should also be modeled taking into account the load. This can be confirmed by studies presented in works by [4-6]. The authors show relationship between the nature of load and mechanical characteristics of DCM.

In addition, the works by [7-9] represent the effect of load on motor magnetic characteristic, which, in turn determine electromagnetic characteristics of DCM. But the above works do not show the transition from mathematical models to their implementation in simulation models.

The study by [10] states that during electric locomotive operation movement parameters are constantly changing starting, traction mode, braking mode, braking mode, skidding, etc.). As the operating mode (rating) is changed the motor shaft speed also changes. Magnetic losses in the magnetic circuit of the traction motor depend on the motor shaft speed [11-13].

When calculating magnetic losses in magnetic circuit of pulsating current traction electric motor certain difficulties occur. These difficulties are associated with the choice of loss calculation method. Different loss calculation methods use different normalization coefficients or ratios at the same approach to loss determination in DCM. Moreover, in different methods, the value of similar coefficients may differ significantly from each other. This leads to discrepancies in the results of loss calculations in DCM when applying different methods [14-16].

The solution to this problem can be found in the study by [17] where the authors based on the analysis of existing methods have identified and proposed the most accurate approach to calculation and modeling of instant magnetic losses in steel of DC traction motor on the example of NB-418K6 motor.

Therefore, **the aim of the article** is to develop a mathematical model of a traction motor with pulsating current taking into account magnetic losses to study electrodynamic processes.

Simulation model of pulse current traction motor. Simulation of electrodynamics processes in a pulsating current traction motor was performed on the example of the NB-418K6 traction motor. Rating data of NB-418 K6 pulsating current traction motor is presented in Table 1.

Table 1

Rating data of NB-418 K6 pulsating current traction motor

Parameter	Designation	Units	Value
Nominal voltage	U_d	V	950
Nominal power in the continuous rating	P	kW	740
Nominal current in continuous rating	I_a	A	820
Nominal speed of the motor shaft in continuous rating	n	rpm	915
Nominal torque on the motor shaft	T	N·m	7727
Armature winding resistance at t = 115 °C	r_{aw}	Ω	0.01612
Resistance of additional poles and field winding at t = 115 °C	r_{ap+cw}	Ω	0.01612
Resistance of main poles at t = 115 °C	r_{mp}	Ω	0.01064
Field winding resistance at t = 115 °C	r_f	Ω	0.001
Number of pole pairs	p	–	3
Number of pairs of parallel branches in armature winding	a	–	3
Number of armature winding conductors	N	–	696
Inertia moment of the motor rotor	J	kg·m^2	73
Cross sectional area of the armature yoke	S_Y	m^2	0.0810
Cross sectional area of the armature teeth	S_z	m^2	0.0415

Electric scheme of the DC traction motor is presented in Fig. 1.

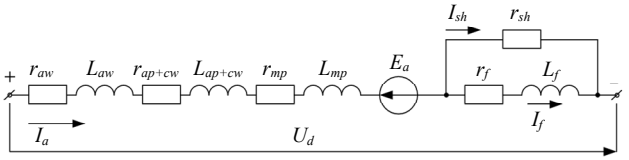

Fig. 1. Electric scheme of the pulsating current traction motor windings:

r_{aw}, r_{ap+cw}, r_{mp}, r_{sh}, r_f – active resistances of armature winding, additional poles and compensation winding, main poles, shunt, field winding; L_{aw}, L_{ap+cw}, L_{mp}, L_f - inductances of armature winding, additional poles and compensation winding, main poles, field winding; U_d – armature voltage; E_a – armature EMF; I_a, I_{sh}, I_f – currents of armature, shunt and field winding

According to Kirchhoff's laws equations of the motor electrics for the circuit shown in Fig. 1 are as follows:

$$U_d = E_a + r_a \cdot I_a + L_a \cdot \frac{dI_a}{dt} + r_{sh} \cdot I_{sh}; \quad (1)$$

$$r_{sh} \cdot I_{sh} = L_f \cdot \frac{dI_f}{dt} + r_f \cdot I_f; \quad (2)$$

$$I_a = I_{sh} + I_f, \quad (3)$$

where E_a is the armature electromotive force; r_a, L_a are the active resistance and inductance of armature circuit respectively; r_f, L_f are the active resistance and inductance of field winding respectively; r_{sh} is the resistance of shunt resistor; I_a is the armature current; I_f is the field winding current; r_{sh} is the resistance of shunt resistor; U_d is the armature voltage.

For convenience of modeling electrical scheme of the pulsating current traction motor windings is shown in the following form (Fig. 2).

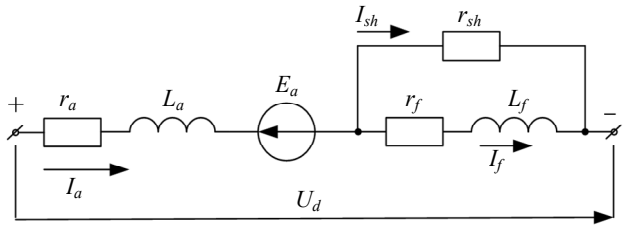

Fig. 2. Simplified electric scheme of the pulsating current traction motor windings: r_a - active resistance of armature; L_a - inductance of armature circuit

Armature resistance is defined as

$$r_a = r_{aw} + r_{ap+cw}, \tag{4}$$

where r_{aw} is the armature winding active resistance; r_{ap+cw} is the active resistance of additional poles and compensation winding.

Armature inductance is defined as

$$L_a = L_{aw} + L_{ap+cw}, \tag{5}$$

where L_{aw} is the inductance of armature winding; L_{ap+cw} is the inductance of additional poles and compensation winding.

Electromotive force E_a is calculated as

$$E_a = C_E \cdot \Phi \cdot \omega, \tag{6}$$

where C_E is the constructive constant coefficient for EMF; Φ is the total magnetic flux of the motor.

Constructive constant coefficient for EMF for shaft speed expressed in *rpm* is determined by the following expression

$$C_E = \frac{N \cdot p}{2 \cdot \pi \cdot a}, \tag{7}$$

where N is the number of armature winding conductors; p is the number of pole pairs; a is the number of pairs of parallel branches in armature winding.

Equation of motor mechanical equilibrium:

$$M - M_c = J \cdot \frac{d\omega}{dt}, \tag{8}$$

where M is the torque moment; M_c is the load moment on the motor shaft; J is the inertia moment of the motor rotor; ω is the angular motor shaft speed.

For modeling convenience expression (8) is represented as a derivative of the angular velocity over time:

$$\frac{d\omega}{dt} = \frac{1}{J} \cdot (M - M_c). \tag{9}$$

Torque moment is determined according to the following expression:

$$M = C_M \cdot \Phi \cdot I_a, \tag{10}$$

where C_M is the constructive constant coefficient for the moment.

Constructive constant coefficients for the EMF and for the moment are equal ($C_E = C_M$).

In this research, the authors propose to implement the model of pulsating current traction motor on the basis of real magnetic characteristics of the motor.

Magnetic characteristics of NB-418 K6 traction motor is presented in Fig. 3 [17].

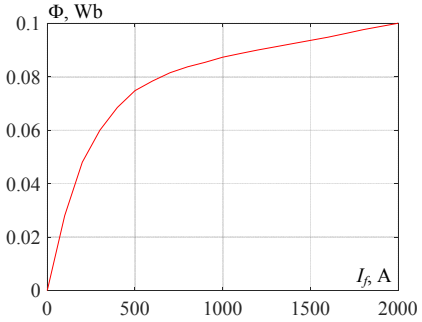

Fig. 3. Dependence of the magnetic flux Φ of the NB-418 K6 traction motor on the field current I_f

Consideration of magnetic losses in traction motor steel is performed according to the algorithm presented in equations (11) – (20).

Specific power losses in electrical steel on eddy currents and hysteresis, taking into account the accumulation of magnetic energy at a given magnetic permeability μ_r = 1, as a function of time, respectively [17] can be presented by the following equations:

$$\begin{aligned} p_{loss}(t) &= \left(H_c + K_{hyst} \cdot \left|B_p \cdot sin(\omega_r \cdot t)\right|\right) \cdot \\ &\cdot \left(B_p \cdot \omega_r \cdot cos(\omega_r \cdot t)\right) + \\ &+ K_{addy} \cdot B_p^2 \cdot \omega_r^2 \cdot cos^2(\omega_r \cdot t), \end{aligned} \tag{11}$$

where p_{loss} is the specific power losses, W/m^3; H_c is the coercive force; V_{is} is the induction amplitude of the charge; ω_r is the frequency of alternating magnetization; t is the time; K_{addy} is the coefficient taking into account specific losses on eddy currents; K_{hyst} is the coefficient taking into account the specific losses on hysteresis.

Frequency of alternating magnetization can be found from the expression

$$\omega_r = p \cdot \omega, \tag{12}$$

where p is the number of pole pairs; ω is the rotation frequency of electric motor shaft.

In order to implement the model of magnetic losses in electrical steel, it is necessary to find the amplitudes of inductions in the nodes made of electrical steel – yoke and anchor teeth [17].

Magnetic induction in the armature yoke can be calculated by means of the following expression

$$B_a = \frac{2 \cdot \Phi_\alpha}{S_a}, \tag{13}$$

where S_a is the cross sectional area of the armature yoke [17]; Φ_a is the armature magnetic flux.

Magnetic induction in the armature teeth can be calculated by means of the following expression

$$B_z = \frac{\Phi_a}{S_z}, \tag{14}$$

where S_z is the cross sectional area of the armature teeth [17].

The armature magnetic flux is equal to the total magnetic flux of the traction motor.

The total magnetic loss is the sum of magnetic losses in the armature and armature teeth, i.e.

$$p_{loss\Sigma}(t) = p_{lossY}(t) + p_{lossz}(t), \quad (15)$$

where $P_{lossY}(t)$, $P_{lossz}(t)$ are the magnetic losses in the armature core and armature teeth.

The given magnetic permeability of 2212 steel differs from 1 [17]. That is, for the transition from a generalized steel sheet with reduced magnetic permeability $\mu_r = 1$, defined by means of equation (11), to a 2212 steel sheet with permeability μ_{r1} equation (15) should be multiplied by μ_{r1}.

Coefficients H_c, K_{hyst} and K_{addy} in equation (11) were determined for specific power losses expressed in W/kg. For transition to losses expressed in watts, equation (11) should be multiplied by the mass of steel of the corresponding motor structural element. Mass of steel of the structural element is determined by the following expression

$$m_i = \rho \cdot V_i, \quad (16)$$

where V_i is the volume of the structural element; ρ = 7750 kg/m^3 is the specific weight of 2212 electrical steel.

Then the instantaneous values of losses in the yoke and anchor teeth, taking into account equation (11) can be expressed as follows:

$$P_{lossY}(t) = p_{lossY}(t) \cdot \rho \cdot V_Y^2 \cdot \mu_{r1}; \quad (17)$$

$$P_{lossz}(t) = p_{lossz}(t) \cdot \rho \cdot V_z^2 \cdot \mu_{r1}, \quad (18)$$

where V_Y, V_z are the volumes of armature yoke steel and steel of armature teeth respectively; μ_{r1} = 2400 is the relative magnetic permeability of 2212 steel at frequency of 50 Hz and inductance B = 1.82 T [17].

Magnetic losses in the motor steel of the model are taken into account as follows. Relationship between active power and engine shaft speed is defined by the following expression:

$$P_{loss} = \omega \cdot M_{closs}, \quad (19)$$

where M_{closs} is the static moment caused by magnetic losses in the motor steel.

Hence the static moment caused by the magnetic losses in the motor steel is s follows

$$M_{closs} = \frac{P_{loss}}{\omega}. \quad (20)$$

The work by [18] shows that both armature circuit inductance and inductance of field winding have a non-linear dependence on armature current and field current respectively. In this regard, the model of the electrical part of the traction motor in the MATLAB software environment was implemented in the Special Power System section of the Simulink library. This gave an opportunity to use real values of motor winding resistances, and the nonlinear dependences of the armature circuit inductance and field winding inductance on the corresponding currents was substituted with units of controlled current sources. Control signals for current sources simulating armature circuit inductance and field winding inductance were presented as the following dependences

$$I_a = f(\psi_a), \quad (21)$$

$$I_f = f(\psi_f), \quad (22)$$

where ψ_a is the flux linkage of armature; ψ_f is the flux linkage of field winding.

Flux linkages ψ_a and ψ_f were obtained based on expressions (1) i (2) respectively.

With this end in view, based on the results for dependences of the armature circuit inductance and field winding inductance on the corresponding currents presented in the work [18], dependence of the armature current on the armature circuit flux linkage (Fig. 4) and dependence of field winding current from field current (Fig. 5) were calculated and constructed.

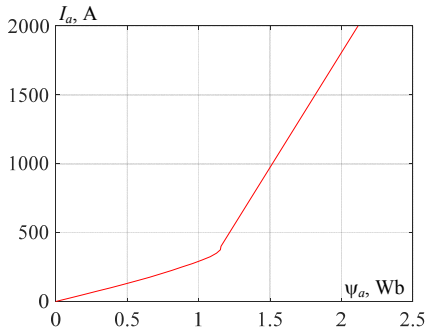

Fig. 4. Dependence of armature circuit current I_a on flux linkage ψ_a

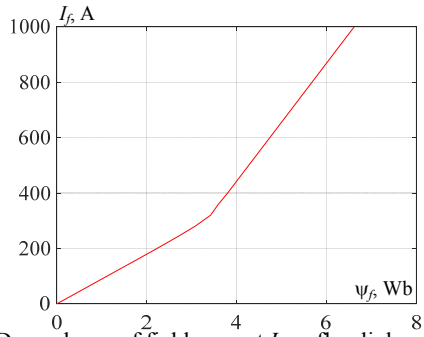

Fig. 5. Dependence of field current I_f on flux linkage of field winding ψ_f

All other structural elements of the traction motor model were presented in form of structural diagrams.

Simulation model performed on the example of the NB-418 K6 traction electric motor used on electric locomotives of alternating current VL-80T, VL-80K (Fig. 6).

Implementation of the traction motor electrical part in the MATLab software environment is shown in Fig. 6 in form of the «Engine currents determination unit». Calculation of magnetic flux performed by approximation of the magnetic characteristic (Fig. 3) based on the arctangent function. In Fig. 6 implementation of Magnetic Characteristic is presented in form of the «Magnetic flux detection unit».

Electric motor mechanical part in Fig. 6 is represented in form of the «Unit for calculating the mechanical parameters of the engine» that implements equations (9), (10). Calculation of instantaneous values of magnetic losses in electric motor steel that implements equations (11) – (20) is presented in the simulation model in form of the «Unit for calculating the static moment caused by magnetic losses» (Fig. 6).

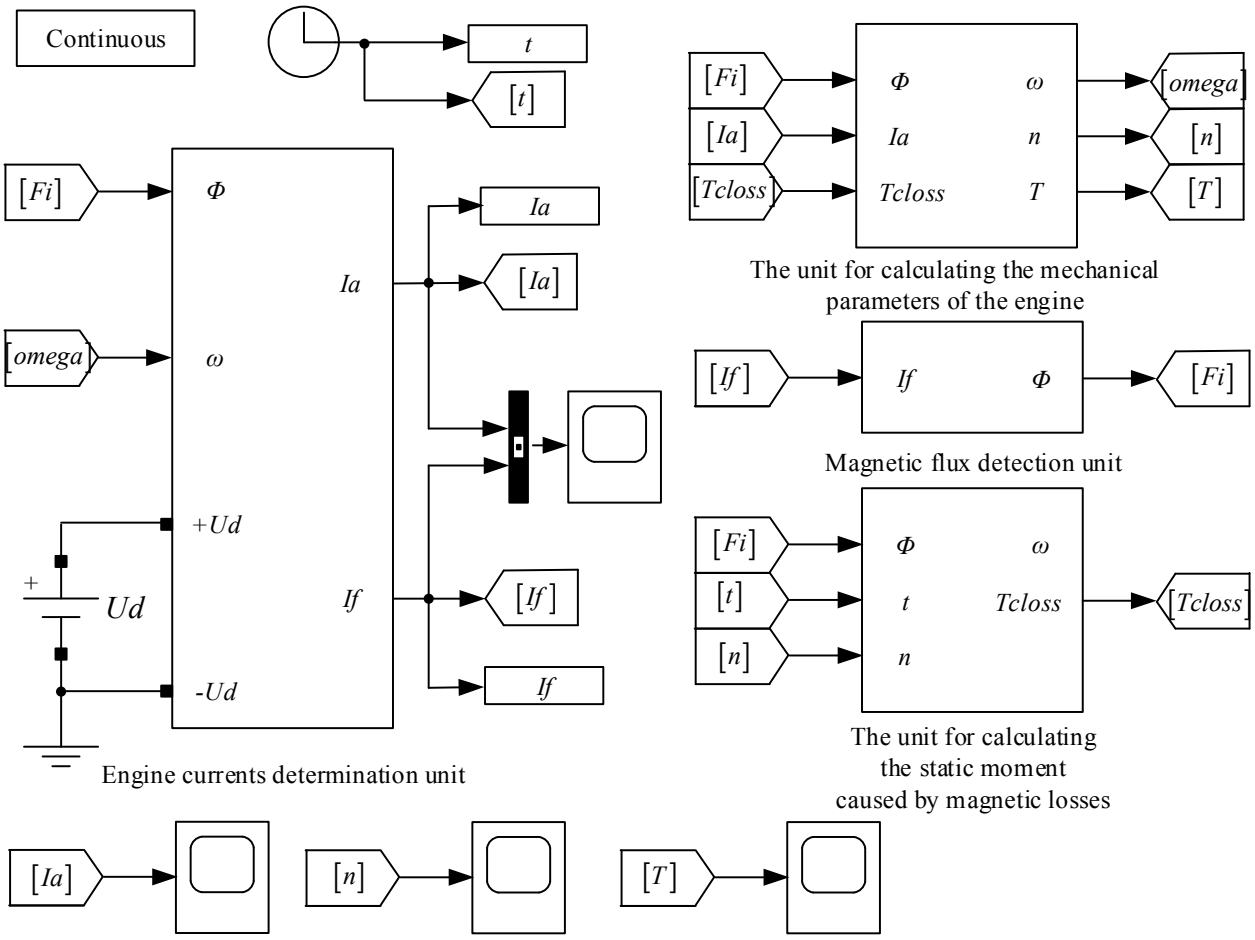

Fig. 6. Simulation model of a traction electric motor implemented in the MATLAB software environment

Simulation results. In order to determine starting characteristics of pulsating current traction electric motor a constant voltage U_d of 950 V corresponding to the nominal voltage value for NB-418 K6 traction motor. In the «Unit for calculating the mechanical parameters of the engine» a static moment T_c of 7727 N·m was created; and in the «Engine currents determination unit» shunt resistance r_{sh} was accepted as 0.24 Ω and these values also correspond to the nominal mode of electric motor operation.

On the simulation model (Fig. 6) obtained are time diagrams of armature current (Fig. 7), torque moment on the electric motor shaft (Fig. 8) and motor shaft speed (Fig. 9).

For the steady-state rating a value of excitation flux Φ was equal to 0.0819 Wb.

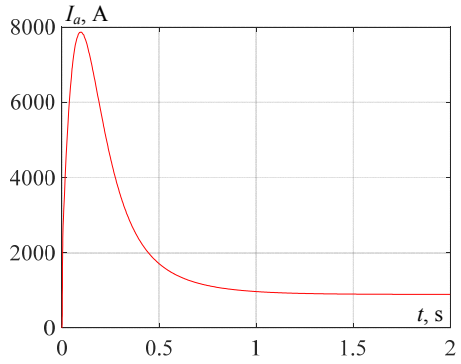

Fig. 7. Time diagrams of armature current I_a

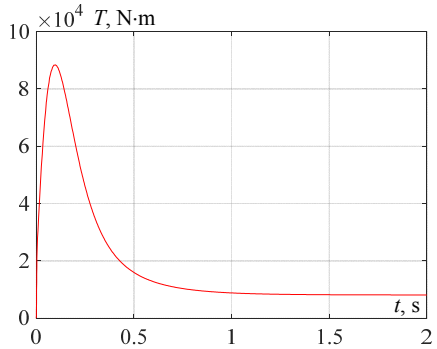

Fig. 8. Time diagram of torque moment T on the motor shaft

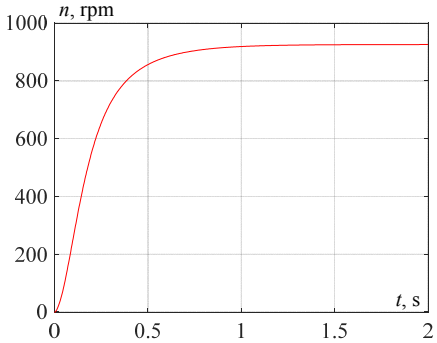

Fig. 9. Time diagram of motor shaft speed n

Values of armature circuit current, the torque moment on the motor shaft, motor shaft speed and the

magnetic flux for the steady-state rating obtained during the simulation were used to calculate errors in determining these values.

Error in determination of armature circuit current

$$\delta_{I_a} = \left|\frac{I_{anom} - I_{amod}}{I_{anom}}\right| \cdot 100\% = \\ = \left|\frac{820 - 881}{820}\right| \cdot 100\% = 6,93\%, \quad (23)$$

where I_{anom} = 820 A is the armature nominal current (see Table 1); I_{amod} = 881 *A* is the armature current obtained in the result of modeling for the steady-state rating.

Flux determination error

$$\delta_{\Phi} = \left|\frac{\Phi_{nom} - \Phi_{mod}}{\Phi_{nom}}\right| \cdot 100\% = \\ = \left|\frac{0,08 - 0,0819}{0,08}\right| \cdot 100\% = 2,375\%, \quad (24)$$

where Φ_{anom} = 0.08 Wb is the nominal magnetic flux (see Table 1); Φ_{amod} = 0.0819 Wb is the magnetic flux obtained in the result of modeling for the steady-state rating.

Error in determination of torque moment on the motor shaft:

$$\delta_T = \left|\frac{T_{nom} - T_{mod}}{T_{nom}}\right| \cdot 100\% = \\ = \left|\frac{7727 - 7990}{7727}\right| \cdot 100\% = 3,4\%, \quad (25)$$

where T_{anom} = 7727 N·m is the nominal torque moment on the motor shaft (see Table 1); T_{amod} = 7990 N·m is the torque moment on the motor shaft obtained in the result of modeling for the steady-state rating.

Error in determination of torque moment on the motor shaft:

$$\delta_n = \left|\frac{n_{nom} - n_{mod}}{n_{nom}}\right| \cdot 100\% = \\ = \left|\frac{915 - 951,6}{915}\right| \cdot 100\% = 4\%, \quad (26)$$

where n_{anom} = 915 rpm is the rated motor shaft speed (Table 1); n_{amod} = 951.6 rpm is the motor shaft speed obtained in the result of modeling for the steady-state rating.

Results of modeling and calculation of errors in determination of controlled motor parameters are listed in Table 2.

Table 2

Results of calculation of errors in determination of controlled parameters during modeling

Rating	Controlled parameter											
	Armature current I_a, A			Static moment T, N·m			Motor shaft speed n, rpm			Flux Φ, Wb		
	I_a	I_{amod}	δ_{Ia}, %	T	T_{mod}	δ_T, %	n	n_{mod}	δ_n,%	Φ	Φ_{mod}	δ_Φ,%
U_d = 950 V Excitation 96% T_c = 7727 N·m	820	881	6.93	7727	7990	3.4	915	951.6	4.0	0,08	0,0819	2,375
U_d = 1080 V Excitation 96 % T_c = 7727 N·m	840	885.3	5.39	7727	8030	3.9	1050	1088	3.5	0,082	0,0839	2,317
U_d = 950 V Excitation 43 % T_c = 7727 N·m	1155	1212	4.93	7727	8174	5.78	1055	1091	3.41	0,11	0,1127	2,45
U_d = 950 V Excitation 96 % T_c = 5597 N·m	665	691.8	4.03	5597	5859	4.68	965	996.2	3.23	0,065	0,0664	2,154

The results shown in Table 2 indicate a high reliability of measuring controlled parameters. Thus, the armature current measurement error for all measurement modes did not exceed 7 %; torque measurement error was up to 6 %; the error of measuring the motor shaft speed was not more than 4 % and the error of measuring the magnetic flux did not exceed 3 %. This indicates a high reliability of the modeling results and increases the accuracy of calculations of energy-intensive modes of rolling stock [19, 20].

Conclusions.

The use of the unit for determining the magnetic losses in the motor armature of the motor made it possible to clarify values of the controlled parameters during modeling. Comparison of the controlled parameters in the steady-state rating with the motor passport data showed a high degree of reliability of the simulation results. Thus, the armature current measurement error for all measurement modes did not exceed 7 %; torque measurement error was up to 6 %; the error of measuring the motor shaft speed was not more than 4 %, the error of measuring the magnetic flux did not exceed 3 %. Further refinement of the mathematical model is related to taking into account all types of losses in the motor components when it is powered from a pulsating voltage source.

The proposed approach to modeling of a pulsating current traction electric motor will give an opportunity to apply this model for development of a mathematical model of the traction electric drive of an electric locomotive aimed at studying electrodynamic processes occurring in the electric drive.

The presence of the unit for determining magnetic losses in the motor steel will give an opportunity to reliably assess spectral composition of the traction current and voltage in the secondary winding of the traction transformer at various modes of electric locomotive operation. This, in turn, will give an opportunity to evaluate operation of reactive power compensators taking into account various modes of electric locomotive operation.

Funding. This work was supported by the Ministry of Education and Science of Ukraine in the project DR No. 0120U101912: Increasing the energy efficiency of rolling stock based on resource-saving technologies and smart energy systems.

Conflict of interest. The authors declare that they have no conflicts of interest.

REFERENCES

1. Nayak B., Sahu S., Choudhury T.R. Parameter estimation of DC motor using adaptive transfer function based on Nelder-Mead optimization. *Indonesian Journal of Electrical Engineering and Computer Science*, 2018, vol. 9, no 3, pp. 696-702. doi: https://doi.org/10.11591/ijeecs.v9.i3.pp696-702.

2. Drubetskyi A.Y. Approximation of universal magnetic characteristic for modelling electric traction machines. *Science and Transport Progress. Bulletin of Dnipropetrovsk National University of Railway Transport*, 2017, no. 1(67), pp. 106-116. doi: https://doi.org/10.15802/stp2017/94031.

3. Kulinich Yu.M., Shukharev S.A., Drogolov D.Yu. Simulation of the pulsating current traction motor. *VNIIZHT Scientific Journal*, 2019, vol. 78, no. 5, pp. 313-319. (Rus). doi: https://doi.org/10.21780/2223-9731-2019-78-5-319.

4. Shepovalova O.V., Belenov A.T. Investigation of DC Motors Mechanical Characteristics with Powered by Comparable Capacity PV Array. *Energy Procedia*, 2017, vol. 119, pp. 990-994. doi: https://doi.org/10.1016/j.egypro.2017.07.132.

5. Evseev, V. Y., Savos'kin, A. N. A Mathematical Model of a Collector Traction Motor with Separate Consideration of Eddy Currents of the Main and Additional Poles. *Russian Electrical Engineering*, 2020, vol. 91, no 9, pp. 557-563. doi: https://doi.org/10.3103/s1068371220090047.

6. Litovchenko V.V., Nazarov D.V. Sharov V.A. Simulation Model of a Direct-Current Electric Locomotive with Commutator Traction Motors. *Russian Electrical Engineering*, 2020, vol. 91, no. 1, pp. 69-76. doi: https://doi.org/10.3103/s1068371220010071.

7. Spiryagin M., Wolfs P., Cole C., Spiryagin V., Sun Y.Q., McSweeney T. *Design and Simulation of Heavy Haul Locomotives and Train*. New York, Taylor & Francis Group, 2016. 477 p. doi: https://doi.org/10.1201/9781315369792.

8. Castaneda C.E., Loukianov A.G., Sanchez E.N., Castillo-Toledo B. Discrete-Time Neural Sliding-Mode Block Control for a DC Motor With Controlled Flux. *IEEE Transactions on Industrial Electronics*, 2012, vol. 59, no. 2, pp. 1194-1207. doi: https://doi.org/10.1109/TIE.2011.2161246.

9. Kharchenko V., Kostenko I., Liubarskyi B., Shaida V., Kuravskyi M., Petrenko O. Simulating the traction electric drive operation of a trolleybus equipped with mixed excitation motors and a DC-DC converter. *Eastern-European Journal of Enterprise Technologies*, 2020, vol. 3, no. 9 (105), pp. 46-54. doi: https://doi.org/10.15587/1729-4061.2020.205288.

10. Goolak S., Tkachenko V., Bureika G., Vaičiūnas G. Method of spectral analysis of traction current of AC electric locomotives. *Transport*, 2020, vol. 35, no 6, pp. 658-668. doi: https://doi.org/10.3846/transport.2020.14242.

11. Liu R., Li L. Calculation Method of Magnetic Material Losses Under DC Bias Using Statistical Loss Theory and Energetic Hysteresis Model. *IEEE Transactions on Magnetics*, 2019, vol. 55, no 10, pp. 1-4. doi: https://doi.org/10.1109/TMAG.2019.2921357.

12. Zhang H., Mueller M. Electromagnetic properties of curved HTS trapped field stacks under high-frequency cross fields for high-speed rotating machines. *Superconductor Science and Technology*, 2021, vol. 34, no 4, pp. 045018. doi: https://doi.org/10.1088/1361-6668/abe4b6.

13. Kwon H., Park H. Numerical Investigation of Optimal Air Flowrate for Cooling 600 W Brushless Direct-Current Motor. *Journal of Thermal Science and Engineering Applications*, 2021, vol. 13, no 4, pp. 041008. doi: https://doi.org/10.1115/1.4048755.

14. Rens J., Vandenbossche L., Dorez O. Iron Loss Modelling of Electrical Traction Motors for Improved Prediction of Higher Harmonic Losses. *World Electric Vehicle Journal*, 2020, vol. 11, no 1, p. 24. doi: https://doi.org/10.3390/wevj11010024.

15. Zhao J., Quan X., Jing M., Lin M., Li N. Design, Analysis and Model Predictive Control of an Axial Field Switched-Flux Permanent Magnet Machine for Electric Vehicle/Hybrid Electric Vehicle Applications. *Energies*, 2018, vol. 11, no. 7, pp. 1859. doi: https://doi.org/10.3390/en11071859.

16. Cheng G., Guo X., Wen Y., Wang Q., Li G., Zhou R. Electromagnetic Modeling and Analysis of 3-DOF Permanent Magnet Spherical Motor Using Magnetic Equivalent Circuit Method. *2018 21st International Conference on Electrical Machines and Systems (ICEMS)*, 2018, pp. 2643-2648. doi: https://doi.org/10.23919/ICEMS.2018.8548998.

17. Goolak S., Sapronova S., Tkachenko V., Riabov I., Batrak Y. Improvement of the model of power losses in the pulsed current traction motor in an electric locomotive. *Eastern-European Journal of Enterprise Technologies*, 2020, vol. 6, no. 5 (108), pp. 38-46. doi: https://doi.org/10.15587/1729-4061.2020.218542.

18. Goolak S., Tkachenko V., Sapronova S., Spivak O., Riabov I., Ostroverkh O. Determination of inductances for pulsating current traction motor. *Technology audit and production reserves*, 2021, vol. 2, no. 1(58), pp. 40-43. doi: https://doi.org/10.15587/2706-5448.2021.229217.

19. Petrenko A.N., Liubarskiy B.G., Pliugin V.E. Determination of railway rolling stock optimal movement modes. *Electrical Engineering & Electromechanics*, 2017, no. 6, pp. 27-31. doi: https://doi.org/10.20998/2074-272X.2017.6.04.

20. Buriakovskyi S.G., Maslii A.S., Panchenko V.V., Pomazan D.P., Denis I.V. The research of the operation modes of the diesel locomotive CHME3 on the imitation model. *Electrical Engineering & Electromechanics*, 2018, no. 2, pp. 59-62. doi: https://doi.org/10.20998/2074-272X.2018.2.10.

Received 11.10.2021
Accepted 13.11.2021
Published 03.12.2021

S. Goolak[1]*, PhD,*
Ie. Riabov[2]*, PhD, Associate Professor,*
V. Tkachenko[1]*, Doctor of Technical Science, Professor,*
S. Sapronova[1]*, Doctor of Technical Science, Professor,*
I. Rubanik[3]*, Chief Designer,*
[1] State University of Infrastructure and Technologies,
9, Kyrylivska Str., Kyiv, 04071, Ukraine,
e-mail: sgoolak@gmail.com (Corresponding Author).
[2] National Technical University «Kharkiv Polytechnic Institute»,
2, Kyrpychova Str., Kharkiv, 61002, Ukraine.
[3] JSC «Riga Electric Machine Building Works»,
53, Ganibu Dambis Str., Riga, LV-1005, Latvia.

How to cite this article:
Goolak S., Riabov Ie., Tkachenko V., Sapronova S., Rubanik I. Model of pulsating current traction motor taking into consideration magnetic losses in steel. *Electrical Engineering & Electromechanics*, 2021, no. 6, pp. 11-17. doi: https://doi.org/10.20998/2074-272X.2021.6.02.

UDC 621.313 https://doi.org/10.20998/2074-272X.2021.6.03

K. Akkouchi, L. Rahmani, R. Lebied

New application of artificial neural network-based direct power control for permanent magnet synchronous generator

Purpose. *This article proposes a new strategy for Direct Power Control (DPC) based on the use of Artificial Neural Networks (ANN-DPC). The proposed ANN-DPC scheme is based on the replacement of PI and hysteresis regulators by neural regulators. Simulation results for a 1 kW system are provided to demonstrate the efficiency and robustness of the proposed control strategy during variations in active and reactive power and in DC bus voltage.* ***Methodology***. *Our strategy is based on direct control of instant active and reactive powers. The voltage regulator and hysteresis are replaced by more efficient and robust artificial neuron networks. The proposed control technique strategy is validated using MATLAB / Simulink software to analysis the working performances.* ***Results***. *The results obtained clearly show that neuronal regulators have good dynamic performances compared to conventional regulators (minimum response time, without overshoots).* ***Originality***. *Regulation of continuous bus voltage and sinusoidal currents on the network side by using artificial neuron networks.* ***Practical value***. *The work concerns the comparative study and the application of DPC based on ANN techniques to achieve a good performance control system of the permanent magnet synchronous generator. This article presents a comparative study between the conventional DPC control and the ANN-DPC control. The first strategy based on the use of a PI controller for the control of the continuous bus voltage and hysteresis regulators for the instantaneous powers control. In the second technique, the PI and hysteresis regulators are replaced by more efficient neuronal controllers more robust for the system parameters variation. The study is validated by the simulation results based on MATLAB / Simulink software.* References 26, tables 5, figures 19.

Key words: **artificial neural network, direct power control, permanent magnet synchronous generator, direct power control based on the use of artificial neural networks.**

Мета. *У статті пропонується нова стратегія прямого керування потужністю (DPC), яка базується на використанні штучних нейронних мереж (ANN-DPC). Запропонована схема ANN-DPC заснована на заміні пропорційно-інтегрального (ПІ) та гістерезисного регуляторів на нейронні регулятори. Наведено результати моделювання для системи потужністю 1 кВт для демонстрації ефективності та надійності запропонованої стратегії керування при зміні активної та реактивної потужності, а також напруги на шині постійного струму.* ***Методологія***. *Запропонована стратегія базується на прямому керуванні миттєвими активними та реактивними потужностями. Регулятор напруги та гістерезисний регулятор замінені більш ефективними та надійними штучними нейронними мережами. Запропонована методика керування перевірена з використанням програмного забезпечення MATLAB / Simulink для аналізу робочих характеристик.* ***Результати***. *Отримані результати показують, що нейронні регулятори мають хороші динамічні характеристики порівняно зі звичайними регуляторами (мінімальний час відгуку, без викидів).* ***Оригінальність***. *Регулювання постійної напруги на шині та синусоїдальних струмів на стороні мережі за допомогою штучних нейронних мереж.* ***Практична цінність***. *Робота стосується порівняльного дослідження та застосування прямого керування потужністю (DPC) на основі методів штучної нейронної мережі (ANN) для досягнення хороших показників системи керування синхронного генератора з постійними магнітами. У цій статті представлено порівняльне дослідження між звичайним керуванням DPC та керуванням ANN-DPC. Перша стратегія заснована на використанні ПІ-регулятора для керування постійною напругою на шині та гістерезисних регуляторів для керування миттєвою потужністю. У другому методі ПІ- та гістерезисні регулятори замінюються більш ефективними нейронними контролерами, більш стійкими до зміни параметрів системи. Дослідження підтверджено результатами моделювання на основі програмного забезпечення MATLAB / Simulink.* Бібл. 26, табл. 5, рис. 19.

Ключові слова: **штучна нейронна мережа, пряме керування потужністю, синхронний генератор з постійними магнітами, пряме керування потужністю на основі штучних нейронних мереж.**

Introduction. Electric machines are often known by their windings and their own and complex geometry. In electrical engineering laboratories, the study of synchronous machines with permanent magnet generators is currently a broad research topic. A permanent magnet synchronous generator (PMSG) which obtains energy from mechanical energy for generate an electric current [1]. Synchronous machines with permanent magnets have experienced a great boom in recent years. This is thanks to the improvement of the qualities of permanent magnets more precisely with the help of rare earths, the development of power electronics and the evolution of non-linear control techniques. The advantages of this type of electric machine are numerous, among which we can cite: robustness, low inertia, high mass torque, high efficiency, higher maximum speed and low maintenance cost. In addition, permanent magnets have undeniable advantages: on the one hand, the inducing flux is created without loss of excitation and on the other hand, the use of these materials will make it possible to deviate significantly from the usual sizing constraints. machines and therefore increase the specific power significantly [2]. Several control strategies applied to PMSG, for example vector control [3, 4], direct torque control [5, 6], direct power control (DPC) and sliding mode control [7, 8]. In [9] compared a conventional multi-network, in which the supervision network is replaced by an expert system and a conventional network. They obtained results similar to those of authors in [10]. Their results are more effective when the characteristics are more relevant. In [11] have taken over the multi-networks used in [9] to assess the detection of epileptic transients. The results obtained were compared with those of 4 experts. Even if these results are insufficient to be used in medical practice, they have made it possible to demonstrate that it is possible to detect epileptic transients and that the supervision network eliminates certain bad decisions. In [10] compared several multi-network architectures with a conventional neural network. The neural networks used are error

backpropagation with an input range of 0 to 1. Each neural network is trained 3 times to verify the repetition of the results obtained and to avoid overtraining. The total sum of the squared errors of the test set is used to evaluate the training. The main qualities of neural networks are their capacity for adaptability and self-organization and the possibility of solving non-linear problems with a good approximation [12, 13]. The reason for this trend is the many advantages, which the architectures of artificial neural network (ANN) have over traditional algorithmic methods [14].

Related works. We cite a few articles in this area of research. The article [4] presents a comparative study between voltage oriented control and DPC. It has been shown that best power quality features are given by vector control techniques. On the other hand, direct control offers the better dynamic response. The work [1] assessed the performance of DPC, HYN-DPC (Neural hysteresis DPC) and ANN-DPC. The results obtained confirm that the use of neuron networks improves the total harmonic distortion (THD) and minimizes power ripple. Works [15, 16] proposed the design of sensorless induction motor drive based on DPC technique. An effective sensorless strategy based on ANN is developed to estimate rotor's position and speed of induction motor. Simulation results confirm the performance of ANN based sensorless DPC induction motor drive in various conditions. The article [17] presents a study between HYN-DTC (Neural hysteresis Direct Torque Control) and fuzzy logic PI controller applied to an induction motor. The first method has less THD. The work [18] proposed a new DPC strategy based on a second order sliding mode controller of a doubly fed induction generator (DFIG) integrated in a wind energy conversion system. In the first step it proposed to use a five-level inverter based on the neural space vector pulse width modulation to supply the DFIG rotor side. The results obtained confirm that the use of neural hysteresis controller decrease the THD. The article [19] presents an ANN based DPC of bidirectional 2-level pulse width modulated (PWM) rectifier. Instead of the traditional PI controller, ANN controller is used in this paper to reduce the peak overshoot and ripple in active power. The work [20] a direct power control strategy for a 2.25 kW DFIG is proposed and implemented using a controller based on an ANN with the multilayer perceptron (MLP) structure, which allows the control of the coupled and nonlinear system. All the PI controllers and rotor current estimation block that generated the set of samples for training process were replaced with success by a single MLP controller with twenty hidden neurons. The results have shown that the DPC approach combined with the MLP controller maintain the features of the DPC and adds the inherent characteristic of an ANN controller, more specifically the capability of controlling the coupled and nonlinear system and to generalize the performance to the whole range of operation considered in the training data.

Aim. In this paper a DPC strategy for a PMSG is proposed and implemented using a controller based on an ANN structure. The ANN controller replaces the PI and hysteresis controllers.

Research path followed in this article. The flowchart (Fig. 1) shows the steps followed in this article. The disadvantages of each technique are cited as well as the solutions given in the literature. We always opt for a simple and optimal solution.

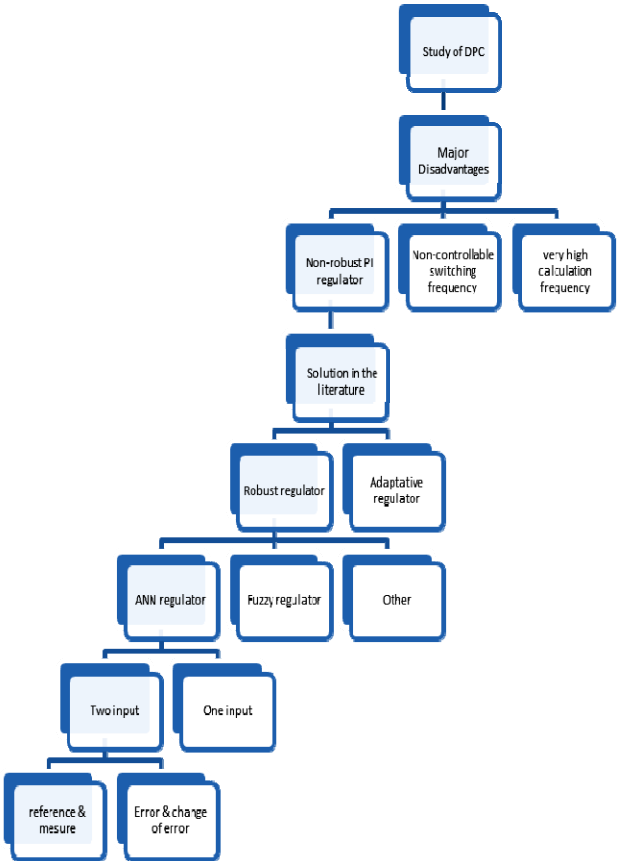

Fig. 1. Flowchart showing the research steps for this article

PMSG modeling. The mathematical model of the PMSG obeys certain essential assumptions simplifying:

- the absence of saturation in the magnetic circuit;
- the sinusoidal distribution of the FMM created by the stator windings;
- hysteresis is neglected with eddy currents and skin effect;
- the notching effect is negligible;
- the resistance of the windings does not vary with temperature.

The structure of the PMSG has a three-phase stator winding. The rotor excitation is created by permanent magnets at the rotor. These magnets are assumed to be rigid and of permeability similar to that of air [21, 22]:

$$U_{ds} = -R_s I_{ds} - L_d \frac{d}{dt} I_{ds} + \omega_r L_{qs} I_{qs} ; \quad (1)$$

$$U_{qs} = -R_s I_q - L_q \frac{d}{dt} I_{qs} - \omega_r L_d I_{ds} + \omega_r \varphi_f , \quad (2)$$

where U_{ds} and U_{qs} are the stator voltage components; R_s is the stator resistance; L_d and L_q are the components of stator inductances; I_{ds} and I_{qs} are the components of stator current; φ_f is the permanent magnet flux; ω_r is the electric pulsation.

The electrical rotation speed is given by:

$$w_e = p \cdot w, \quad (3)$$

where p is the number of pairs of poles; w is the mechanical speed.

The electromagnetic torque C_e represented by:

$$C_e = \frac{3}{2} \cdot p \cdot \varphi_f \cdot I_{qS} . \quad (4)$$

The power equations are provided by:

$$P = \frac{3}{2} \cdot (U_{dS} \cdot I_{dS} - U_{qS} \cdot I_{qS}) ; \quad (5)$$

$$Q = \frac{3}{2} \cdot (U_{qS} \cdot I_{dS} - V_{dS} \cdot I_{qS}) , \quad (6)$$

where P is the active power; Q is the reactive power.

Uncontrolled rectifier PWM. We have 3 phase line voltages and the fundamental line currents in [22]:

$$U_a = U_m \cos 2\omega t ; \quad (7)$$

$$U_b = U_m \cos(2\omega t + \frac{2\pi}{3}) ; \quad (8)$$

$$U_c = U_m \cos(2\omega t - \frac{2\pi}{3}) ; \quad (9)$$

$$I_a = I_m \cos(2\omega t + \varphi) ; \quad (10)$$

$$I_b = I_m \cos(2\omega t + \frac{2\pi}{3} + \varphi) ; \quad (11)$$

$$I_c = I_m \cos(2\omega t - \frac{2\pi}{3} + \varphi) , \quad (12)$$

where U_m, I_m are the amplitudes of the phase voltage and current respectively; ω is the rotational frequency; φ is the phase difference [23].

Line to line input voltages of PWM rectifier can be described as:

$$U_{sa} = (S_a - S_b) \cdot U_{dc}; \quad (13)$$

$$U_{sb} = (S_b - S_c) \cdot U_{dc}; \quad (14)$$

$$U_{sc} = (S_c - S_a) \cdot U_{dc}; \quad (15)$$

and phase voltages equations give by:

$$U_{sa} = \frac{2S_a - (S_b + S_c)}{3} \cdot U_{dc} ; \quad (16)$$

$$U_{sb} = \frac{2S_b - (S_a + S_c)}{3} \cdot U_{dc} ; \quad (17)$$

$$U_{sc} = \frac{2S_c - (S_a + S_b)}{3} \cdot U_{dc} , \quad (18)$$

where S_a, S_b, S_c are the switching states of the rectifier; U_{dc} is voltage rectifier.

DPC of PMSG. DPC appeared to be competitive with vector control technique. This control method was proposed in [24]. The DPC control is based on the selection of a voltage vector in such a way that the errors between the measured and reference quantities are reduced and maintained between the limits of the bands hysteresis [23, 25]. On the other hand, DPC control is an active and reactive power-based control technique with the advantages of robustness and rapid control (see Fig. 2) it is possible to express that of the reference power by [15]:

$$P_{ref} = U_{dc} \cdot I_{dc}, \quad (19)$$

where I_{dc} represents the rectifier output current.

Artificial neural network-based DPC. Neural networks have properties of learning, approximation and generalization, so they are of interest for the synthesis of such a command [17, 26]. ANN is a simplified mathematical formulation of biological neurons. They have the capacity of memorization, of generalization and especially of learning which is the most important phenomenon.

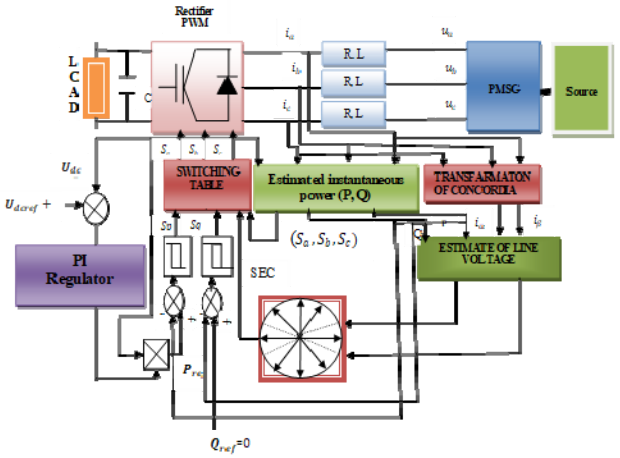

Fig. 2. Block diagram of the DPC

Structure of a neuron. The neuron is the fundamental cell of a network of artificial neurons. By analogy with the biological neuron, the neuron must be able to accomplish the following tasks: collect, process the data coming from the sending neurons and transmit the messages to the other neurons. The relation between the input and the output of the neuron can be given by the following equation:

$$S_i = F(a); \quad (20)$$

$$S_i = \sum_{j=0}^{N} W(i,j) \cdot x(j), \quad (21)$$

where the variables N, S_i, F, x and W respectively denote the number of inputs of the neural network, the output vector of the network, the activation function, the vector of the inputs of the neural network and the weight matrix.

We present in Fig. 3 the structure of a simple neuron.

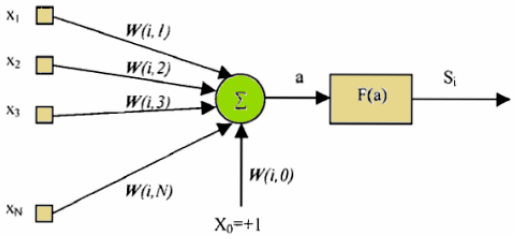

Fig. 3. Structure of a simple neuron

Structure of a single layered neural network. Layered network is a network whose neurons are organized in layers, the simplest form is the single layer network. All input signals are propagated from the input nodes to the output neural layer.

The number of input (nodes) and output neurons is generally related to the problem to be solved. The inputs will be propagated through the matrix of weights W to then obtain the output response (Fig. 4). The equivalent equation can be written in the form:

$$y_i = \sum_{i=0}^{N} W(i,j) \otimes x(i) , \quad (22)$$

where $x(i)$ is the input vector; $y(i)$ is the output vector; $W(i,j)$ is the weight of the neural network.

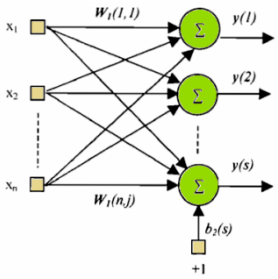

Fig. 4. Structure of a single layered neural network

ANN activation functions. The activation functions used in today's connection models are varied. We can identify three main types of best known functions: *Tansig*, *Logsig* and *Pureline*.

Artificial neural network (ANN) learning modes. Learning can be defined as the ability to store information that can be recalled later. The knowledge of a connection network is stored in the connection weights which will be determined during learning. The goal of learning for a network is to find a set of mimic weights that will error between the output of the network and the desired result.

Learning methods of neural networks.

- learning by backpropagation of the error;
- learning according to a gradient descent;
- learning according to the Quasi-Newton method.

Direct neural power control of PMSG. Figure 5 depicts the construction of the PMSG's direct neural power control (ANN-DPC). The PI voltage regulator and the active and reactive instantaneous power hysteresis regulators are replaced with neural controllers. To generate the ANN controller by MATLAB / Simulink or we have chosen 24 hidden layers for the voltage controller and 5 hidden layers for each hysteresis regulator. Figure 5 gives the block diagram proposed of ANN-DPC.

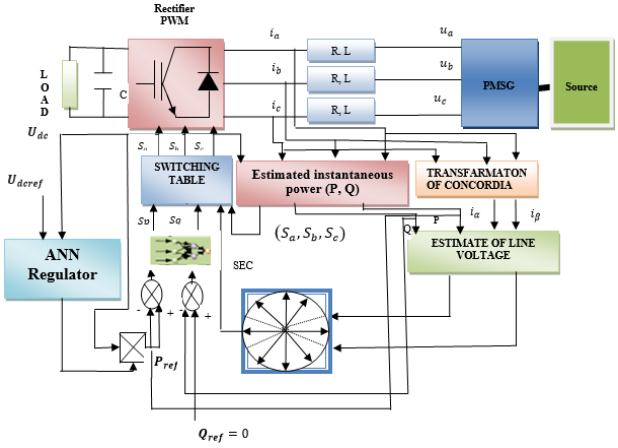

Fig. 5. Block diagram proposed of ANN-DPC

The activation functions are respectively of the «*tansig*» type for the hidden layers and «*pureline*» for the output layers (see Table A.3 in Appendix of this article). An algorithm of carries out the updating of the weights a biases of this network retropropagation called the Levenberg-Marquardt (LM) algorithm.

The representation of the internal structure of the neural voltage controller is shown in Fig. 6.

Figure 7 and 8 illustrates the internal structure of layers 1 and 2 of the neural voltage controller respectively.

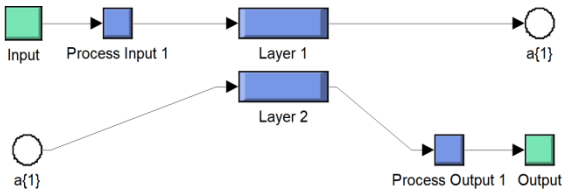

Fig. 6. Internal structure of the neural voltage controller

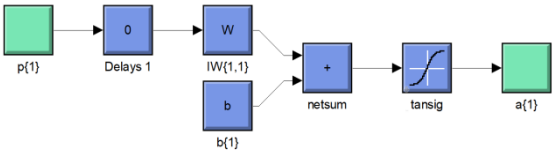

Fig. 7. Internal structure of layer 1

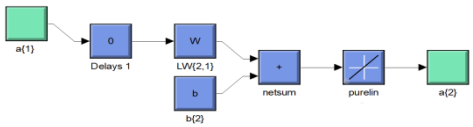

Fig. 8. Internal structure of layer 2

The training performance of ANN-DPC is shown on Fig. 9.

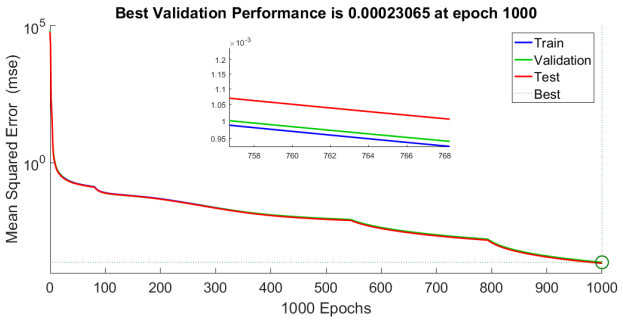

Fig. 9 The training performance of ANN-DPC

The three curves are superimposed. This result is justified in Fig. 10, where the training regression of ANN-DPC also is shown.

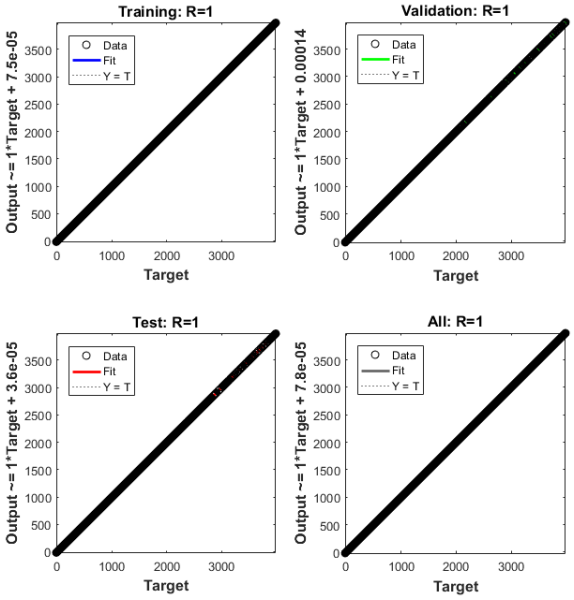

Fig. 10 Training regression of ANN-DPC

Simulation and results of DPC. In Fig. 11 the stator voltage and current of PMSG is shown.

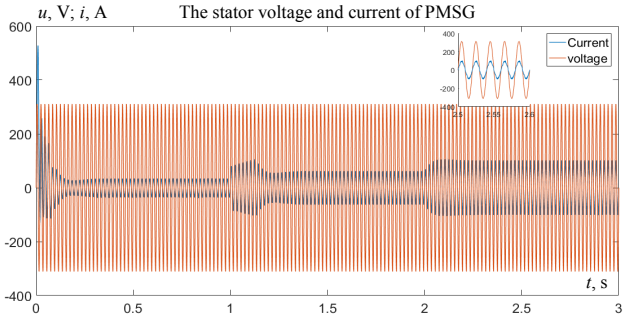

Fig. 11. The stator voltage and current of PMSG

In Fig. 12 the rectified voltage DPC is shown.

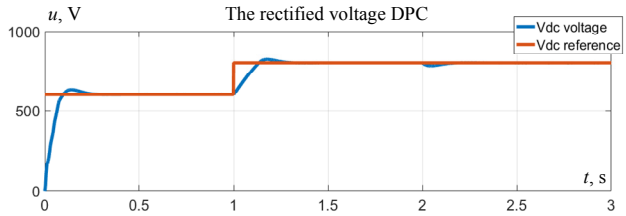

Fig. 12. The rectified voltage DPC

In Fig. 13 the active power DPC is shown.

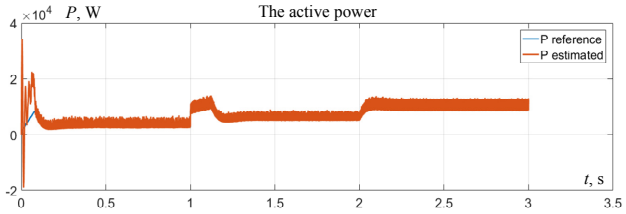

Fig. 13. The active power DPC

The results obtained when changing the DC bus reference voltage for the twelve sector control are shown in the next figures. Figure 14 shows a clear improvement in THD (7.3 %) compared to conventional DPC (12.71 %).

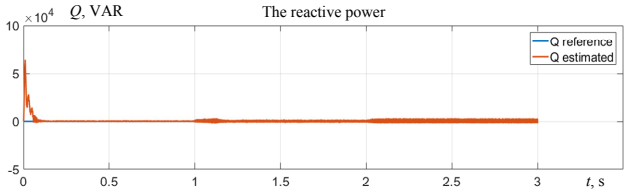

Fig. 14. The reactive power DPC

In Fig. 15 the line current i_b and its harmonic spectrum are shown.

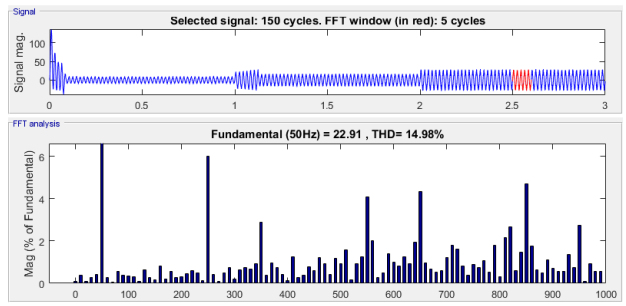

Fig. 15. The line current i_b and its harmonic spectrum

Simulation and results for ANN-DPC. Figure 16 shows that the DC bus voltage follows its reference without overshoot with minimal retraining time and allowable static error.

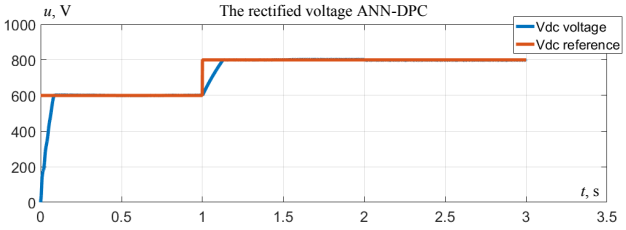

Fig. 16. Rectified voltage ANN-DPC

Figure 17 shows that the active energy follows its reference with the existence of peaks.

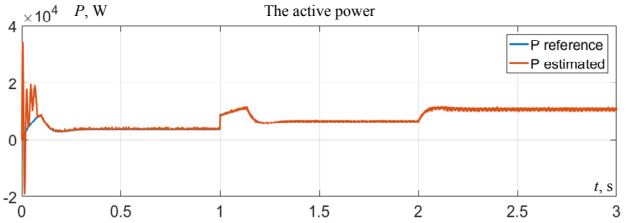

Fig. 17. The active power ANN-DPC

Figure 18 shows that reactive energy follows its reference with a peak passage at start-up.

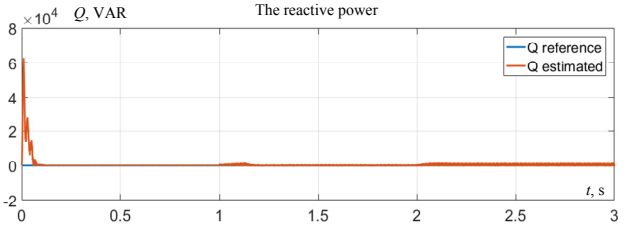

Fig. 18. The reactive power ANN-DPC

Figure 19 shows that the current is sinusoidal with a start peak passage.

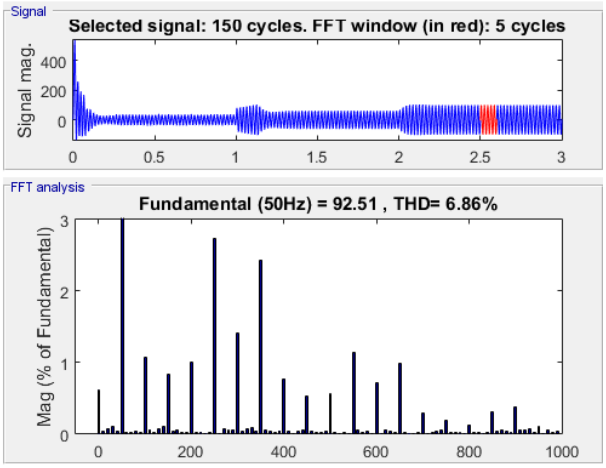

Fig. 19. The line current i_a and its harmonic spectrum ANN-DPC

Study comparative between DPC and ANN-DPC is shown on Table 1.

Table 1

Study comparative between DPC and ANN-DPC

		THD	Active power ripple	Reactive power ripple
Reference test	Classical DPC	12.71	bad	very good
	ANN-DPC	7.3	very good	good
Robustness test	Classical DPC	9.34	bad	bad
	ANN-DPC	6.86	very good	very good

As an example a comparative study with published results are shown on Table 2.

Table 2

A comparative study with published results

Method	THD, %	Ripple of power
1. ANN-DPC (ANN replaces PI controller) [19]	6.52	bad
2. HYN-DPC (ANN replaces Hysteresis controller) [1]	37.25	good
3. ANN-DPC (ANN replaces switching table) [1]	31.95	very good
4. Proposed method – ANN-DPC (combination of methods 1 and 2)	6.86	very good

Conclusions.

In this paper, a direct power control (DPC) is proposed for controlling the PWM rectifier supplied by a PMSG in terms of rapid control of active and reactive power. Decoupled active and reactive power control is achieved without the use of a decoupling system or a change in coordinates. DC voltage is controlled to a consistent incentive in all conditions. The application of a new scheme by replacing the PI and hysteresis regulators has been applied in order to minimize the THD and a better control of the instantaneous powers in terms of speed and ripple rate. The simulation results confirm the effectiveness of the applied technique:

- the sinusoidal form of the line current;
- the current must be in phase with the voltage;
- reactive energy compensation
- a low THD;
- ripple rate of powers;
- time response of DC voltage.

Finally, we prove that the method (ANN-DPC) is the best compared to the classic DPC control.

APPENDIX

Table A.1

PMSG parameters

Parameter	Value
Direct stator inductance L_d, H	0.012
Stator quadrature inductance L_q, H	0.0211
Permanent magnet flux φ_f, Wb	0.9
Stator resistance R_s, Ω	0.895
Inertia J, kg·m^2	0.00141
Number of poles n_p	3
Friction force F, N·m/rad·s	0

Table A.2

Rectifier parameter

Parameter	Value
Line resistance R_l, Ω	0.2
Line inductance L, H	0.011
Filtering capacity C, F	0.0047
DC voltage reference U_{ldcref}, V	600-800

Table A.3

Parameters of Levenberg-Marquardt (LM) algorithm

LM parameters	V_{dc} controller	H_p, H_q*
Number of hidden layers	24	5
Learning rate	0.002	0.002
Number of iterations (epochs)	1000	200
Convergence acceleration rate	0.9	0.9
Goal	0	0
Activation function	*tansig*	*tansig*

*H_p, H_q are respectively hysteresis active and reactive power controllers.

Conflict of interest. The authors declare that they have no conflicts of interest.

REFERENCES

1. Ghouizil A., Achour D., Benbouhenni H. Etude comparative entre la commande DPC, DPC-HYN et DPC-RNA de la GSAP. *Journal of Advanced Research in Science and Technology*, 2018, vol. 5, no. 2, pp. 735-752. (Fra). Available at: https://www.asjp.cerist.dz/en/downArticle/112/5/2/59632 (accessed 15 May 2021).

2. Multon B. Historique des machines électriques et plus particulièrement des machines à réluctance variable. *La Revue 3 E. I, Société de l'électricité, de l'électronique et des technologies de l'information et de la communication*, 1995, pp. 3-8. (Fra). Available at: https://hal.archives-ouvertes.fr/hal-00674038/document (accessed 15 May 2021).

3. Hemieda A.M., Farag W.A., Maghoub O.A. Modeling and control of direct driven PMSG for ultra large wind turbines. *World Academy of Science, Engineering and Technology*, 2011, vol. 59, pp. 918-924. Available at: https://scholar.cu.edu.eg/sites/default/files/wael_farag/files/modeling_and_control_of_direct_driven_pmsg_for_ultra_large_wind_turbines.pdf (accessed 15 May 2021).

4. Allagui M., Hasnaoui O.B.K., Belhadj J. A 2 MW direct drive wind turbine; vector control and direct torque control techniques comparison. *Journal of Energy in Southern Africa*, 2014, vol. 25, no. 2, pp. 117-126. doi: https://doi.org/10.17159/2413-3051/2014/v25i2a2679.

5. Errami Y., Ouassaid M., Cherkaoui M., Maaroufi M. Variable structure sliding mode control and direct torque control of wind power generation system based on the PM synchronous generator. *Journal of Electrical Engineering*, 2015, vol. 66, no. 3, pp. 121-131. doi: https://doi.org/10.2478/jee-2015-0020.

6. Freire N,. Estima J., Cardoso A. A comparative analysis of PMSG drives based on vector control and direct control techniques for wind turbine applications, *Przeglad Elektrotechniczny*, 2012, vol. 88, no. 1a, pp. 184-187. Available at: http://pe.org.pl/articles/2012/1a/39.pdf (accessed 15 May 2021).

7. Merzoug M.S., Benall H., Louze L. Sliding Mode Control (SMC) Of Permanent Magnet Synchronous Generators (PMSG). *Energy Procedia*, 2012, vol. 18, pp. 43-52. doi: https://doi.org/10.1016/j.egypro.2012.05.016.

8. Mendis N., Muttaqi K.M., Perera S. Management of battery-supercapacitor hybrid energy storage and synchronous condenser for isolated operation of PMSG based variable-speed wind turbine generating systems. *IEEE Transactions on Smart Grid*, 2014, vol. 5, no. 2, pp. 944-953. doi: https://doi.org/10.1109/tsg.2013.2287874.

9. Gehlot N.S., Alsina P.J. A comparison of control strategies of robotic manipulators using neural networks. *Proceedings of the 1992 International Conference on Industrial Electronics, Control, Instrumentation, and Automation*, 1992, vol. 2, pp. 688-693. doi: https://doi.org/10.1109/IECON.1992.254549.

10. Mavrovouniotis M.L., Chang S. *Numerical recipes in C*. New York, Cambridge University Press, 1990.

11. Ozdamar O., Yaylali I., Jayaker P., Lopez C.N. Inversion of multilayer networks. *Int. Joint. Conf. Neural Networks*, Washington, June 1989, pp. 425-430.

12. Narendra K.S., Mukhopadhyay S. Intelligent control using neural networks. *IEEE Control Systems Magazine*, 1992, vol. 12, no. 2, pp. 11-18. doi: https://doi.org/10.1109/37.126848.

13. Watrous R.L. Learning algorithms for connectionist networks: applied gradien methods of nonlinear optimization. *International Journal of Power Electronics and Drive System*, 1988, vol. 8,no. 4, pp. 619-627.

14. Hassan Adel A., Abo-Zaid S., Refky A. Improvement of direct torque control of induction motor drives using neuro-

fuzzy controller. *Journal of Multidisciplinary Engineering Science and Technology*, 2015, vol. 2, no. 10, pp. 2913-2918. Available at: https://www.jmest.org/wp-content/uploads/JMESTN42351145.pdf (accessed 5 May 2021).
15. Seyoum D., Rahman M.F., Grantham C. Terminal voltage control of a wind turbine driven isolated induction generator using stator oriented field control. *Eighteenth Annual IEEE Applied Power Electronics Conference and Exposition, 2003. APEC '03*, pp. 846-852 vol. 2. doi: https://doi.org/10.1109/apec.2003.1179315.
16. Halvaei Niasar A., Rahimi Khoei H. Sensorless Direct Power Control of Induction Motor Drive Using Artificial Neural Network. *Advances in Artificial Neural Systems*, 2015, vol. 2015, pp. 1-9. doi: https://doi.org/10.1155/2015/318589.
17. Benbouhenni H., Boudjema Z. Comparative study between neural hysteresis, fuzzy PI, and neural switching table for an IM DTC control. *International journal of fuzzy systems and advanced applications*, 2018, vol. 5, pp. 23-34. Available at: http://www.naun.org/main/NAUN/fuzzy/2018/a082017-063.pdf (accessed 15 May 2021).
18. Benbouhenni H. Robust direct power control of a DFIG fed by a five- level NPC inverter using neural SVPWM technique. *TECNICA ITALIANA-Italian Journal of Engineering Science*, 2021, vol. 65, no. 1, pp. 119-128. doi: https://doi.org/10.18280/ti-ijes.650118.
19. Jayachandra B., Mahesh A. ANN Based Direct Power Control of 2-level PWM Rectifier. *2018 International Conference on Power Energy, Environment and Intelligent Control (PEEIC)*, 2018, pp. 623-627. doi: https://doi.org/10.1109/peeic.2018.8665617.
20. Andreoli de Marchi R., Sergio Dainez P., Von Zuben F.J., Bim E. A neural network controller for the direct power control of doubly fed induction generator. *Eletrônica de Potência*, 2013, vol. 18, no. 3, pp. 1038-1046. doi: https://doi.org/10.18618/rep.2013.3.10381046.
21. Boukhechem I., Boukadoum A., Boukelkoul L., Lebied R. Sensorless direct power control for three-phase grid side converter integrated into wind turbine system under disturbed grid voltages. *Electrical Engineering & Electromechanics*, 2020, no. 3, pp. 48-57. doi: https://doi.org/10.20998/2074-272x.2020.3.08.
22. Lebied R., Lalalou R., Benalla H., Nebti K., Boukhechem I. Ameliorate direct power control of standalone wind energy generation system based on permanent magnet synchronous generator by using fuzzy logic control. *Electrical Engineering & Electromechanics*, 2020, no. 6, pp. 63-70. doi: https://doi.org/10.20998/2074-272X.2020.6.09.
23. Djeriri Y., Meroufel A., Massoum A., Boudjema Z. Direct power control of a doubly fed induction generator based wind energy conversion systems including a storage unit. *Journal of Electrical Engineering*, 2014, vol. 14 , no. 1, pp. 196-203.
24. Noguchi T., Tomiki H., Kondo S., Takahashi I. Direct power control of PWM converter without power-source voltage sensors. *IEEE Transactions on Industry Applications*, 1998, vol. 34, no. 3, pp. 473-479. doi: https://doi.org/10.1109/28.673716.
25. Zolfaghar M., Taher S.A., Munuz D.V. Neural network-based sensorless direct power control of permanent magnet synchronous motor. *Ain Shams Engineering Journal*, 2016, vol. 7, no. 2, pp. 729-740. doi: https://doi.org/10.1016/j.asej.2016.01.002.
26. Micu D.D., Czumbil L., Christoforidis G., Simion E. Neural networks applied in electromagnetic interference problems, *Revue roumaine des sciences techniques. Série Électrotechnique et Énergétique*, 2012, vol. 57, no. 2, pp. 162-171. Available at: http://revue.elth.pub.ro/viewpdf.php?id=338 (accessed 15 May 2021).

Received 25.08.2021
Accepted 20.10.2021
Published 03.12.2021

Kamel Akkouchi [1]*, PhD,*
Lazhar Rahmani [2]*, Professor of Electrical Engineering,*
Ryma Lebied [3]*, PhD,*
[1] Electrical Engineering Laboratory of Constantine (LGEC),
Department of Electrical Engineering,
University of Constantine 1,
25000 Constantine, Algeria.
[2] Automatic Laboratory of Setif (LAS),
University of Ferhat Abbes Setif,
19000 Setif, Algeria
[3] Electrotechnical Laboratory Skikda (LES),
University 20 August 1955,
26 Road El Hadaiek 21000, Skikda, Algeria.
e-mail: akkouchi.kamel@umc.edu.dz (Corresponding author),
lazhar-rah@univ-setif.dz,
r.lebied@univ-skikda.dz

How to cite this article:
Akkouchi K., Rahmani L., Lebied R. New application of artificial neural network-based direct power control for permanent magnet synchronous generator. *Electrical Engineering & Electromechanics*, 2021, no. 6, pp. 18-24. doi: https://doi.org/10.20998/2074-272X.2021.6.03.

UDC 621.318 https://doi.org/10.20998/2074-272X.2021.6.04

Yu.V. Batygin, S.O. Shinderuk, E.O. Chaplygin

Mutual influence of currents in a flat inductor system with solenoid between two massive conductors

Introduction. *Inductor systems, as tools for metal processing, are widely used in industrial technologies using the energy of powerful pulsed electromagnetic fields.* ***Problem.*** *A common disadvantage of the known works on the creation of tools for magnetic-pulse impact on conductive objects is the use physical and mathematical models, in which the exciting currents do not depend on the ongoing electromagnetic processes. Such the assumption distorts the picture of the real energy in the working area of the inductor system.* ***Goal.*** *To obtain design relationships and numerical estimations of the mutual influence of exciting and induced currents of a flat inductor system with a circular solenoid located between massive well-conducting objects, moreover to carry out a theoretical analysis of electromagnetic processes in this system.* ***Methodology.*** *Applied integrating Maxwell equations using the Laplace and Fourier-Bessel integral transforms in the approximation of the ideal conductivity of the metal objects to be processed.* ***Results****. The calculated relationships for the theoretical analysis of electromagnetic processes are obtained in the high-frequency approximation. It is shown that the inductance of the studied system decreases as the objects being processed approach the solenoid and increases as they move away from it. It is found that for the invariability of the power indicators, of the proposed tool, a corresponding correction of the amplitude (on average up to 20 times) of the exciting current is necessary in the solenoid winding.* ***Originality****. For the first time, the tool design with a circular solenoid located between the massive metal objects is proposed for flat magnetic-pulse stamping. As a result of the theoretical analysis, the influence of electromagnetic processes on the currents flowing in the system is confirmed.* ***Practical significance.*** *The use of the results obtained will allow to increase the efficiency of the tool of magnetic-pulse technologies, and to reduce the energy costs for performing the specified production operations.* References 19, figures 2.

Key words: **magnetic-pulse stamping, sheet metals, electromagnetic fields, inductor systems, circular solenoid, massive conductor.**

В роботі розглянута плоска індукторна система з круговим соленоїдом, розташованим між масивними добре провідними об'єктами. Така конструкція спрямована не тільки на підвищення ефективності інструменту магнітно-імпульсних технологій, та на зниження енергетичних витрат на виконання заданої виробничої операції. Інтегруванням рівнянь Максвелла з використанням інтегральних перетворень Лапласа і Фур'є-Бесселя в наближенні ідеальної провідності металевих об'єктів, що підлягають обробці, аналітично отримано математичну модель системи. В рамках поставленої мети отримано розрахункові співвідношення і проведено теоретичний аналіз електромагнітних процесів в плоскій індукторній системі з круговим соленоїдом, що розміщений між масивними добре провідними об'єктами, а також проведено чисельні оцінки взаємного впливу збуджуючих і індукованих струмів. Результати аналізу електромагнітних процесів показали, що для незмінності силових показників запропонованого інструменту магнітно-імпульсного штампування необхідна відповідна корекція амплітуди збуджуючого струму в обмотці соленоїда – джерела діючих електромагнітних полів. Бібл. 19, рис. 2.

Ключові слова: **магнітно-імпульсне штампування, листові метали, електромагнітні поля, індукторні системи, круговий соленоїд, масивний провідник.**

В работе рассмотрена плоская индукторная система с круговым соленоидом, расположенным между массивными хорошо проводящими объектами. Такая конструкция направлена не только на повышение эффективности инструмента магнитно-импульсных технологий, но и снижение энергетических затрат на выполнение заданной производственной операции. Интегрированием уравнений Максвелла с использованием интегральных преобразований Лапласа и Фурье-Бесселя в приближении идеальной проводимости подлежащих обработке металлических объектов аналитически получено математическую модель системы. В рамках поставленной цели получены расчётные соотношения и проведен теоретический анализа электромагнитных процессов в плоской индукторной системе с круговым соленоидом, размещённым между массивными хорошо проводящими объектами, а также проведены численные оценки взаимного влияния возбуждающих и индуцированных токов. Результаты анализа электромагнитных процессов показали, что для неизменности силовых показателей предложенного инструмента магнитно-импульсной штамповки необходима соответствующая коррекция амплитуды возбуждающего тока в обмотке соленоида – источника действующих электромагнитных полей. Библ. 19, рис. 2.

Ключевые слова: **магнитно-импульсная штамповка, листовые металлы, электромагнитные поля, индукторные системы, круговой соленоид, массивный проводник.**

Introduction. Problem definition in general. Inductor systems, as tools for metal processing, are widely used in industrial technologies using the energy of powerful pulsed electromagnetic fields. The design of induction systems is determined by the type of given production operation (for example, «distribution», «crimping», «flat stamping», etc.). Note that their successful practical implementation, as described in the modern special literature, is carried out in the framework of the so-called «traditional» magnetic pulse treatment of metals (MPTM) or in Western terminology Electromagnetic Metals Forming (EMF). As practice has shown, the effectiveness of this technology is possible

only in the range of sufficiently high operating frequencies of acting fields and high values of electrical conductivity of the processed objects. From a physical point of view, the natural Lorentz repulsion of the conductor from the instrument with the method, called «magnetic pressure» [1-4], is used here.

The development of electromagnetic technologies and increasing requirements for their efficiency has led to the creation of new types of induction systems. A number of production operations initiated a new direction of magnetic pulse processing of metals, based on the transformation of natural Lorentz repulsion in the attraction of the processed object [5-9]. As part of the «traditional» magnetic pulse treatment of metals, it seems a priori, increase in the productivity of flat stamping operations of sheet metal products is possible with the help of so-called «two-sided induction systems», where the solenoid is placed between objects of force action. The development of new tools requires the study of the processes of electromagnetic effects of exciting and induced currents. The relevance of such works is beyond doubt. The obtained results will allow to take a new approach to the problems of productivity, to increase the efficiency of inductor systems and expand the range of processed objects.

Literature review. Analysis of basic research and publications and problem definition. The two-sided arrangement of sheet metals relative to the source of the magnetic field (solenoid) takes place in induction systems, where the natural Lorentz repulsion is transformed into the attraction of a specified area of the processed object. Structurally, such tools consist of flat layered: the auxiliary screen, which conducts electric current, the circular solenoid and, naturally, the sheet metal to be deformed. The currents induced in the screen and the metal being processed are unidirectional. According to Ampere law, a certain area of sheet metal will be attracted to the plane of the rigidly fixed screen [10]. This principle of operation is also used in systems of automated supply of aluminum sheets to the working area of the stamping equipment of US car plants [11]. Practical aspects of MPTM development in the direction of attracting specified areas of sheet metals and creating appropriate tools for removing dents are described in [2, 3, 12]. Note that, mainly, magnetic-pulse attraction has found application in advanced technologies for the restoration of damaged coatings of car bodies [9, 10, 12, 13].

Object of study. Consider the induction effects in tools for flat magnetic-pulse stamping of solid sheet metal products with high electrical conductivity, where the solenoid is placed between two objects of force action. The physical idea of such a design of the inductor system involves the concentration of energy of the excitation field in the space between two conductors. Unlike the known tools for «traditional» flat magnetic pulse stamping, where the solenoid is placed over a single object of force action, this proposal reduces the scattering of energy generated in the surrounding space.

A common disadvantage of the known works on the creation of instruments of force magnetic-pulse influence on conductive objects (both attraction and repulsion) is the use of physical and mathematical models in which the excitation currents are accepted given and independent on electromagnetic processes. Thus, in [9] in inductor systems, mechanical forces in the form of attractive forces and their distribution in the system were considered, but the mutual influence of currents in the inductor system remained unexplored. We should also mention classical analytical [14, 15] and modern numerical models, for example, in [16, 17].

From a phenomenological point of view, it is obvious that such an assumption in the definition of the electrodynamic problems to be solved distorts the picture of real energy in the working zone of the inductor system.

The goal of the paper is to obtain calculation relationships and to carry out theoretical analysis of electromagnetic processes in a flat inductor system with a circular solenoid placed between massive well-conducting objects, as well as to obtain numerical estimations of the mutual influence of excitation and induced currents. We emphasize the relevance of this goal, which is aimed not only at improving the efficiency of the tool of magnetic pulse technology, but also to reduce energy costs to perform a specified production operation.

Presentation of the main material. Analytical dependencies, numerical estimations. Concerning problems in MPTM inductor systems, we begin consideration with definition of problems which is identical for all researches of the proceeding electrodynamic processes [2, 8-12].

Assumptions for solving the formulated problem:

- a physical and mathematical model of the inductor system is symmetrical about the plane of the exciting solenoid (Fig. 1);
- a cylindrical coordinate system is adopted;
- a inductor system is assumed to be axially symmetric, i.e. $\frac{\partial}{\partial \varphi} = 0$, where φ is the azimuthal angle;
- a solenoid is assumed to be so thin that its metal does not affect the electromagnetic processes occurring in the system ($\Delta \to 0$);
- an azimuthal harmonic current $J(t) = J_m \cdot \sin(\omega \cdot t)$ flows in the solenoid winding, where J_m is the amplitude; ω is the cyclic frequency; t is the time;
- sheet metals (plates that conduct electricity) are quite massive and have a high specific conductivity;
- in the system the azimuthal component of the electric field strength $E_\varphi(t, r, z) \neq 0$ is excited, as well as the radial r and normal z components of the magnetic field strength vector $H_r(t, r, z) \neq 0$ and $H_z(t, r, z) \neq 0$ accordingly;
- electromagnetic processes are assumed to be quasi-stationary, so $(\omega \cdot l / c) << 1$, where c is the speed of light in vacuum; l is the largest characteristic size of the system.

The evaluation of the characteristics of the mutual influence of induced and excitation currents can be carried out based on the equality of the average values of the normal components of the magnetic flux density in the inner window of the solenoid at different distances between it and the plates.

In addition to the accepted assumptions, it should be noted that in practice the massiveness and high electrical conductivity of sheet metals means the operation of the inductor system in high-frequency temporal mode, when there is no penetration of fields through the processed objects. Within these studies, they can be considered as ideal conductors for which $\omega\cdot\tau >> 1$, where $\omega\cdot\tau$ is the «electrodynamic» thickness (the introduction of the term is justified in [9, 10]); $\tau = \mu_0\cdot\gamma\cdot d^2$ is the characteristic time of penetration of the field into the non-magnetic conducting layer; μ_0 is the magnetic permeability of the vacuum; γ is the specific electrical conductivity, and d is the geometric thickness.

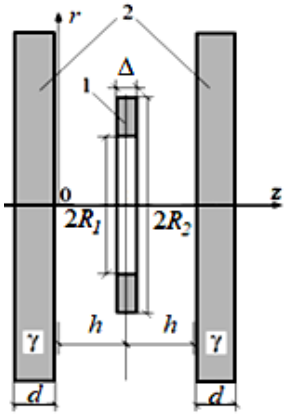

Fig. 1. Calculation model of flat inductor system:
1 – circular solenoid (Δ– thickness, $R_{1,2}$ – inner and outer radii);
2 – sheet metals (d – thickness, γ – specific electrical conductivity)

It is a priori obvious that the influence of induced currents on electromagnetic processes should decrease with the removal of sheet metals and increase with their approach to the exciting solenoid. In this regard, to describe the studied effect, we can identify and propose two main characteristics of the electromagnetic processes that take place. The first one is the ratio of the inductance of the system at different distances between the solenoid and the sheet metals to the inductance at infinite distance of the latter. The second one is the corresponding ratio of the resulting current in the solenoid winding to the excitation current in the absence of sheet metals. Note that the latter characteristic can be taken as a quantitative indicator of the effect of induced currents on the current in the solenoid winding.

Based on the accepted assumption of equality of average values of normal components of magnetic flux density in the inner window of the solenoid at different distances of sheet metals, we can obtain the following dependencies to assess the mutual influence of excitation and induced currents [14]:

$$\begin{cases} \overline{B}_{\rm h} = \overline{B}_{\infty}; \\ \dfrac{J_{\rm h}}{J_{\infty}} = \dfrac{L_{\infty}}{L_{\rm h}}; \end{cases} \tag{1}$$

where $\overline{B}_{\rm h}$, $J_{\rm h}$, $L_{\rm h}$ are the average value of the normal component of the magnetic flux density, the current in the solenoid winding and the inductance of the system at the final distance h between the solenoid and the sheet metals, respectively; $\overline{B}_{\infty}$, J_{∞}, L_{∞} are the average value of the normal component of the flux density, the current in the solenoid winding and the inductance of the system in the absence of sheet metals (at $h \to \infty$), respectively.

It should be noted that effectively relations (1) are consistent with the known dependencies [14]. Indeed, the amplitudes of the currents in the windings are inversely proportional to their inductance.

In accordance with the formulated goal, we turn to the calculation model in Fig. 1, for which we write a system of Maxwell equations in the space of L-images according to Laplace [9, 10, 18, 19]

$$\begin{cases} \dfrac{\partial E_{\varphi}(p,r,z)}{\partial z} = \mu_0 p H_{\rm r}(p,r,z); \\ \dfrac{1}{r}\cdot\dfrac{\partial}{\partial r}\cdot\left(r\cdot E_{\varphi}(p,r,z)\right) = -\mu_0 p H_{\rm z}(p,r,z); \\ \dfrac{\partial H_{\rm r}(p,r,z)}{\partial z} - \dfrac{\partial H_{\rm z}(p,r,z)}{\partial r} = j_{\varphi 0}(p,r,z), \end{cases} \tag{2}$$

where

$E_{\varphi}(p,r,z) = {\rm L}\left\{E_{\varphi}(t,r,z)\right\}$, $H_{\rm r,z}(p,r,z) = {\rm L}\left\{H_{\rm r,z}(t,r,z)\right\}$,

$j_{\varphi 0}(p,r,z) = \left\{j_{\varphi 0}(t,r,z)\right\}$, $j_{\varphi 0}(t,r,z)$ is the current density in the solenoid, $j_{\varphi 0}(p,r,z) = j_{\rm m}\cdot g(t)\cdot f(r)\cdot\delta(z-h)$, $g(t)$ is the temporal dependence; $f(r)$ is the radial dependence; $\delta(z-h)$ is the Dirac function [18].

We integrate the system of equations (1) in the same way as it was done earlier in [2, 9, 10].

The geometry of the inductor system and the accepted assumptions allow us to apply the Fourier-Bessel integral transform [18, 19].

For L-images of the excited electric field strength $E_{\varphi}(p, r, z)$ we write that

$$\begin{cases} E_{\varphi}(p,r,z) = \displaystyle\int_0^{\infty} E_{\varphi}(p,\lambda,z)\cdot\lambda\cdot J_1(\lambda r)\, d\lambda, \\ E_{\varphi}(p,\lambda,z) = \displaystyle\int_0^{\infty} E_{\varphi}(p,r,z)\cdot r\cdot J_1(\lambda r)\, dr, \end{cases} \tag{3}$$

where $E_{\varphi}(p, \lambda, z)$ is the image of electric field strength in Fourier-Bessel space; λ is the integral transform parameter; $J_1(\lambda r)$ is the Bessel function of the first order.

Omitting intermediate mathematical transformations, from the system (1) using the integral image (2) we write the differential equation for the azimuthal component of the excited electric field strength in the inner cavity of the considered inductor system [18].

$$\frac{\partial^2 E_\varphi(p,\lambda,z)}{\partial z^2}-\lambda^2\cdot E_\varphi(p,\lambda,z)=K(p,\lambda)\cdot\delta(z-h),\quad (4)$$

where $K(p,\lambda)=\mu_0 p\cdot j_m\cdot g(p)\cdot f(\lambda)$; $j_m=\frac{J_m}{(R_2-R_1)}$ is the excited current density;

$$g(p)=\mathrm{L}\{g(t)\};\ f(\lambda)=\int_{R_1}^{R_2} f(r)\cdot r\cdot J_1(\lambda r)\,dr.$$

The general integral of the ordinary differential equation (4) has the form [18]:

$$E_\varphi(p,\lambda,z)=C_1\cdot e^{\lambda z}+C_2\cdot e^{-\lambda z}+$$
$$+\frac{K(p,\lambda)}{\lambda}\cdot\eta(z-h)\cdot\mathrm{sh}\left(\lambda\cdot(z-h)\right),\quad (5)$$

where $C_{1,2}$ are the arbitrary integration constants; $\eta(z-h)$ is the Heaviside step function.

The accepted assumption of the absence of field penetration through sheet metals, as already mentioned, is described by the inequality $\omega\cdot\tau >> 1$ [2, 6], which corresponds to their «ideal» conductivity. Satisfying the boundary conditions of the continuity of the tangential components of the electromagnetic field strength vector on the surfaces of ideal conductors at $z = 0$ ($E_\varphi(p,\lambda,z=0)=0$) and $z = 2h$ ($E_\varphi(p,\lambda,z=2h)=0$) [14], we find a partial solution of equation (3). Substituting the coordinate $z = h$ into the obtained expression, we obtain the image of the excited high-frequency electric field in the inner window of a flat circular solenoid of the considered inductor system.

$$E_\varphi(p,\lambda,z=h)=-\frac{K(p,\lambda)}{2\lambda}\cdot\mathrm{th}(\lambda h).\quad (6)$$

The integral image (2) taking into account (5) takes the form:

$$E_\varphi(p,r,z)=-\int_0^\infty\frac{K(p,\lambda)}{2}\cdot\mathrm{th}(\lambda h)\cdot J_1(\lambda r)\,d\lambda.\quad (7)$$

The connection of the L-image of the normal component of the excited magnetic field strength with the φ-component of the electric field strength in the inner window of the solenoid is found by the second equation from the system (1) by substitution $z = h$

$$H_z(p,r,z=h)=-\frac{1}{\mu_0 p}\cdot\frac{1}{r}\cdot\frac{\partial}{\partial r}\cdot\left(r\cdot E_\varphi(p,r,z=h)\right).\quad (8)$$

By integrating expression (8) along the plane of the inner window of the solenoid, we determine the relationship of the magnetic flux with $E_\varphi(p, r, z = h)$

$$\Phi_h(p)=2\pi\mu_0\cdot\int_0^{R_1} H_z(p,r,z=h)rdr=$$
$$=-\frac{2\pi}{p}\cdot\left(r\cdot E_\varphi(p,r,z=h)\right)\Big|_0^{R_1}\quad (9)$$

Taking into account formulas (7), (9) after the transition to the space of the originals we find the amplitude dependence Φ_{hm} for the magnetic flux in the solenoid window of the inductor system. Omitting intermediate identical transformations, we obtain that

$$\Phi_{hm}=J_m\cdot\frac{\mu_0\pi R_1}{(R_2-R_1)}\cdot\int_0^\infty f(\lambda)\cdot\mathrm{th}(\lambda h)\cdot J_1(\lambda R_1)\,d\lambda.\quad (10)$$

The inductance of this system is found as the ratio of magnetic flux to excitation current [14].

After entering a new integration variable $y = \lambda R_1$ and perform the necessary identical transformations we obtain a convenient formula for calculating the inductance at any distance from the solenoid to the sheet metals

$$L_h=\frac{\mu_0\pi R_1^2}{(R_2-R_1)}\cdot\int_0^\infty\frac{f(y,R_{1,2})}{y^2}\cdot\mathrm{th}(\lambda h)\cdot J_1(y)\,dy,\quad (11)$$

where $f(y,R_{1,2})=\int_y^{\left(y\cdot\frac{R_2}{R_1}\right)} x\cdot J_1(x)\,dx.$

The limit transition in (11) for $h \to \infty$ gives an expression for the inductance of the actual solenoid winding in the absence of sheet metals

$$L_\infty=\lim_{h\to\infty}L_h=\frac{\mu_0\pi R_1^2}{(R_2-R_1)}\cdot\int_0^\infty\frac{f(y,R_{1,2})}{y^2}\cdot J_1(y)\,dy.\quad (12)$$

Ultimately, the use of relations (1), (11), (12) allows us to proceed to numerical estimations of the impact of induction effects on the characteristics of electromagnetic processes in the studied inductor system. The results of the calculations are presented in Fig. 2.

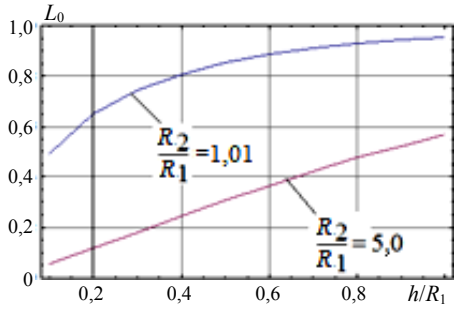

a

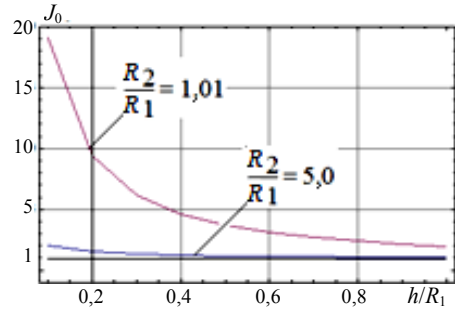

b

Fig. 2. Relative inductance (*a*) and relative current (*b*) in the solenoid winding of the inductor system

The main results of the calculations are formulated in the following provisions:

- the influence of induction effects on electromagnetic processes in the high-frequency mode of the studied

inductor system showed that its inductance increases with the removal of massive conductors and decreases as they approach the solenoid, as well as with increasing its radial size (Fig. 2,*a*);

- the mentioned decrease in inductance requires an increase in the current in the solenoid winding to maintain a constant value of the excited magnetic flux density and constant force indicators (Fig. 2,*b*);
- as follows from the calculated data, to maintain the characteristics of the studied inductor system, on average, a possible increase in the excitation current by ~20 times is required (Fig. 2,*b*).

Conclusions and prospects for further development. For the first time for flat magnetic pulse stamping the design of the tool with the circular solenoid placed between the massive well-conducting metal objects which are subject to processing is proposed.

In the approximation of high-frequency electromagnetic processes, the calculation relationships are obtained, which are used to perform theoretical analysis and numerical estimations of the characteristics of a flat inductor system with variation of the working gap between the solenoid – a source of the field and the objects being processed.

It is shown that the inductance, as the main characteristic of the studied system, decreases when the processed objects approach the solenoid and increases at a distance from it, which is physically explained by the interaction of electromagnetic fields of exciting and induced currents.

It is obtained that in order to keep the force indicators of the proposed tool of magnetic pulse stamping, it is necessary to accordingly and obligatory adjust the amplitude of the excitation current in the winding of the solenoid – a source of the acting electromagnetic fields.

In conclusion, the authors would like to note the reasoning that expands the scope of practical application of the results of the work performed. As it seems a priori, a similar design of a flat air current transformer (matching device in MPTM), where a multi-turn circular solenoid connected to a power source should be placed between single-turn solenoids with electrically parallel load output, which can significantly reduce energy dissipation into the surrounding space. Such a device can become an element of energy-saving technologies in modern converter engineering.

Conflict of interest. The authors of the paper declare no conflict of interest.

REFERENCES

1. Benenson W., Harris J.W., Stöcker H., Lutz H. *Handbook of Physics*. Springer Nature Switzerland AG, 2002. 1190 p. doi: https://doi.org/10.1007/0-387-21632-4.

2. Gnatov A., Argun S. New Method of Car Body Panel External Straightening: Tools of Method. *International Journal of Vehicular Technology*, 2015, vol. 2015, pp. 1-7. doi: https://doi.org/10.1155/2015/192958.

3. Kudasov Y.B., Surdin O.M., Platonov V.V., Kozabaranov R.V., Maslov D.A., Makarov I.V., Svetlov A.S., Popov E.Y. Metal plate deformation under magnetic field pulse of complex shape. *Journal of Applied Physics*, 2019, vol. 126, no. 8, p. 084901. doi: https://doi.org/10.1063/1.5108823.

4. Du L., Li X., Xia L., Zhang X., Lai Z., Han X., Li L., Cao Q. Numerical and experimental verification of an iterative coupling method for analyzing the Lorentz-force-driven sheet metal stamping process. *The International Journal of Advanced Manufacturing Technology*, 2021, vol. 115, no. 7-8, pp. 2161-2173. doi: https://doi.org/10.1007/s00170-021-07268-z.

5. Bay F., Jeanson A.-C., Zapata J.A. Electromagnetic Forming Processes: Material Behaviour and Computational Modelling. *Procedia Engineering*, 2014, vol. 81, pp. 793-800. doi: https://doi.org/10.1016/j.proeng.2014.10.078.

6. Ouyang S., Li C., Du L., Li X., Lai Z., Peng T., Han X., Cao Q., Li L. Electromagnetic forming of aluminum alloy sheet metal utilizing a low-frequency discharge: A new method for attractive forming. *Journal of Materials Processing Technology*, 2021, vol. 291, p. 117001. doi: https://doi.org/10.1016/j.jmatprotec.2020.117001.

7. Ouyang S., Du L., Cao Q., Li L. Electromagnetic attractive forming of aluminum alloy sheets utilizing a low-frequency half-wave current. *Materials and Manufacturing Processes*, 2021, pp. 1-9. doi: https://doi.org/10.1080/10426914.2021.1944197.

8. Batygin Y.V., Chaplygin E.A. Vortical currents in flat metallic sheet. *Electrical Engineering & Electromechanics*, 2006, no. 5, pp. 54-59. (Rus). Available at: http://eie.khpi.edu.ua/issue/view/6513/2466 (accessed 25 June 2021).

9. Turenko A.N., Batygin Yu.V., Gnatov A.V. *Impul'snye magnitnye polia dlia progressivnykh tekhnologii. T. 3. Teoriia i eksperiment pritiazheniia tonkostennykh metallov impul'snymi magnitnymi poliami* [Pulsed magnetic fields for advanced technologies. Vol. 3. Theory and experiment of the attraction of thin-walled metals by pulsed magnetic fields]. Kharkiv, KhNAHU Publ., 2009. 240 p. (Rus).

10. Batygin Yu., Barbashova M., Sabokar O. *Electromagnetic Metal Forming for Advanced Processing Technologies*. Cham, Springer International Publ. AG., 2018. 93 p. doi: https://doi.org/10.1007/978-3-319-74570-1.

11. Golovashchenko S.F., Batygin Yu.V. *Sheet metal blank destacker*. Patent US. US2018105373-A1, 04/19/2018.

12. Batygin Yu.V., Chaplygin E.A., Shinderuk S.A., Strelnikova V.A. The main inventions for technologies of the magnetic-pulsed attraction of the sheet metals. A brief review. *Electrical Engineering & Electromechanics*, 2018, no. 3, pp. 43-52. doi: https://doi.org/10.20998/2074-272X.2018.3.06.

13. Kudasov Y.B., Makarov I.V., Platonov V.V., Surdin O.M., Maslov D.A., Voronov S.L., Malyshev A.Y., Korshunov A.S., Popov E.Y., Svetlov A.S. An Experimental Setup for Studying the Deformation Dynamics of Metal Samples under Pulsed Magnetic Field. *Instruments and Experimental Techniques*, 2019, vol. 62, no. 1, pp. 88-92. doi: https://doi.org/10.1134/s0020441219010135.

14. Demirchyan K.S., Neiman L.R., Korovkin N.V., Chechurin V.L. *Teoreticheskie osnovy elektrotekhniki. 4 izd. T. 3* [Theoretical Foundations of Electrical Engineering, 4th ed., Vol. 3]. St. Petersburg, Peter Publ., 2006. 318 p. (Rus).

15. Isaev Yu., Vasilieva O. *Metody rascheta elektromagnitnykh polei* [Methods for calculating electromagnetic fields]. LAP Lambert Academic Publ., 2012. 172 p. (Rus).

16. Altenbach H., Konkin V., Lavinsky D., Morachkovsky O., Naumenko K. Verformungsanalyse elektrisch leitender metallischer Bauteile bei Magnetimpulsbearbeitung. *Forschung*

im Ingenieurwesen, 2018, vol. 82, no. 4, pp. 371-377. (Ger). doi: https://doi.org/10.1007/s10010-018-0285-x.
17. Lavinskii D.V., Morachkovskii O. K. Elastoplastic Deformation of Bodies Interacting Through Contact Under the Action of Pulsed Electromagnetic Field. *Strength of Materials*, 2016, vol. 48, no. 6, pp. 760-767. doi: https://doi.org/10.1007/s11223-017-9822-3.
18. Kantorovich L. *Mathematics for Natural Scientists. Fundamentals and Basics*. Springer Nature Switzerland AG, 2016. 526 p. doi: https://doi.org/10.1007/978-1-4939-2785-2.
19. Weber H., Ulrich H. *Laplace–, Fourier– und z–Transformation*. Springer Nature Switzerland AG, 2012. 236 p. doi: https://doi.org/10.1007/978-3-8348-8291-2.

Received 21.10.2021
Accepted 26.11.2021
Published 03.12.2021

Yu.V. Batygin[1], *Doctor of Technical Science, Professor,*
S.O. Shinderuk[1], *PhD, Associate Professor,*
E.O. Chaplygin[1], *PhD, Associate Professor,*
[1] Kharkiv National Automobile and Highway University,
25, Yaroslava Mudrogo Str., Kharkiv, 61002, Ukraine.
e-mail: yu.v.batygin@gmail.com,
s.shinderuk.2016102@ukr.net (Corresponding author),
chaplygin.e.a@gmail.com

How to cite this article:
Batygin Yu.V., Shinderuk S.O., Chaplygin E.O. Mutual influence of currents in a flat inductor system with solenoid between two massive conductors. *Electrical Engineering & Electromechanics*, 2021, no. 6, pp. 25-30. doi: https://doi.org/10.20998/2074-272X.2021.6.04.

UDC 621.3.022: 621.315.2(3) https://doi.org/10.20998/2074-272X.2021.6.05

M.I. Baranov, S.G. Buriakovskyi, V.V. Kniaziev

Destruction of polymer insulation and threshold amplitudes of current pulses of different temporal shapes for electric wires and cables in the low- and high-current circuits of pulse power engineering, electrical engineering and electronic devices

Goal. *Development of engineering method for settlement of threshold amplitudes I_{mpk} of single-pulse current $i_p(t)$ of different temporal shapes for electric wires and cables with polyethylene (PET), polyvinylchloride (PVC) and rubber (R) half-length insulation, used in modern pulsed power engineering, electrical engineering and electronics in their low- and high-current circuits.* ***Methodology.*** *Basis of the theoretical and applied electrical engineering, electrical power engineering, electrophysics bases of technique of high-voltage and large pulsed currents, bases of low- and high-current electronics, measuring technique, electromagnetic compatibility and standardization.* ***Results.*** *Development of engineering method is executed on close calculation determination of threshold amplitudes I_{mpk} of single-pulse axial-flow current $i_p(t)$ of different temporal shapes for electric wires and cables with copper (aluminum) current-carrying parts and PET, PVC and R half-length insulation, used in the ow- and high-current circuits of pulsed electrical power engineering, electrical engineering and electronics. Electrothermal resistibility of half-length insulation of the examined cable and wire products (CWP), proper maximum to the possible temperatures of heating of current-carrying and insulating parts of the probed wires and cables and shutting out the offensive of the phenomenon destruction in the indicated insulation of CWP, was fixed based on this method. Calculation analytical correlations are obtained for finding in probed CWP of threshold numeral values of I_{mpk} amplitudes of pulses of current $i_p(t)$, time-varying both on aperiodic dependence of type τ_f/τ_p with duration of their front τ_f and duration of their pulses τ_p and by law of exponential attenuation sinewave. It is shown that at $I_{mp}>I_{mpk}$ destruction of their half-length insulation, resulting in the decline of service life of CWP, will come from the thermal overheat of current-carrying parts of the examined electric wires and cables. The examples of practical application of the offered method are resulted upon settlement for a radiofrequency coaxial cable RC 50-4-11 with middle sizes is easily soiled with continuous PET insulation of threshold amplitudes of I_{mpk} of standard aperiodic pulses of current $i_p(t)$ from nano-, micro- and millisecond temporal ranges of shape of τ_f/τ_p=5 ns/200 ns, τ_f/τ_p=10 μs/350 μs and τ_f/τ_p=7 ms/160 ms. It is shown that with the proper growth of parameter $\tau_p>>\tau_f$ for flow on a continuous copper tendon and split copper shell of radiofrequency coaxial cable RC 50-4-11 with middle sizes is easily soiled indicated homopolar pulses of current $i_p(t)$ substantial diminishing of their threshold amplitudes of I_{mpk} (with 531,2 кА for the nanosecond pulse of current of type 5 ns/200 ns to 1.84 кА for the millisecond impulse of current of type of 7 ms/160 ms takes place).* ***Originality.*** *An engineering method is first developed for close settlement of threshold numeral values of I_{mpk} amplitudes of single-pulse axial-flow current $i_p(t)$ of arbitrary peak-temporal parameters for electric wires and cables with copper (aluminum) current-carrying parts and PET, PVC and R half-length insulation.* ***Practical value.*** *Application in electrical engineering practice of the offered engineering method for determination of threshold amplitudes I_{mpk} of the indicated pulses of axial-flow current $i_p(t)$ for the probed electric wires and cables will allow considerably to increase service life of examined CWP.* References 20, tables 2.

Key words: **electrical wires and cables with polymer insulation, electrothermal resistance of cable and wire products, destruction of insulation, threshold amplitudes of current pulses for wires and cables.**

Запропонована інженерна методика за розрахунковим визначенням порогових амплітуд I_{mpk} імпульсів струму $i_p(t)$ різної часової форми для електричних проводів і кабелів з поліетиленовою, полівінілхлоридною і гумовою ізоляцією, широко вживаних в галузі імпульсної енергетики, високовольтної сильнострумової техніки, вимірювальної техніки і електроніки, а також в системах імпульсного електроживлення, контролю, управління роботою і діагностики стану функціонування електротехнічних пристроїв різного загальногромадянського і військового призначення. В якості вихідного критеріального положення при виборі порогових амплітуд I_{mpk} імпульсів струму $i_p(t)$ довільних амплітудно-часових параметрів для вказаних проводів і кабелів була вибрана термічна стійкість їх поясної ізоляції, яка відповідає гранично допустимим короткочасним температурам нагріву мідних (алюмінієвих) і ізоляційних частин досліджуваних кабелів (проводів) і що не допускає настання явища деструкції в ізоляції даної кабельно-провідникової продукції. Приведені приклади практичного використання запропонованої методики за розрахунковим визначенням порогових амплітуд I_{mpk} стандартних аперіодичних імпульсів струму $i_p(t)$ часової форми 5 нс/200 нс, 10 мкс/350 мкс і 7 мс/160 мс для радіочастотного коаксіального середньогабаритного кабелю марки РК 50-4-11 зі суцільною поліетиленовою ізоляцією. Бібл. 20, табл. 2.

Ключові слова: **електричні проводи і кабелі з полімерною ізоляцією, електротермічна стійкість кабельно-провідникової продукції, деструкція ізоляції, порогові амплітуди імпульсів струму для проводів і кабелів**.

Предложена инженерная методика по расчетному определению пороговых амплитуд I_{mpk} импульсов тока $i_p(t)$ различной временной формы для электрических проводов и кабелей с полиэтиленовой, поливинилхлоридной и резиновой изоляцией, широко применяемых в области импульсной энергетики, высоковольтной сильноточной техники, измерительной техники и электроники, а также в системах импульсного электропитания, контроля, управления работой и диагностики состояния функционирования электротехнических устройств различного общегражданского и военного назначения. В качестве исходного критериального положения при выборе пороговых амплитуд I_{mpk} импульсов тока $i_p(t)$ произвольных амплитудно-временных параметров для указанных проводов и кабелей была выбрана термическая стойкость их поясной изоляции, соответствующая предельно допустимым кратковременным температурам нагрева медных (алюминиевых) и изоляционных частей исследуемых кабелей (проводов) и не допускающая наступления явления деструкции в изоляции

рассматриваемой кабельно-проводниковой продукции. Приведены примеры практического использования предлагаемой методики по расчетному определению пороговых амплитуд I_{mpk} стандартных апериодических импульсов тока $i_p(t)$ временной формы 5 нс/200 нс, 10 мкс/350 мкс и 7 мс/160 мс для радиочастотного коаксиального среднегабаритного кабеля марки РК 50-4-11 со сплошной полиэтиленовой изоляцией. Библ. 20, табл. 2.
Ключевые слова: **электрические провода и кабели с полимерной изоляцией, электротермическая стойкость кабельно-проводниковой продукции, деструкция изоляции, пороговые амплитуды импульсов тока для проводов и кабелей.**

State-of-the-art and urgency of the problem. In the field of traditional electric power engineering, there is an electrical engineering approach to the engineering selection of the cross-sections S_C of electrical wires and cables with polymer insulation, used for both long-term and short-term modes of their operation [1]. This approach is based on the thermal stability of such a cable and wire product (CWP) under conditions of direct exposure to it of short-circuit (SC) current with specified amplitude-temporal parameters (ATPs). In this case, the thermal resistance of electric cables (wires) of any design is limited by the maximum permissible short-term temperature θ_{lS} of heating of their metal and insulating parts in the mode of one-, two and three-phase SC in the electrical network [1]. According to electrical data from [1], the specified temperature θ_{lS} should not exceed for those used in power circuits with alternating current of power frequency 50 Hz of non-insulated (bare) copper and aluminum buses (wires) in the SC mode of the highest level of 250 °C and 200 °C, and for cables (insulated wires) with copper (aluminum) cores, polyvinylchloride (PVC), rubber (R) and polyethylene (PET) insulation – respectively, the temperature level of 150 °C and 120 °C. In addition, it is known that in the field of industrial power engineering, the long-term permissible heating temperature θ_{ll} of conductive (insulating) parts of various electrical wires and cables is limited by the conditions of reliable operation of electrical contacts and contact connections of their circuits, as well as by the operating conditions of their insulation [1]. Here, the maximum long-term permissible heating temperature θ_{ll} for the main types of bare wires (buses) and cables (wires) with PVC, R and PET insulation, which are under current load in industrial electric power circuits, should not numerically exceed the level of 70 °C and 65 °C, respectively [1]. Taking into account the above electrical data and the fulfillment of those initial conditions that the cable (wire) before the AC current acts on it was fully electrically loaded and had temperature θ_{ll}, and upon the onset of the SC mode, it heated up to temperature θ_{lS}, in [1] to select the minimum permissible cross-section $S_{l\min}$ of the electric wire (cable), the following calculated analytical relationship is recommended:

$$S_{l\min} = B_k^{1/2} / C_k , \qquad (1)$$

where $B_k = \int_0^{t_k} i_k^2(t)dt$ is the Joule (action) integral of the SC current $i_k(t)$ with its duration t_k of flow in the CWP, $A^2 \cdot s$; C_k is the constant coefficient, $A \cdot s^{1/2}/m^2$.

We point out that the engineering method for calculating the Joule integral B_k in (1) and the numerical values of the coefficient C_k corresponding to the indicated operating conditions of wires and cables in power electric circuits for the CWP are given in [1]. The values of the cross-sections $S_{l\min}$ of the CWP found by (1) will correspond to the operating mode in the electric power circuits of wires and cables when the heating temperature of their current-carrying and insulating parts does not exceed the maximum permissible short-term temperature θ_{lS} and when the thermal resistance of the indicated CWP is ensured.

ATPs of current pulses $i_p(t)$ of nano-, micro- and millisecond time ranges generated and used in the field of high-voltage pulse technology (HPT) [2] and in other areas of modern pulsed low- and high-current power engineering, electrical engineering and electronics (for example, in equipment of pulse electrical technologies and accelerator technology [3]) to achieve various scientific and technological goals, usually do not correspond to ATPs of AC SC current in industrial power circuits. In this regard, the practical application of relationship (1) for the calculation determination of the cross-sections S_C of wires (cables) in low- and high-current electrical circuits of the indicated pulse technology is fundamentally impossible. In addition, the indicated electrical engineering approach to the choice in the industrial electric power industry of the cross-sections S_C of electric wires (cables) does not allow determining the threshold amplitudes I_{mpk} of pulse currents $i_p(t)$ with various ATPs, above which destructive processes in its polymer insulation will begin to manifest in the considered CWP. As is known, the phenomenon of destruction of such insulation, accompanied by irreversible violations of its electrical insulating properties, can be caused by an external (internal) damaging or destabilizing effect on wires and cables of various physical factors (for example, an alternating (pulsed) current flowing through their current-carrying parts, ionizing and electromagnetic radiation) [1, 4, 5]. Within the framework of the applied problem we are solving, only one destabilizing factor is considered, due to the pulse current $i_p(t)$ flowing through the electric wires and cables with various ATPs. At certain (threshold) values I_{mpk} of the amplitude I_{mp} of current pulses $i_p(t)$ of one or another temporal shape flowing through the current-carrying parts (inner core and outer shell) of the CWP, due to the intense Joule heating of these metal parts of the wires (cables), processes of thermal destruction in their belt insulation can occur [1, 6, 7]. It should be noted that at values of the amplitudes I_{mp} of pulse currents $i_p(t)$ of hundreds of kiloamperes, destructive processes in the polymer insulation of the studied CWP can also arise from the action of large electrodynamic forces on cables (wires) [2]. In practice, it is important to know such

threshold values I_{mpk} of the amplitudes I_{mp} of current pulses $i_p(t)$ of various temporal shapes, leading to a violation of the electrical insulating properties of wires (cables) used in the field of HPT, measuring technology, electronics, in systems of power supply, control, operation control and diagnostics of the state of functioning of electrical devices, and a decrease in their service life.

At present, when developing and creating in the world new polymeric insulating materials with various nano- and microstructural structures of electrical engineering and other (including medical and biological) purposes, the issues of behaviour of polymer insulation under conditions of the action of destabilizing (damaging) physical factors are given increased attention [8-11].

The goal of the paper is the development of an engineering methodology for calculating the threshold amplitudes I_{mpk} of single current pulses $i_p(t)$ of various temporal shapes for electrical wires and cables with PET, PVC and R belt insulation used in modern pulsed power engineering, electrical engineering and electronics in their low- and high-current circuits.

Problem definition. Consider insulated wires and cables with copper (aluminum) inner cores (i=1) and outer shells (i=2), with PET, PVC and R belt insulation used in electrical circuits of HPT and other low- and high-current electrical engineering (electronics) [1, 12]. We assume that single current pulses $i_p(t)$ flow in their longitudinal direction along the round solid or split copper (aluminum) cores and shells of the indicated wires and cables of electrical circuits of pulsed electrical engineering (electronics) devices, the ATPs of which can correspond to nano-, micro- and millisecond time ranges with amplitudes I_{mp}, varying in a wide range from 1 A to 1000 kA [2, 3]. We assume that wires and cables of finite length l_0 are placed in the surrounding air with temperature equal to θ_0 = 20 °C [13]. Let us use the condition of the adiabatic nature of electrothermal processes flowing at the time of action of the pulsed axial current $i_p(t)$ no more than 1000 ms in the materials of the cores (shells) of the studied CWP, in which the effect of heat transfer from the surfaces of their current-carrying parts, having current temperature $\theta_{Ci} \geq \theta_0$, and their thermal conductivity of their electrically conductive materials and insulation for Joule heating of the metal parts of the cores (shells) of wires (cables) are neglected. We believe that the thermal resistance of wires (cables) of circuits of HPT and other above-mentioned electrical engineering (electronics) devices when exposed to pulse current $i_p(t)$ is limited by their maximum permissible short-term heating temperature θ_{CiS}, which depends on the degree of decrease in the mechanical strength of the core (shell) material and thermal conditions of operation of the insulation of the CWP in the mode of its short-term heating by current pulses of nano-, micro- or millisecond duration, flowing through their current-carrying parts. As in [14], we assume that the temperature value θ_{CiS} corresponds to the known from [1] maximum permissible short-term temperature θ_{lS} of heating of wires and cables by SC currents of power frequency. Then, in accordance with the data from [1], in the electrical low- and high-current circuits of the considered electrical engineering for their insulated wires (cables) with copper and aluminum conductors (shells) and PVC (R) insulation, the value θ_{CiS} will be numerically approximately $\theta_{CiS} \approx 150$ °C , and for their CWP with the indicated cores (shells) and PET insulation – $\theta_{CiS} \approx 120$ °C . It is required to calculate in an approximate form the threshold amplitudes I_{mpk} of single current pulses $i_p(t)$ of various ATPs from nano-, micro- and millisecond time ranges flowing through electrical wires and cables with copper (aluminum) cores (shells) and PET, PVC and R belt insulation.

Electrical engineering approach to the selection of the permissible minimum cross-sections S_{Cil} of wires and cables with pulse current of various ATPs. For the permissible minimum cross-sections S_{Cil} of the current-carrying conductors (shells) of the investigated electrical wires (cables) with pulse current $i_p(t)$ of arbitrary ATPs, from the equation of their heat balance in the adiabatic mode of the CWP operation in low- and high-current circuits, the following approximate calculated relationship can be obtained [14]:

$$S_{Cil} = (J_{CiA})^{1/2} / C_l \,, \tag{2}$$

where $J_{CiA} = \int_0^{t_p} i_p^2(t)dt$ – the action integral of a single current pulse $i_p(t)$ with its duration t_p and given ATPs, $A^2 \cdot s$; $C_l = (J_{ClS} - J_{Cll})^{1/2}$ is the constant coefficient, $A \cdot s^{1/2}/m^2$; J_{ClS}, J_{Cll} are the current integrals for current-carrying conductors (shells) of electrical wires (cables) of low-current and power circuits of various electrical devices, the permissible short-term and long-term permissible heating temperatures of the CWP material which correspond to the values adopted above: $\theta_{lS} = \theta_{CiS}$ and θ_{ll}, $A^2 \cdot s/m^4$.

To find the numerical values of the current integrals J_{ClS} and J_{Cll} included in (2), the following analytical expressions can be used [14]:

$$J_{ClS} = \gamma_{0i}\beta_{0i}^{-1} \ln\left[c_{0i}\beta_{0i}(\theta_{lS} - \theta_0) + 1\right]; \tag{3}$$

$$J_{Cll} = \gamma_{0i}\beta_{0i}^{-1} \ln\left[c_{0i}\beta_{0i}(\theta_{ll} - \theta_0) + 1\right], \tag{4}$$

where γ_{0i}, c_{0i}, β_{0i} are, respectively, the specific electrical conductivity, specific volumetric heat capacity and thermal coefficient of specific electrical conductivity of the material of the core (shell) of the wire (cable) of the electric circuit before the impact on the considered CWP of the pulsed current $i_p(t)$ with arbitrary ATPs.

Table 1 shows the numerical values of the electrophysical parameters γ_{0i}, c_{0i} и β_{0i}, included in the calculation relationships (3), (4), at room temperature of the air surrounding the electrical wires and cables under consideration, equal to θ_0 = 20 °C [13].

Table 2 shows calculated according to (2) − (4) taking into account the quantitative data of Table 1 numerical values of the coefficient C_l for insulated wires and cables with copper (aluminum) cores (shells) with PVC, R and PET insulation for two cases possible in real

practice of their exploitation: the case of their preliminary current load ($J_{Cil} \neq 0$) and the case of their complete de-energizing ($J_{Cil} = 0$).

Table 1

Basic electrophysical parameters of the material of current-carrying cores (shells) of insulated wires and cables in low- and high-current circuits of modern electrical engineering (electronics) at $\theta_0 = 20$ °C [13]

Material of the core (shell) of the wire (cable)	Numerical value of the parameter		
	γ_{0i}, $10^7 \cdot (\Omega \cdot m)^{-1}$	c_{0i}, $10^6 \cdot J/(m^3 \cdot °C)$	β_{0i}, $10^{-9} \cdot m^3/J$
Copper	5,81	3,92	1,31
Alunimum	3,61	2,70	2,14

Table 2

Numerical values of the coefficient C_l for insulated wires and cables with copper (aluminum) cores (shells) in low- and high-current circuits of modern electrical engineering (electronics) with nano-, micro- and millisecond current pulses $i_p(t)$ of various ATPs

Type of insulation in a wire (cable) of a low- and high-current circuit of electrical engineering and electronics	Material of the core (shell) of the wire (cable)	Numerical value of C_l, 10^8 A·s$^{1/2}$/m^2	
		$J_{Cil}=0$	$J_{Cil}\neq 0$
PVC, R	Copper	1,506	1,160
	Aluminum	0,972	0,745
PET	Copper	1,355	0,957
	Aluminum	0,877	0,616

As for the calculated definition in (2) of the action integral J_{CiA} of a single current pulse $i_p(t)$ with one or another ATPs, we first consider the case of a change in this type of electric current in time t according to the aperiodic law of the following form [2,15]:

$$i_p(t) = k_{p1} I_{mp} \left[\exp(-\alpha_1 t) - \exp(-\alpha_2 t)\right], \qquad (5)$$

where $\alpha_1 \approx 0.76/\tau_p$, $\alpha_2 \approx 2.37/\tau_f$ are the shape coefficients of the aperiodic current pulse with the given ATPs, flowing in low- and high-current circuits of HPT, pulsed electrical engineering and electronics; $k_{p1} = [(\alpha_1/\alpha_2)^m - (\alpha_1/\alpha_2)^n]^{-1}$ is the normalizing factor; $m = \alpha_1/(\alpha_2-\alpha_1)$; $n = \alpha_2/(\alpha_2-\alpha_1)$; τ_f, τ_p are, respectively, the rise time at the level of (0.1–0.9) I_{mp} and the duration of the current pulse at the level of 0.5 I_{mp}; I_{mp} is the amplitude of the current pulse $i_p(t)$ flowing through the wire (cable).

In this electrophysical case, the expression for the action integral J_{CiA} flowing in low- and high-current circuits of the considered technique of the current pulse $i_p(t)$ takes at $t_p=3\tau_p$ according to (2), (5) the following approximate analytical form:

$$J_{CiA} \approx k_{p1}^2 I_{mp}^2 [0{,}658\tau_p - 0{,}633\tau_f]. \qquad (6)$$

Next, consider the electrophysical case when changes in time t of the pulse current $i_p(t)$ acting on the electric wires (cables) of the indicated circuits of electrical engineering (electronics) occur according to the law of a damped sinusoid [2, 13]:

$$i_p(t) = k_{p2} I_{mp1} \exp(-\delta t) \sin(\omega t), \qquad (7)$$

where $\delta=\Delta_p/T_p$ is the current damping coefficient; $\omega=2\pi/T_p$ is the circular frequency of current oscillations; T_p is the period of current oscillations; $\Delta_p=\ln(I_{mp1}/I_{mp3})$ is the logarithmic decrement of pulse current $i_p(t)$ oscillations with the first I_{mp1} and the third I_{mp3} amplitudes in electrical circuits; $k_{p2}=[\exp(-\Delta_p/2\pi \cdot \operatorname{arcctg}\Delta_p/2\pi)\sin(\operatorname{arcctg}\Delta_p/2\pi)]^{-1}$ is the normalizing factor for the damped sinusoidal current $i_p(t)$ flowing in the wire (cable).

For the temporal shape (7) of the change in the wire (cable) of the current pulse $i_p(t)$ at $t_p=3T_p$ in (2), the calculation expression for the action integral J_{CiA} of the current pulse $i_p(t)$ flowing in the investigated low- and high-current circuits of modern electrical engineering takes the following approximate analytical form:

$$J_{CiA} \approx k_{p2}^2 I_{mp1}^2 [T_p (4\Delta_p)^{-1} - \Delta_p T_p (4\Delta_p^2 + 16\pi^2)^{-1}]. \qquad (8)$$

Knowing the numerical values of I_{mp}, I_{mp1}, τ_f, τ_p, Δ_p and T_p from regulatory documents or experimental data, taking into account the calculated estimate of the values of the normalizing coefficients k_{p1} and k_{p2} for the indicated temporal shapes of changes in the pulse current $i_p(t)$ according to (2) – (8) we can in approximate form calculate (with an error of no more than 5 %), the permissible minimum cross-sections S_{Cil} of cores (shells) of electrical wires and cables used in circuits of HPT, power electrical engineering and electronics.

With regard to the applied problem being solved, the threshold values I_{mpk} of the amplitude I_{mp} of the current pulse $i_p(t)$ of the given temporal shape will correspond to the permissible short-term heating temperature $\theta_{CiS} = \theta_{lS}$ with this pulse current $i_p(t)$ of the electric wire and cable with the selected insulation. Therefore, from (2), taking into account (6), (8) and the data of Table 2, when the relation $S_{Ci} = S_{Cil}$ is fulfilled, the calculated threshold values I_{mpk} of the amplitudes I_{mp} and I_{mp1} of the axial current pulses $i_p(t)$ for the time shapes indicated according to (5), (7) flowing along the investigated insulated wires and cables in low- and high-current circuits of electrical engineering and electronics can also be determined in the considered approximation.

Calculation estimation of threshold amplitudes I_{mpk} of current pulses $i_p(t)$ of various ATPs for electrical wires and cables. In accordance with the above expressions (2), (5), (6) for the threshold value I_{mpk} of the amplitude I_{mp} of the aperiodic (unipolar) pulse of the axial current $i_p(t)$, acting on the current-carrying and insulating parts of the investigated electrical wires (cables), under the condition $S_{Ci}=S_{Cil}$, the following approximate calculated analytical relationship can be obtained:

$$I_{mpk} \approx S_{Ci} C_l k_{p1}^{-1} [0{,}658\tau_p - 0{,}633\tau_f]^{-1/2}. \qquad (9)$$

From (9) it can be seen that for given temporal parameters of the front τ_f and duration τ_p of the current pulse $i_p(t)$, known structural characteristics of wires and cables (values of their cross-sections S_{Ci}) and the selected operating mode of the CWP with the studied polymer insulation and the specified materials of its cores and shells (the known value of the coefficient C_l according to the data in Table 2), finding the desired value of the amplitude I_{mpk} will be reduced to determining,

according to (5), the numerical value of the normalizing coefficient $k_{p1}>1$.

From (2), (7), (8) under the condition $S_{Ci} = S_{Cil}$ for the threshold value I_{mpk} of the first amplitude I_{mp1} of the damped sinusoidal pulse current $i_p(t)$ in the insulated wire and cable, the following approximate calculated analytical expression follows:

$$I_{mpk} \approx S_{Ci} C_l k_{p2}^{-1} [T_p (4\Delta_p)^{-1} - \Delta_p T_p (4\Delta_p^2 + 16\pi^2)^{-1}]^{-1/2}. \quad (10)$$

Similarly to (9), using (10) to find the calculated value I_{mpk} for a particular wire (cable) with known characteristics S_{Ci} and C_l (see Table 2) at given temporal parameters Δ_p и T_p for the discharge pulse current $i_p(t)$ flowing through the CWP will actually be reduced to the calculation according to (7) of the numerical value of the normalizing coefficient $k_{p2}\geq 1$.

According to (9), (10), the threshold values I_{mpk} of the amplitudes I_{mp} of aperiodic and damped sinusoidal current pulses $i_p(t)$ are directly proportional to the cross-sections S_{Ci} of the metal cores (shells) of the electrical wires and cables under study. In addition, the sought values of I_{mpk} are actually inversely proportional to the temporal parameters $\tau_p^{1/2}$ и $T_p^{1/2}$ for current pulses $_p(t)$flowing through the CWP.

Note that the calculated relations (9), (10) for determining the threshold values I_{mpk} of the amplitudes I_{mp} of the axial current pulses $i_p(t)$, varying in time t according to (5), (7) according to the aperiodic dependence and the law of the exponentially decaying sinusoid, cover a wide nomenclature of temporary shapes and ATPs of used in electrophysical practice single current pulses $i_p(t)$ flowing through current-carrying parts of wires and cables with PVC, R and PET belt insulation in modern pulsed power engineering, electrical engineering and electronics.

In low- and high-current circuits of the considered power engineering, electrical engineering and electronics with the temporal shapes of current pulses $i_p(t)$ flowing through their CWP used according to (5), (7) at $I_{mp}>I_{mpk}$, thermal overheating of the current-carrying parts of wires and cables will lead to destruction of their insulation, which reduces the working life of the CWP used in them.

Calculation estimation of the heating temperature θ_{Ci} of electrical wires and cables by current pulses $i_p(t)$ of various ATPs. For the purpose of computational verification of the formulas (9), (10) for choosing the threshold amplitudes I_{mpk} of the pulse current in the considered CWP, let us estimate the temperature θ_{Ci} of the Joule heating of the current-carrying parts of cables (wires) through which single current pulses $i_p(t)$ with specified ATPs flow. For this, we use the well-known nonlinear dependence of the electrical conductivity γ_{0i} of the material of the core (shell) of the wire (cable) on its current temperature θ_{Ci} [13]:

$$\gamma_{0i} \approx \gamma_{20i} \left[1 + c_{0i}\beta_{0i}(\theta_{Ci} - \theta_0)\right]^{-1}, \quad (11)$$

where γ_{20i} is the specific electrical conductivity γ_{0i} of the conductive material of the current-carrying parts of the CWP at the temperature of the surrounding air $\theta_{Ci}=\theta_0=20$ °C (for copper and aluminum these values of γ_{20i} are indicated in Table 1).

For used in CWP of pulsed power engineering, electrical engineering and electronics basic metals, (11) describes the temperature changes in their parameter γ_{0i} with an error of no more than ±5 % [13].

Taking into account (11) and data from [13], the solution of the inhomogeneous differential equation of thermal conductivity applied to the metal parts of the investigated cables (wires) of the adopted length l_0 with pulse current $i_p(t)$ of various ATPs for the current temperature θ_{Ci} of their Joule heating by the specified current under the initial condition $[\theta_{Ci}|_{(t=0)} - \theta_0] = 0$ can be written in the following approximate form:

$$\theta_{Ci} \approx \theta_0 + (c_{0i}\beta_{0i})^{-1} [\exp(J_{CiA}^2 \gamma_{20i}^{-1} \beta_{0i} / S_{Ci}^2) - 1]. \quad (12)$$

It follows from (12) that the current temperature θ_{Ci} of heating by pulsed current $i_p(t)$ of various ATPs of current-carrying cores (shells) of the considered CWP is inversely proportional to the specific volumetric heat capacity c_{0i} (heat capacity per unit volume of metal) of their conductive materials, which for most metals in the solid phase varies depending on their temperature within ±10 % of its average numerical value [13]. We point out that for the thermophysical parameter c_{0i}, an equality of the form [13] is fulfilled: $c_{0i}=c_{\rho i}\cdot\rho_i$, where $c_{\rho i}$ is the heat capacity per unit mass of the homogeneous conductive material of the CWP (J/kg·°C) with its density ρ_i (kg/m^3). Therefore, in the investigated electrophysical case, we can say that the overall parameters of the CWP (except for the cross-section S_{Ci} of its cores and shells) at given ATPs of current pulses i $i_p(t)$ flowing through its metal parts do not affect the heating of cables (wires). This thermal process is attended, according to (12), by mainly the specific thermophysical parameters of the CWP (γ_{0i}, c_{0i} and β_{0i}) and the ATPs of the pulsed current $i_p(t)$ [13]. For short (with extremely small values of τ_p and T_p) current pulses $i_p(t)$, the heating zone of the CWP will be localized in very thin layers of its metal cores and shells. Taking into account the accepted assumptions and (12), we can conclude that in the considered adiabatic approximation, the length l_0 of the cable (wire) and, accordingly, the total mass of the metal parts of the CWP at $t\leq 3\tau_p$ or $t\leq 3T_p$ does not have a noticeable effect on the pulse heating temperature θ_{Ci} of these parts of the CWP. This influence on the temperature level θ_{Ci} will increase after the passage of the considered current pulses $i_p(t)$ through the current-carrying parts of the CWP, when, due to the thermal conductivity of their metal, the temperature will begin to equalize along the thickness of these parts.

In the case when the relation $S_{Ci} = S_{Cil}$ is fulfilled for the current-carrying metal parts of the cables and wires under consideration, taking into account (2), expression (12) is simplified and takes the following form:

$$\theta_{Ci} \approx \theta_0 + (c_{0i}\beta_{0i})^{-1} [\exp(\gamma_{20i}^{-1} \beta_{0i} C_l^2) - 1], \quad (13)$$

where C_l is the constant coefficient, the numerical values of which for the considered polymer insulation of cables (wires) and the specified operating modes of their electrical circuits are given in Table 2.

Relation (13) can be just used in the calculated verification of the obtained expressions (9), (10) to find the numerical values of the threshold amplitudes I_{mpk} of the pulse current $i_p(t)$ in the considered CWP. According to the conditions we have adopted, at $S_{Ci} = S_{Cil}$, the calculated according to (13) temperature θ_{Ci} of heating of the current-carrying parts of the studied CWP should not exceed the accepted normalized permissible short-term temperature θ_{CiS} for it.

Examples of calculating the threshold amplitudes I_{mpk} of current pulses $i_p(t)$ of nano-, micro- and millisecond temporal ranges. As the investigated CWP, we choose a short radiofrequency coaxial medium-sized cable with solid PET insulation, brand RC 50-4-11 [12], having, at $l_0 \leq 10$ m, a round solid copper core with diameter of 1.37 mm ($S_{C1} \approx 1.474$ mm^2) and tinned braided copper shell (braid with twisting density of at least 95 %) with inner diameter of 4.6 mm and wall thickness of 0.15 mm ($S_{C2} \approx 2{,}059$ мм^2). We assume that this cable is placed in an air atmosphere at room temperature $\theta_0 = 20$ °C with the fulfillment of the condition for the current integral $J_{Cil} = 0$ in its electrical circuit (without preliminary current load of the cable at $\theta_{il} = \theta_0$). From the given design data, it can be seen that the copper core of the selected RF cable brand RC 50-4-11 with cross-section $S_{C1} \approx 1.474$ mm^2 in comparison with its reverse external current conductor (copper braid with cross-section $S_{C2} \approx 2.059$ mm^2) will be less resistant to the electrothermal action of a current pulse $i_p(t)$ longitudinally flowing through them in opposite directions with specified ATPs. Let a single current pulse $i_p(t)$ flowing through the current-carrying parts of the adopted coaxial cable has an aperiodic temporal shape. Therefore, the specified core of the cable of the RC 50-4-11 brand can be an internal local hotbed of overheating of the current-carrying parts of this cable. In this regard, the continuous belt PET insulation adjacent to the copper core of the RC 50-4-11 radiofrequency cable may experience the effect of increased levels of the temperature field caused by the Joule heating of this copper core by the adopted current pulse $i_p(t)$ flowing through it. It is the copper core and the adjacent cylindrical zone of PET insulation of the RF cable of the adopted in applied calculations values I_{mpk} that will be the weak «links» in a possible chain of destructive processes in the cable under consideration. Taking into account the above, it can be concluded that the calculation estimation of the threshold values I_{mpk} of the amplitude I_{mp} of the used current pulse $i_p(t)$ of a given time shape for a radiofrequency cable of the brand RC 50-4-11 should be tied to the electrothermal state of a single-wire round copper core ($S_{C1} \approx 1.474$ mm^2) of this cable experiencing the thermal effect of an aperiodic current pulse $i_p(t)$.

1. First, we use a standard nanosecond current pulse of a temporal shape $\tau_f/\tau_p = 5$ ns/200 ns, which was used in a number of countries when simulating in high-current discharge electric circuits of HPT with multi-wire air systems of field formation and, accordingly, in their working air volumes with those tested for electromagnetic compatibility (durability) technical objects of various dimensions of a powerful electromagnetic pulse of a high-altitude nuclear explosion [4, 16]. From (5) we find that for this calculation case, the shape factors α_1 and α_2 of the nanosecond current pulse $i_p(t)$ take the following numerical values: $\alpha_1 \approx 3.8 \cdot 10^6$ s^{-1}; $\alpha_2 \approx 4.7 \cdot 10^8$ s^{-1}. In this case, for a given temporal shape of a unipolar current pulse $i_p(t)$, the normalizing factor k_{p1} according to (5) turns out to be approximately equal to $k_{p1} \approx 1.049$. Then from (9) at $k_{p1} \approx 1.049$, $C_l = 1.355 \cdot 10^8$ A·s$^{1/2}$/m^2 (see the corresponding data in Table 2) and $S_{Ci} = S_{C1} = 1.474$ mm^2 (cross-section of the copper cable core) for the threshold numerical value I_{mpk} the amplitude I_{mp} of the considered aperiodic current pulse $i_p(t)$ of the temporal shape $\tau_f/\tau_p = 5$ ns/200 ns in relation to the RF coaxial cable of the brand RC 50-4-11, we find that $I_{mpk} \approx 531.2$ kA.

2. Next, consider the standard microsecond aperiodic current pulse $i_p(t)$ of the time shape $\tau_f/\tau_p = 10$ μs/350 μs, which is now used in accordance with the requirements of the current International Standard IEC 62305-1-2010 [17] when testing power electrical equipment for resistance to the direct action of powerful short lightning electric discharges on it [18]. From (9) at $k_{p1} \approx 1.054$ ($\alpha_1 \approx 2.17 \cdot 10^3$ s^{-1}; $\alpha_2 \approx 2.37 \cdot 10^5$ s^{-1}), $C_l = 1.355 \cdot 10^8$ A·s$^{1/2}$/m^2 and section of a solid copper core $S_{Ci} = S_{C1} = 1.474$ mm^2 of the RC 50-4-11 RF cable under study for the threshold numerical value I_{mpk} of the amplitude I_{mp} of the considered aperiodic pulse of the axial current $i_p(t)$ of the time shape $\tau_f/\tau_p = 10$ μs/350 μs in the adopted cable we find that $I_{mpk} \approx 12.66$ kA.

3. At the end of the examples of applied calculations of threshold amplitudes I_{mpk} for the CWP, we use the standard millisecond aperiodic current pulse $i_p(t)$ of the temporal shape $\tau_f/\tau_p = 7$ ms/160 ms, which is now used in accordance with the requirements of the current US regulatory document SAE ARP 5412: 2013 [19] during full-scale electromagnetic tests of the main units and systems of aviation equipment for lightning resistance to direct exposure to them by the long-term component of the artificial lightning current [20]. For this current pulse $i_p(t)$in accordance with (9) at $k_{p1} \approx 1.078$ ($\alpha_1 \approx 4.75$ s^{-1}; $\alpha_2 \approx 3.38 \cdot 10^2$ s^{-1}), $C_l = 1.355 \cdot 10^8$ A·s$^{1/2}$/m^2 and a given cross-section of a copper core $S_{Ci} = S_{C1} = 1.474$ mm^2 of a radiofrequency coaxial cable of the RC 50-4-11 brand, it follows that the threshold numerical value I_{mpk} of the amplitude I_{mp} of the specified axial current pulse $i_p(t)$ of the temporal shape $\tau_f/\tau_p = 7$ ms/160 ms for it will be equal to about $I_{mpk} \approx 1.84$ kA.

One of the indicators of the reliability of the electrical engineering approach used by us and the approximate calculated relationship (9) obtained on its basis, used in the above examples of determining the threshold values I_{mpk} of the amplitudes I_{mp} of unipolar current pulses $i_p(t)$ of nano-, micro- and millisecond duration for a radiofrequency coaxial cable brand RC 50-4-11, is that the performance according to (13) in relation to these practical cases of finding the numerical values I_{mpk} of the estimated calculation of the heating temperature θ_{Ci} (at $\theta_0 = 20$ °C and $J_{Cil} = 0$) of the round solid copper core of the specified cable leads to a result

equal to $\theta_{Ci} \approx 119.9$ °C. It can be seen that the calculated temperature level θ_{Ci} of Joule heating of the CWP in the cases under study does not exceed the permissible short-term temperature $\theta_{CiS} \approx 120$ °C, which is typical for electrical cables with PET insulation.

Conclusions.

1. An engineering technique has been developed for the approximate calculation of the threshold amplitudes I_{mpk} of single pulses of axial current $i_p(t)$ of various temporal shapes for electrical wires and cables with copper (aluminum) current-carrying parts and PET, PVC and R belt insulation used in low- and high-current pulse circuits of power engineering, electrical engineering and electronics. This technique is based on the electrothermal resistance of the polymer insulation of the considered CWP, which corresponds to the permissible short-term heating temperatures of current-carrying and insulating parts of its wires and cables and does not allow the occurrence of the phenomenon of thermal destruction in the belt insulation of the CWP.

2. Calculation analytical relationships (9), (10) are obtained for finding the threshold numerical values I_{mpk} of the amplitudes I_{mp} of the current pulses $i_p(t)$, which vary in time t according to the aperiodic dependence and according to the law of the exponentially decaying sinusoid, in the studied CWP. It is shown that at $I_{mp}>I_{mpk}$, due to thermal overheating of the current-carrying parts of the wires and cables under consideration, destruction of their belt insulation will occur, leading to a decrease in the service life of the CWP.

3. Examples of practical application of the proposed engineering methodology for the calculation definition for a radiofrequency coaxial medium-sized cable of the RC 50-4-11 brand with solid PET belt insulation of threshold amplitudes I_{mpk} of standard aperiodic current pulses $i_p(t)$ from nano-, micro- and millisecond temporal ranges of the shape τ_f/τ_p=5 ns/200 ns, τ_f/τ_p=10 μs/350 μs, and τ_f/τ_p=7 ms/160 ms are presented. It was found that with a corresponding increase in the parameter $\tau_p>>\tau_f$ for the indicated unipolar single pulses of current $i_p(t)$ flowing through a round solid copper conductor and a hollow split tinned copper braid of this cable, there is a significant decrease in their threshold amplitudes I_{mpk} (from 531.2 kA for a nanosecond current pulse of 5 ns/200 ns to 1.84 kA for millisecond current pulse of 7 ms/160 ms).

Acknowledgment. The work was supported by the Ministry of Education and Science of Ukraine (Project DB No. 0121U109546).

Conflict of interest. The authors of the paper declare no conflict of interest.

REFERENCES

1. Orlov I.N. *Elektrotehnicheskij spravochnik. Proizvodstvo i raspredelenie elektricheskoj energii. Tom 3, Kn. 1* [Electrical engineering handbook. Production and distribution of electric energy. Vol. 3, Book 1. Ed. I.N. Orlov]. Moscow, Energoatomizdat Publ., 1988. 880 p. (Rus).

2. Dashuk P.N., Zayents S.L., Komel'kov V.S., Kuchinskyi G.S., Nikolayevskaya N.N., Shkuropat P.I., Shneerson G.A. *Tehnika bol'shih impul'snyh tokov i magnitnyh polej* [The technique of large pulsed currents and magnetic fields]. Moscow, Atomizdat Publ., 1970. 472 p. (Rus).

3. Mesiats G.A. *Impul'snaia energetika i elektronika* [Pulsed power and electronics]. Moscow, Nauka Publ., 2004. 704 p. (Rus).

4. Ricketts L.U., Bridges J.E., Mayletta J. *Elektromahnitnij impul's i metody zashchity* [Electromagnetic pulse and methods of protection]. Moscow, Atomizdat Publ., 1979. 328 p. (Rus).

5. Myrova L.O., Chepizhenko A.Z. *Obespechenie stoikosti apparatury svyazi k ioniziruyushchim i elektromagnitnym izlucheniyam* [Providing of resistibility of apparatus of connection to the ionizing and electromagnetic radiations]. Moscow, Radio and Connection Publ., 1988. 296 p. (Rus).

6. Shidlovskyi A.K., Shcherba A.A., Zolotaryov V.M., Podoltsev A.D., Kucheryavaya I.N. *Kabeli s polimernoy izolyatsiey na sverhvysokie napryazheniya* [Cables with a polymeric isolation on over-voltage]. Kyiv, Institute of Electrodynamics of NAS of Ukraine Publ., 2013. 550 p. (Rus).

7. Pugach V.N., Polyakov D.A., Nikitin K.I., Tereshchenko N.A., Komarov I.V. Research of temperature destruction effect on cables insulation operation life. *Omsk Scientific Bulletin*, 2019, no. 6 (168), pp. 70-74. (Rus). doi: https://doi.org/10.25206/1813-8225-2019-168-70-74.

8. Miller-Chou B.A., Koenig J.L. A review of polymer dissolution. *Progress in Polymer Science*, 2003, vol. 28, no. 8, pp. 1223-1270. doi: https://doi.org/10.1016/s0079-6700(03)00045-5.

9. Brzeziński M., Wedepohl S., Kost B., Calderón M. Nanoparticles from supramolecular polylactides overcome drug resistance of cancer cells. *European Polymer Journal*, 2018, vol. 109, pp. 117-123. doi: https://doi.org/10.1016/j.eurpolymj.2018.08.060.

10. Schulte R., Ostwald R., Menzel A. Gradient-Enhanced Modelling of Damage for Rate-Dependent Material Behaviour – A Parameter Identification Framework. *Materials*, 2020, vol. 13, no. 14, p. 3156. doi: https://doi.org/10.3390/ma13143156.

11. Spirescu V.A., Chircov C., Grumezescu A.M., Andronescu E. Polymeric Nanoparticles for Antimicrobial Therapies: An up-to-date Overview. *Polymers*, 2021, vol. 13, no. 5, p. 724. doi: https://doi.org/10.3390/polym13050724.

12. Belorussov N.I., Saakjan A.E., Jakovleva A.I. *Elektricheskie kabeli, provoda i shnury. Spravochnik* [Electrical cables, wires and cords. Directory]. Moscow, Energoatomizdat Publ., 1988. 536 p. (Rus).

13. Knopfel' G. *Sverkhsil'nye impul'snye magnitnye polia* [Ultra strong pulsed magnetic fields]. Moscow, Mir Publ., 1972. 391 p. (Rus).

14. Baranov M.I., Rudakov S.V. Electrothermal action of the pulse of the current of a short artificial-lightning stroke on test specimens of wires and cables of electric power objects. *Journal of Engineering Physics and Thermophysics*, 2018, vol. 91, no. 2, pp. 544-555. doi: https://doi.org/10.1007/s10891-018-1775-2.

15. Baranov M.I., Kniaziev V.V., Rudakov S.V. Calculation and experimental estimation of results of electro-thermal action of rationed by the international standard IEC 62305-1-2010 impulse current of short blow of artificial lightning on the thin-walled coverage from stainless steel. *Electrical Engineering & Electromechanics*, 2017, no. 1, pp. 31-38. doi: https://doi.org/10.20998/2074-272X.2017.1.06.

16. Gurevich V.I. *Elektromagnitnyi impul's vysotnogo iadernogo vzryva i zashchita elektrooborudovaniia ot nego: monografiia* [Electromagnetic impulse of high-altitude nuclear explosion and protection of electrical equipment from it: monograph]. Moscow, Infra-Engineering Publ., 2019. 516 p. (Rus).

17. *IEC 62305-1: 2010. Protection against lightning. Part 1: General principles*. Geneva, IEC Publ., 2010. Available at:

https://cs.spz-bc.com.ua/-/Du44pi68kxwVNlVLm0wh0g/sv/document/4b/f8/7c/437461/255/IEC-62305-1_v1_LQ.pdf?1559637095 (accessed 25 May 2021).
18. Baranov M.I., Koliushko G.M., Kravchenko V.I., Rudakov S.V. A generator aperiodic current pulses of artificial lightning with a rationed temporal form of 10/350 μs with an amplitude of ±(100-200) kA. *Instruments and Experimental Techniques*, 2015, vol. 58, no. 6, pp. 745-750. doi: https://doi.org/10.1134/s0020441215060032.
19. *SAE ARP 5412: 2013. Aircraft Lightning Environment and Ralated Test Waveforms*. SAE Aerospace. USA, 2013, pp. 1-56. Available at: https://www.sae.org/standards/content/arp5412b (accessed 25 May 2021).
20. Baranov M.I., Buriakovskyi S.G., Rudakov S.V. The tooling in Ukraine of model tests of objects of energy, aviation and space-rocket engineering on resistibility to action of pulsed current of artificial lightning. *Electrical Engineering & Electromechanics*, 2018, no. 4, pp. 45-53. doi: https://doi.org/10.20998/2074-272X.2018.4.08.

Received 12.10.2021
Accepted 15.11.2021
Published 03.12.2021

M.I. Baranov[1], *Doctor of Technical Science, Professor,*
S.G. Buriakovskyi [1], *Doctor of Technical Science, Professor,*
V.V. Kniaziev[1], *Candidate of Technical Science, Leader Research Scientist,*
[1] Research and Design Institute «Molniya»
of National Technical University
«Kharkiv Polytechnic Institute»,
47, Shevchenko Str., Kharkiv, 61013, Ukraine,
e-mail: baranovmi@kpi.kharkov.ua (Corresponding Author),
sergbyr@i.ua, knyaz2@i.ua

How to cite this article:
Baranov M.I., Buriakovskyi S.G., Kniaziev V.V. Destruction of polymer insulation and threshold amplitudes of current pulses of different temporal shapes for electric wires and cables in the low- and high-current circuits of pulse power engineering, electrical engineering and electronic devices. *Electrical Engineering & Electromechanics*, 2021, no. 6, pp. 31-38. doi: https://doi.org/10.20998/2074-272X.2021.6.05.

UDC 621.315.6 https://doi.org/10.20998/2074-272X.2021.6.06

V.M. Kyrylenko, K.V. Kyrylenko, M.O. Budko, P.L. Denysiuk

Reasoning of additional diagnostic parameters for electric insulation diagnostics by absorption methods

*The **aim** of this work is to analyze the inadequacies of the diagnostic parameters, in particular the absorption and polarization coefficients, which are manifested in their integral character and dependence on the ratio of values of several elements of the equivalent scheme of insulation replacement. This article contains the results of theoretical investigation of the extreme nature of the absorption diagnostic parameters, which leads to unambiguity of the diagnostics procedure. The ways of partial adjustment of this unambiguity have been proposed. **Methodology.** To determine the extremality of the absorption coefficients depending on the absorption time, absorption capacity and resistance, as well as the leakage resistance, the usual method of investigating the functions was used, detailed calculations have been obtained by using MATLAB software. **Results**. Has been shown that the ambiguity* of diagnostic results *is caused by the contradiction of the integral character of the diagnostic parameters and the local character of the isolation* failures*,* in particular breakdown*, by ambiguous dependence of the diagnostic parameters on the values of the elements of the insulation replacement scheme and the extremal nature of the diagnostic parameters. Based on the general expression describing all currently used absorption coefficients, it is shown that they all have an extremum, the value of which depends on the parameters of the insulation substitution scheme and the time interval between the measurements of the absorption current. The dependence of the extreme value of the absorption and polarization coefficients on the parameters of the insulation substitution scheme has been established. Has been shown that to eliminate the ambiguity caused by the extremity of the absorption coefficients, it is necessary to introduce additional diagnostic parameters, such as the ratio of leakage resistance to absorption resistance, as well as the critical value of the absorption time constant. **Originality.** The detailed analysis of the reasons of ambiguity of electric insulation technical diagnostics by absorption methods has been carried out. A method for eliminating the ambiguity caused by the extremity of the absorption coefficients has been proposed. **Practical significance.** To eliminate the ambiguity caused by the extremity of the absorption coefficients, additional diagnostic parameters are proposed – the ratio of leakage resistance to the absorption resistance and critical values of the absorption time constant. The applying of these parameters with the absorption coefficients will more adequately assess the technical condition of insulation.* References 15, tables 2, figures 4.

Key words: **non-destructive insulation diagnostics, absorption methods of insulation diagnostics, diagnostic parameters of insulation, dielectric absorption ratio, absorption index, polarization index.**

В статті представлено результати аналізу екстремального характеру і зумовленої ним неоднозначності залежності абсорбційних коефіцієнтів від сталої часу абсорбції, а також залежності їх значень від відношення наскрізного опору ізоляції до її абсорбційного опору. Розраховано максимальні значення коефіцієнтів абсорбції і поляризації, а також сталої часу абсорбції, що відповідає їм, для різних значень відношення вказаних вище опорів. Обґрунтована можливість використання відношення наскрізного і абсорбційного опорів та абсорбційної сталої часу в якості додаткових діагностичних параметрів для усунення неоднозначності, пов'язаної з екстремальністю коефіцієнтів абсорбції і поляризації. Бібл. 15, табл. 2, рис. 4.

Ключові слова: **неруйнівні методи діагностування електричної ізоляції, абсорбційні методи діагностування ізоляції, діагностичні параметри ізоляції, ємнісний і омічний коефіцієнти абсорбції, коефіцієнти абсорбції і поляризації.**

В статье представлены результаты анализа экстремального характера и обусловленной им неоднозначности зависимости абсорбционных коэффициентов от постоянной времени абсорбции и зависимости их значений от отношения сквозного сопротивления изоляции к ее абсорбционному сопротивлению. Рассчитаны максимальные значения коэффициентов абсорбции и поляризации, а также постоянных времени абсорбции, которые соответствуют им, для различных значений отношения указанных выше сопротивлений. Обоснована возможность использования отношения сквозного и абсорбционного сопротивлений и абсорбционной постоянной времени в качестве дополнительных диагностических параметров для устранения неоднозначности, связанной с наличием максимумов коэффициентов абсорбции и поляризации. Библ. 15, табл. 2, рис. 4.

Ключевые слова: **неразрушающие методы диагностирования электрической изоляции, абсорбционные методы диагностирования изоляции, диагностические параметры изоляции, емкостной и омический коэффициенты абсорбции, коэффициенты абсорбции и поляризации.**

Introduction. To ensure efficient and trouble-free operation of electrical engineering and electrical power equipment, periodic or continuous monitoring of its technical condition is carried out using destructive and non-destructive electrical methods of control and testing. Non-destructive methods include the use of electrophysical and dielectric characteristics, their dependencies on the intensity of the electric field and external factors or their relative values at different values of the parameters of the active factors.

To assess the technical condition of electrical insulation in practice they often use the results of its non-destructive diagnosis by the values of electrical resistance of insulation and the characteristics of the absorption current flowing through the insulation when connected to DC voltage. These methods are based on the generalized equivalent dielectric circuit (Fig. 1).

The advantages of the generalized equivalent circuit of inhomogeneous dielectric include transparency of interpretation of the physical content of its elements, their direct connection with physical processes in insulation of inhomogeneous dielectrics which determine its performance properties and durability.

The elements of the generalized equivalent dielectric circuit include:

- geometric capacitance C_g which reflects the capacitance associated with the rapid processes of electronic and ionic polarization;
- through resistance R_n, i.e. the steady value of the resistance of the dielectric to the flow of direct current;
- absorption capacitance C_a which is responsible for the slow processes of migratory polarization due to the accumulation of free charges within the dielectric regions with different electrophysical properties or in the electrode regions;
- absorption resistance R_a which is introduced to correctly reflect the inertial properties of migratory polarization.

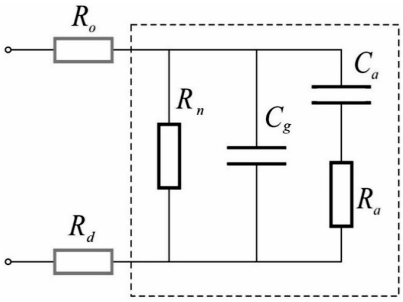

Fig. 1. Generalized equivalent insulation circuit and elements of the measurement circuit

In addition, Fig. 1 shows the circuit elements:

- R_o – limiting resistance which is introduced into the measuring circuit to form the exponential charge current of the geometric capacitance;
- R_d – resistance of the sensor to measure the voltage that corresponds to the absorption current through the dielectric.

In order for them not to affect the diagnostic results, the resistance value of these resistors must be significantly less than the resistance value of the dielectric leakage.

In the general case, the inhomogeneous dielectric's circuit may contain several $C_a - R_a$ circuits corresponding to the absorption processes with time constants of different types of migratory polarization. Note that the relaxation polarization when using the absorption and polarization coefficients is not taken into account because the moments of time at which the absorption current is measured to calculate the values of these parameters significantly exceed the time constants of relaxation processes.

Review of the state of absorption methods for diagnosing electrical insulation. Absorption diagnostic methods are recommended as normative for diagnosing insulation of transformers, synchronous generators, compensators, collector exciters and AC motors [1]. Modern scientific research of absorption methods and their use relate to diagnosing the insulation condition of rotating electric machines [2, 3], low-voltage and high-voltage cables [4-7], power transformers [8-10].

In technical diagnostics, two types of absorption coefficients are used – ohmic and capacitive coefficients, as well as coefficients determined by the ratio of absorption current values at different points in time, the method of restored voltage and its modern varieties, and nonlinearity of absorption and restored voltage characteristics.

The ohmic absorption coefficient is equal to the ratio of the values of the absorption current or effective insulation resistance, measured after 15 and 60 s for currents or after 60 and 15 s for resistances:

$$k_a = \frac{i_{15}}{i_{60}} = \frac{R_{60}}{R_{15}} = \frac{1+\frac{R_n}{R_a}\exp(-\frac{60}{\tau_a})}{1+\frac{R_n}{R_a}\exp(-\frac{15}{\tau_a})}. \quad (1)$$

In addition to the ohmic absorption coefficient, they now use the polarization coefficient k_p with the values of the absorption current reference time of 60 and 600 s, the dielectric absorption ratio R_{30}/R_{15} and the polarization index R_{60}/R_{30}, the dielectric discharge coefficient, and the insulation state coefficient determined by the two, taken at the initial section of the absorption current at 0.06 and 0.1 s, the charge of the geometric capacitance and the time interval between samples:

$$k_{ci} = \frac{i_{0,06} - i_{0,1}}{\Delta t \cdot q_g} = \frac{i_{0,06} - i_{0,1}}{0{,}04 q_g}.$$

The capacitive absorption coefficient is determined by the ratio of the maximum value of the restored voltage $U_{r\max}$ to the charging voltage U_0:

$$k_c = \frac{U_{r\max}}{U_0} = \frac{C_a}{C_a + C_g}. \quad (2)$$

Restored voltage occurs on the insulation, if after a full charge it is disconnected from the voltage source, short-circuited for a short period of time to discharge the geometric capacity, and then allow the absorption tank to charge geometric one, the voltage on which will increase from zero to maximum, and then fall to zero due to the discharge due to the through resistance.

A variation of the capacitive absorption coefficient is the dispersion coefficient, which is determined by charging the insulation capacitance with a short rectangular pulse of duration τ_1 of voltage U_0 and measuring the voltage U_d on it after disconnection from the voltage source after a time interval $\tau_2 >> \tau_1$ when the introduced charge is redistributed between the geometric and absorption capacitances:

$$D = \frac{U_0}{U_0 - U_d} = \frac{C_g}{C_a} = \frac{1-k_c}{k_c}.$$

The use of capacitive and ohmic absorption coefficients to assess the state of electrical insulation has significant disadvantages: first, they are integral characteristics of insulation; secondly, they are determined by the ratio of the values of several elements of the equivalent dielectric circuit; third, they do not give a complete picture of the processes of insulation degradation. Let's consider these issues in more detail.

As follows from (1), the values of the absorption coefficient depend on the ratio of through resistance and absorption resistance and on the absorption constant time which are integral indicators because they are averaged over the entire volume of insulation. Therefore, this

criterion can be used only to assess the general condition of the insulation, such as more or less uniform moisture or caused by its aging general deterioration of electrophysical characteristics and an increase in the probability of failure.

In addition, all coefficients determined by the ratio of the two values of the absorption current, as will be shown below, are extreme values and their criteria can be inherent in both wet and aged insulation and homogeneous insulation, in which absorption processes are very weak.

The capacitive coefficient according to (2) is characterized by the ratio of geometric and absorption capacitances, which are also integral characteristics of insulation, partially characterizes the heterogeneity of insulation and its growth during aging. However, it in general does not provide information on the nature of the resistivity distribution and resistive components of the equivalent circuit, which are responsible for thermal aging and thermal breakdown of the dielectric, and also gives an idea only of the intensity of volume migration or near-electrode polarizations without specifying its characteristics, such as time constant of migratory polarization. In addition, the value $U_{r\max}/U_0$ will depend on the ratio R_n/R_a because this ratio determines the voltage that can occur on the parallel through resistance R_n the geometric capacity C_g, and therefore the capacitive absorption coefficient will be only the limit value for the ratio $U_{r\max}/U_0$.

Further improvements of absorption methods based on restored voltage are actively considered in the literature for the purpose of more adequate technical diagnostics of electrical insulation [11-13]. When using the method of restored voltage, as diagnostic parameters of insulation it is proposed to use the ratio of the maximum value of the restored voltage to the charging one, the initial rate of increase of the restored voltage, the time of reaching the maximum value of the restored voltage, the maximum value of the restored voltage, the coefficients of nonlinearity of the restored voltage, the time constant of the self-discharge, but in this article the method of recharged voltage will not be considered.

Taken into account the prevalence of absorption methods, most modern domestic and foreign megohmmeters allow not only to measure the insulation resistance, but also automatically calculate the absorption coefficient and record data to calculate the polarization coefficient. Even more detailed processing of the absorption curve, including the method of recharge voltage, is offered in specialized diagnostic systems.

However, it should be noted that with various proposals for the selection of diagnostic procedures and parameters and fairly intensive publication of the results of the use of absorption methods for diagnostic purposes in domestic and foreign literature, quite serious problems remain the choice of good condition when using appropriate diagnostic parameters and interpretation of processes occurring in isolation, based on changes in specific diagnostic parameters over time, and at the same time the results obtained to assess the state of electrical insulation.

The main factor that significantly reduces the prognostic potential of absorption methods is the irreparable contradiction between the integral nature of diagnostic parameters and the local nature of the breakdown, as a catastrophic process of insulation failure. Absorption methods can give an idea of the general state of insulation due to thermal aging and other processes that lead to the deterioration of the general state of insulation, but they are not effective for predicting breakdown. The possibility of breakdown is determined by the characteristics of the insulation in a very limited volume, which is hundreds of thousands of parts of the total volume, and therefore the value of the integral characteristics is not affected.

Promising in the improvement of absorption methods are works in which methods of determining the individual values of the parameters of the equivalent insulation substitution circuit are considered [14], but they also do not solve this problem. In addition, the diagnostic parameters are transient in time, which leads to additional errors in their use to determine the technical condition [15].

In addition, even the patterns of change of diagnostic parameters depending on the values of the parameters of the equivalent insulation circuit have not been systematically studied, although this dependence leads to ambiguity of technical condition criteria and reduces their prognostic ability. As an example, we can cite the extremity of the absorption and polarization coefficients, which, as shown below, will be close to unity also in highly humid and almost homogeneous insulation. Therefore, there is a need to eliminate this ambiguity.

The goal of this article is to study the extremity of ohmic absorption coefficients and to substantiate additional diagnostic parameters to eliminate the ambiguity of absorption and polarization coefficients associated with the presence of a maximum in the dependencies of these coefficients on the absorption time constant.

Analysis of the extremity of the absorption coefficients. We will perform this analysis using a generalized equivalent circuit of an inhomogeneous dielectric (see Fig. 1), which is the basis of absorption methods for diagnosing electrical insulation.

According to the definition, ohmic absorption coefficients, i.e. absorption coefficients, polarization, dielectric absorption ratio and polarization index, are equal to the ratio of the insulation resistances of the product, measured after time equal to t_1 and t_2, after applying a constant voltage [1]:

$$k_a = \frac{R_{t_1}}{R_{t_2}} = \frac{1+\frac{R_n}{R_a}\exp\left(-\frac{t_1}{\tau_a}\right)}{1+\frac{R_n}{R_a}\exp\left(-\frac{t_2}{\tau_a}\right)}, \qquad (3)$$

where $\tau_a = C_a \cdot R_a$ is the absorption time constant.

We show that all absorption coefficients determined by the ratio of the two values of the absorption current are extreme values and their criteria can be inherent in both wet or aged insulation and homogeneous insulation, in which the absorption processes are very weak.

Consider in general form expression (3), which characterizes the absorption coefficients of insulation,

denoting $x = R_n/R_a$, and perform its study on extremes, using as independent variables the ratio of the through resistance to the absorption x and the time constant of the absorption process τ_a. The derivative with respect to x of the expression for the absorption coefficient is equal to

$$\frac{dk_a}{dx} = \frac{\exp\left(-\frac{t_2}{\tau_a}\right) - \exp\left(-\frac{t_1}{\tau_a}\right)}{\left(1 + x\exp\left(-\frac{t_1}{\tau_a}\right)\right)^2}. \quad (4)$$

According to (4), the extremum condition $dk_a/dx = 0$ is satisfied only when $x \to \infty$, i.e. at $R_n/R_a \to \infty$.

From this it follows that dk_a/dx is an increasing function from 1 with saturation by function R_n at R_a = const, or a similar function of the ratio R_n/R_a and has a one-sided maximum at infinity, the value of which depends on the absorption constant τ_a and the moments of reference time of the absorption current t_1 and t_2.

For the derivative with respect to τ_a we have:

$$\frac{dk_a}{d\tau} = \frac{\frac{t_2}{\tau_a^2}x\exp\left(-\frac{t_2}{\tau_a}\right) + \frac{t_2}{\tau_a^2}x^2\exp\left(-\frac{t_1+t_2}{\tau_a}\right) - \frac{t_1}{\tau_a^2}x\exp\left(-\frac{t_1}{\tau_a}\right) - \frac{t_1}{\tau_a^2}x^2\exp\left(-\frac{t_1+t_2}{\tau_a}\right)}{\left(1+x\exp\left(-\frac{t_1}{\tau_a}\right)\right)^2}.$$

Extreme condition $dk_a/dx = 0$ gives two possibilities. The first one is $\tau_{a\max} = \infty$ and $R_n/R_a \to \infty$. Under such conditions, the insulation cannot be defective, given that $C_a < C_g$ and has a finite value. Another option

$$t_2\exp\left(-\frac{t_2}{\tau_{a\max}}\right) + t_2x\exp\left(-\frac{t_1+t_2}{\tau_{a\max}}\right) - t_1\exp\left(-\frac{t_1}{\tau_{a\max}}\right) - t_1\exp\left(-\frac{t_1+t_2}{\tau_{a\max}}\right) = 0$$

This equation after simplification has the form

$$\frac{t_1\exp\left(-\frac{t_2}{\tau_{a\max}}\right) + t_2x\exp\left(-\frac{t_1}{\tau_{a\max}}\right)}{t_2 - t_1} = x = \frac{R_n}{R_a}. \quad (5)$$

Thus, each coefficient, which is determined by the ratio of two values of the absorption current, according to (5) has a maximum, the position of which is determined by the values of the absorption time constant $\tau_{a\max}$, i.e. the product of absorption resistance R_a and capacitance C_a, through resistance to absorption one ratio R_n/R_a, as well as the timing of the values of the absorption current t_1 and t_2. The position of the maximum will affect the values of the diagnostic parameters at this point and lead to a change in the set of values of the parameters of the equivalent circuit, which correspond to the critical value of the diagnostic parameter, which complicates the interpretation of insulation control results.

Analysis of the influence of substitution circuit parameters on absorption coefficients. Let us consider in more detail the influence of the parameters of the generalized equivalent insulation circuit on the absorption coefficients on the example of the absorption and polarization coefficients.

In the normative literature [1] when evaluating the insulation humidity of electrical engineering and electrical power equipment, as the critical value of the ohmic absorption coefficient $k_a = 1.3$ is often taken. If k_a is less, the insulation is considered wet. In the general case, the critical values of k_a can be in the range of 1.2 – 1.6. Note that the accepted interpretation of k_a as a criterion for wetting the material is not entirely accurate due to the significant dependence of its value on C_a, R_a and the absorption constant.

Indeed, the ambiguity in the interpretation of diagnostic results is due to the fact that the dependence of the absorption coefficient has a maximum not only on the absorption constant, but also separately from the absorption capacitance at a constant value of absorption resistance, and from the absorption resistance at a constant value of absorption capacitance. Therefore, we note that almost no attention is paid: for homogeneous insulation with non-blocking electrodes, the absorption capacitance C_a, and hence the absorption time constant τ_a, must be close to zero, and the absorption coefficient k_a according to (1) will be close to 1. That is, both for an ideal dielectric when the absorption time constant is close to zero due to a small value of the absorption capacitance, and for a significantly humidified dielectric when a small value of the absorption constant is due to a small value of the absorption resistance, the absorption coefficient $k_a \approx 1$. This means that the absorption coefficient dependence on the absorption constant is extreme, which is indeed the case, as shown in Fig. 2. As can be seen from Fig. 2, in the region of small values of τ_a there is a rather sharp decrease in the absorption coefficient with decreasing τ_a, and with increasing τ_a after the maximum – its gradual decline.

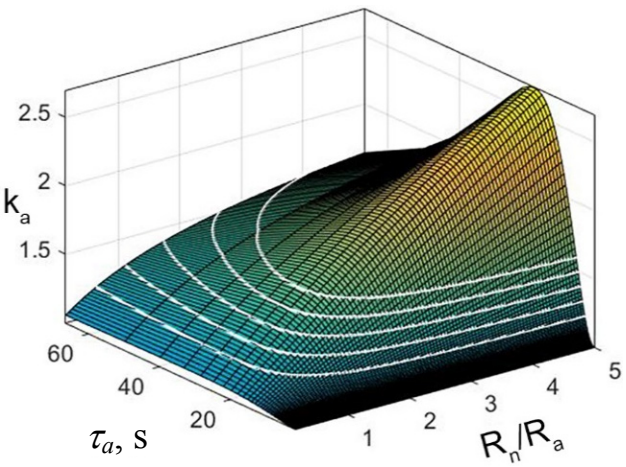

Fig. 2. Dependence of the absorption coefficient on the absorption time constant and the ratio of through resistance to absorption one. The contours for the values of the absorption coefficient 1.2 – 1.6 are shown (bottom to top)

The absorption coefficient k_a at τ_a = const has a constant value, as shown by the calculation, only at a certain ratio of R_n and absorption characteristics. As an example Fig. 2 shows a cross section of the graph by planes k_a = [1.2; 1.3; 1.4; 1.5; 1.6] which corresponds to the values of k_a which are taken as a criterion in assessing the insulation of electrical engineering and electrical power equipment.

The extreme values of k_a and time constants corresponding to them are given in Table 1. The maximum absorption coefficient k_a depending on τ_a takes place at a given ratio R_n/R_a in the range τ_a = 7.5 – 33.5 s. Two values of the absorption time constant τ_a correspond to the same value of k_a outside the maximum at R_n/R_a = const. For example, at the ratio R_n/R_a = 1 critical value k_a = 1.3 correspond to the values τ_a = 13.1 s and τ_a = 59 s, and at R_n/R_a =10 – values τ_a = 4.25 s and τ_a = 152 s.

Table 1

Parameter	R_n/R_a	0,0001	0,001	0,01	0,1	1	10	100	1000
k_a	τ_{amax}, s	32,44	32,44	32,345	31,46	25,88	16,27	10,42	7,49
	k_{amax}	1	1,0005	1,0047	1,0465	1,42	3,98	18,78	102,09
k_p	τ_{amax}, s	234	234	230	226	190	125	65,5	55
	k_{pmax}	1	1,0007	1,007	1,07	1,66	6,64	362,9	2841

Calculations at different ratios of through and absorption resistances show that the value of the time constant τ_a, which corresponds to the maximum value of k_a, is almost constant at R_n/R_a <1 and gradually decreases at R_n/R_a>1, when the absorption coefficient begins to increase markedly. As for the polarization coefficient k_p, all the qualitative regularities that take place for the absorption coefficient are preserved, but the quantitative characteristics are shifted towards larger values (Table 1). For both coefficients, the maximum value of the coefficients goes to infinity at $R_n/R_a \to \infty$ and zero τ_a. At the same time, when the value of R_n/R_a is zero, the maximum value of the absorption coefficient takes place at τ_a = 32.46 s, and for the polarization coefficient k_p at τ_a = 234 s.

Depending on the through resistance, the absorption coefficient increases monotonically with saturation from 1 to $\exp((t_2 - t_1)/\tau_a)$, where t_1 and t_2 are the time of resistance measurement after voltage application, with increasing through resistance to infinity. It should be borne in mind that $\exp((t_2 - t_1)/\tau_a)$ at $t_2 - t_1$ = const exponentially decreases with increasing τ_a, and therefore the saturation level k_a will be quite different at different absorption resistances, which is shown in Fig. 3, where the maximum value of the absorption coefficient can reach 60 at small ratios R_n/R_a and $t_2 - t_1$ = 60 s. Theoretically, at larger values of the difference $t_2 - t_1$, the maximum value of the absorption coefficient can reach several hundred.

The critical ratio of leakage resistance to absorption resistance occurs at certain values of the absorption constant (Fig. 4), which are also a function of the resistance ratio R_n/R_a. Note that the maximum values of the absorption time constant τ_{amax} for the polarization coefficient are much larger compared to its values for the absorption coefficient in the same range of values R_n/R_a.

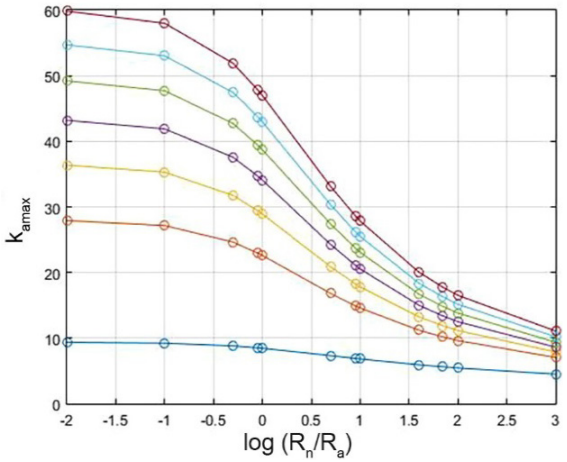

Fig. 3. Dependence of the maximum value of the absorption coefficient k_{amax} on lg(R_n/R_a) at values of a difference of moments of time of measurement of absorption current $t_2 - t_1$: 0.1, 10, 20, 30, 40, 50, 60 s (bottom to top)

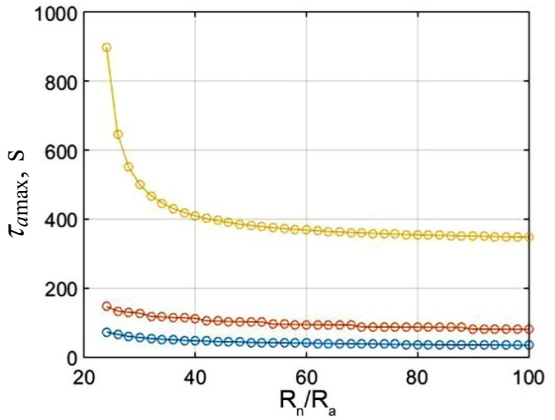

Fig. 4. The values of the absorption constant τ_{amax} corresponding to the extremum of the absorption coefficient (bottom), when t_1 = 30 and t_2 = 120 s, as well as for the polarization coefficient (upper curve) depending on R_n/R_a

Thus, the results of the simulation carried out confirm the ambiguity of the ohmic absorption coefficient and the polarization coefficient as diagnostic parameters. The ambiguity of the dependence of the absorption coefficients on τ_a and the dependence of their values on the ratio of resistances R_n/R_a leads to the impossibility of unambiguous interpretation of the results because the same value of k_a can correspond to material with satisfactory properties and material with low resistance levels. Small values of τ_a are possible both at small values of C_a characteristic of a qualitative homogeneous material, and at small values of R_a which correspond to the large microdefectivity of individual regions of this material.

For large values of τ_a which occur at large C_a and R_a, the interpretation is the opposite – the material is very inhomogeneous, but not very defective. In addition to this ambiguity, it should also be taken into account that at the same constant value of τ_a increase in C_a and corresponding decrease in R_a are responsible for deterioration of material properties, and decrease in C_a and increase in R_a – improvement, and without separate definition of these parameters it is impossible to answer, in which direction the properties of the material change.

These considerations confirm that the absorption coefficients are quite contradictory and difficult to interpret the results obtained in the process of technical diagnosis of insulation and that they can be effective if used to diagnose this type of insulation of this manufacturer after preliminary tests.

Introduction of an additional diagnostic parameter to eliminate the ambiguity of the absorption coefficients. To increase the diagnostic capacity of the absorption coefficients, which is limited by the presence of a maximum depending on their absorption time constant, it is possible to use an additional diagnostic parameter, in particular the limit value of the ratio $(R_n /R_a)_{cr}$.

As follows from Fig. 2, there is the smallest value of the ratio $(R_n /R_a)_{cr}$, with a further decrease of which the absorption coefficient will have a value only less than the criterion at any values of the absorption constant. To find the limit values of the ratio $(R_n /R_a)_{cr}$ it is necessary to substitute in (3) the criterion value of the absorption coefficient, which will give the equation of the cross section profile corresponding to this value, find the value of the absorption constant

$$\tau_{a\min} = \frac{t_2 - t_1}{\ln\left(\frac{k_a t_2}{t_1}\right)}, \qquad (6)$$

corresponding to the minimum absorption coefficient depending on the resistance ratio R_n /R_a, and then calculate $(R_n /R_a)_{cr}$, substituting $\tau_{a\min}$ in the equation:

$$\left(\frac{R_n}{R_a}\right)_{cr} = \frac{k_a - 1}{\exp\left(-\frac{t_1}{\tau_{a\min}}\right) - k_a \exp\left(-\frac{t_2}{\tau_{a\min}}\right)}. \qquad (7)$$

Calculated by (6), (7) the limit values of the ratio $(R_n/R_a)_{cr}$ for different values of the absorption and polarization coefficients, and the corresponding values of the absorption time constants corresponding to these values of the coefficients are given in Table 2.

Table 2

The values of the absorption coefficient		1,1	1,2	1,3	1,4	1,5	1,6	1,7	1,8	1,9	2,0
k_a	$(R_n/R_a)_{cr}$	0,22	0,45	0,69	0,95	1,21	1,49	1,77	2,06	2,36	2,67
	τ_{amin}, s	30,4	28,7	27,3	26,1	25,1	24,2	23,5	22,8	22,2	21,64
k_p	$(R_n/R_a)_{cr}$	0,145	0,293	0,44	0,60	0,75	0,91	1,07	1,23	1,39	1,55
	τ_{amin}, s	225	217	210	205	199	195	191	187	183	180

If we use the limits values of the absorption or polarization coefficients and the ratio $(R_n/R_a)_{cr}$ at the same time, the ambiguity of the diagnosis associated with the presence of a maximum in the absorption coefficients will be overcome.

We also give formulas for determining the limit values of the ratio $(R_n /R_a)_{cr}$ depending on the values of the absorption constant that do not correspond to the minimum.

For an absorption coefficient equal to 1.3, at 20 s < τ_a < 100 s for the limit values $(R_n /R_a)_{cr}$ we can write a linearized equation

$$\left(\frac{R_n}{R_a}\right)_{cr} = 0{,}29 + 0{,}0141 \cdot \tau_a , \qquad (8)$$

and for the polarization coefficient equal to 2 in the region 185 s < τ_a < 1250 s accordingly

$$\left(\frac{R_n}{R_a}\right)_{cr} = 0{,}215 + 0{,}00103 \cdot \tau_a . \qquad (9)$$

If the value obtained in the diagnostic test $(R_n /R_a)_{cr}$ is less than that calculated by (8), (9), the technical condition of the insulation is not satisfactory.

Note that in this case both $(R_n /R_a)_{cr}$, and τ_a should be used as diagnostic parameters. The proposed additional diagnostic parameters are auxiliary, used to eliminate the ambiguity of the main criterion of the absorption or polarization coefficient, and can be applied to the most commonly used critical values of the absorption coefficient k_a = 1.3 and the polarization coefficient k_p = 2. For larger values of the absorption coefficients, it is possible to calculate $(R_n /R_a)_{cr}$, and τ_a by the same formulas, but they will correspond to the slightly underestimated limit values of the absorption coefficients.

Conclusions.

It is shown that the absorption and polarization coefficients are extreme functions of the ratio of through and absorption resistances, absorption constant time, as well as absorption capacitance and resistance separately, which reduces their prognostic capacity and leads to ambiguous interpretation of diagnostic results.

The possibility of introducing an additional diagnostic parameter, which is the ratio of through and absorption resistances $(R_n /R_a)_{cr}$ in the minimum line of intersection of the dependence $k_a(\tau_a, R_n /R_a)$ with the plane k_a = const, to eliminate the ambiguity associated with the extremity of absorption coefficients, is justified. The limit values of the ratio of through and absorption resistances $(R_n /R_a)_{cr}$ for absorption and polarization coefficients in the range of values from 1.1 to 2 is calculated. When obtaining in the process of diagnosing insulation values of the ratio R_n /R_a less than the limit ones, at any values of absorption constant insulation state will be unsatisfactory.

Formulas for calculating the critical values of the R_n /R_a ratio at the values of the absorption time constant in the range of 20 < τ_a < 100 for k_a = 1.3 and 85 < τ_a < 1250 for the polarization coefficient k_p = 2 are proposed, which together can also be used as auxiliary diagnostic parameters for these values of the absorption coefficients.

Conflict of interest. The authors of the article declare no conflict of interest.

REFERENCES

1. *SOU-N-EE-20.302:2007. Testing norms for electrical equipment*. Kyiv, DP MOU «Voienne vydavnytstvo Ukrainy «Varta», 2007. 262 p. (Ukr).

2. Noskov V., Mezetsev M., Gavrylenko S., Heiko H. Control and diagnosis of the condition the traction electric drive. *Systems of Control, Navigation and Communication*, 2021, vol. 1, no. 63, pp. 58-61. (Ukr). doi: https://doi.org/10.26906/sunz.2021.1.058.

3. Khamevko O.N., Sushko D.L. Analysis of methods control and diagnostic parameters isolation the traction engine of direct current. *Collected scientific works of Ukrainian State University*

of Railway Transport, 2014, no. 147, pp. 152-155. (Ukr). doi: https://doi.org/10.18664/1994-7852.147.2014.75121.
4. Bezprozvannych G.V., Moskvitin E.S., Kyessayev A.G. The absorption characteristics of the phase and zone paper-impregnated insulation of power cable at direct voltage. *Electrical Engineering & Electromechanics*, 2015, no. 5, pp. 63-68. doi: https://doi.org/10.20998/2074-272X.2015.5.09.
5. Tamus Z.A., Berta I. Application of voltage response measurement on low voltage cables. *2009 IEEE Electrical Insulation Conference*, 2009, pp. 444-447. doi: https://doi.org/10.1109/EIC.2009.5166387.
6. Bezprozvannych G.V., Moskvitin E.S. Estimation criteria for degree of paper-impregnated insulated power cable ageing. *Electrical Engineering & Electromechanics*, 2013, no. 4, pp. 32-36. doi: https//doi.org/10.20998/2074-272X.2013.4.05.
7. Naboka B.G., Bezprozvannych A.V., Moscvitin E.S., Bytko M.V., Bytko S.M., Golovan A.A. Diagnostics of power system cable lines on dielectric dissipation factor and impregnated-paper insulation self-discharge time constant. *Electrical Engineering & Electromechanics*, 2011, no. 2, pp. 65-69. doi: https://doi.org/10.20998/2074-272X.2011.2.14.
8. Németh B., Csépes G., Vörös C. Applicability of the dielectric response methods of diagnostics of power transformers: Hungarian experiences. *2011 Electrical Insulation Conference (EIC)*, 2011, pp. 49-53. doi: https://doi.org/10.1109/EIC.2011.5996114.
9. Sarkar S., Sharma T., Baral A., Chatterjee B., Dey D., Chakravorti S. A new approach for determination of moisture in paper insulation of in-situ power transformers by combining polarization-depolarization current and return voltage measurement results. *IEEE Transactions on Dielectrics and Electrical Insulation*, 2013, vol. 20, no. 6, pp. 2325-2334. doi: https://doi.org/10.1109/TDEI.2013.6678886.
10. Gavrilă D.E., Ciprian I., Gavrilă H.C. Applying the Recovery Voltage Method (RVM) to Study the Degradation of High Power Transformer Insulation. *Advanced Materials Research*, 2014, vol. 911, pp. 260-265. doi: https://doi.org/10.4028/www.scientific.net/amr.911.260.
11. Mustafa E., Németh R.M., Afia R.S.A., Tamus Z.Á. Parameterization of Debye Model for Dielectrics Using Voltage Response Measurements and a Benchmark Problem. *Periodica Polytechnica Electrical Engineering and Computer Science*, 2021, vol. 65, no. 2, pp. 138-145. doi: https://doi.org/10.3311/ppee.16399.
12. Tamus Z.Á. Combination of voltage response method with non-contact electrostatic voltage measurement to determine the dielectric response of insulating materials. *Journal of Physics: Conference Series*, 2019, vol. 1322, p. 012042. doi: https://doi.org/10.1088/1742-6596/1322/1/012042.
13. Sun Y., Li Z., Han Y., Suo C. An effective method to avoid charge leakage along the surface in voltage response measurement. *Review of Scientific Instruments*, 2021, vol. 92, no. 5, p. 055104. doi: https://doi.org/10.1063/5.0051428.
14. Roziskulov S.S. Mykhailiv V.I., Hrabchuk B.L. Transient electromagnetic processes in inhomogeneous electrical isolation of high-voltage cables during its diagnosis by methods of measuring and analyzing the relaxation current and the return voltage. *Methods and devices of quality control,* 2013, no. 1(30), pp. 84-91. (Ukr). Available at: http://194.44.112.13/journals/3328p.pdf (accessed 16 June May 2021).
15. Bezprozvannych G.V., Kostiukov I.A. Error of control of electrical insulation structures by dielectric absorption parameters according to the concept of uncertainty of measurements. *Electrical Engineering & Electromechanics*, 2020, no. 1, pp. 47-51. doi: https://doi.org/10.20998/2074-272X.2020.1.07.

Received 09.10.2021
Accepted 12.11.2021
Published 03.12.2021

V.M. Kyrylenko[1]*, PhD, Associate Professor,*
K.V. Kyrylenko[1]*, PhD,*
M.O. Budko[1]*, PhD,*
P.L. Denysiuk[1]*, PhD, Associate Professor,*
[1] National Technical University of Ukraine
«Igor Sikorsky Kyiv Polytechnic Institute»,
37, Prospect Peremohy, Kyiv-56, 03056, Ukraine,
e-mail: vsemychkirg@gmail.com (Corresponding Author)

How to cite this article:
Kyrylenko V.M., Kyrylenko K.V., Budko M.O., Denysiuk P.L. Reasoning of additional diagnostic parameters for electric insulation diagnostics by absorption methods. *Electrical Engineering & Electromechanics*, 2021, no. 6, pp. 39-45. doi: https://doi.org/10.20998/2074-272X.2021.6.06.

UDC 621.311 https://doi.org/10.20998/2074-272X.2021.6.07

F. Akbar, T. Mehmood, K. Sadiq, M.F. Ullah

Optimization of accurate estimation of single diode solar photovoltaic parameters and extraction of maximum power point under different conditions

Introduction. *With the snowballing requirement of renewable resources of energy, solar energy has been an area of key concern to the increasing demand for electricity. Solar photovoltaic has gotten a considerable amount of consideration from researchers in recent years.* ***Purpose.*** *For generating nearly realistic curves for the solar cell model it is needed to estimate unknown parameters with utmost precision. The five unknown parameters include diode-ideality factor, shunt-resistance, photon-current, diode dark saturation current, and series-resistance.* ***Novelty.*** *The proposed research method hybridizes flower pollination algorithm with least square method to better estimate the unknown parameters, and produce more realistic curves.* ***Methodology.*** *The proposed method shows many promising results that are more realistic in nature, as compared to other methods. Shunt-resistance and series-resistance are considered and diode constant is not neglected in this approach that previously has been in practice. The values of series-resistance and diode-ideality factor are found using flower pollination algorithm while shunt-resistance, diode dark saturation current and photon-current are found through least square method.* ***Results.*** *The combination of these techniques has achieved better results compared to other techniques. The simulation studies are carried on MATLAB/Simulink.* References 34, tables 5, figures 10.
Key words: **maximum power point, maximum power point error, genetic algorithm, flower pollination algorithm.**

Вступ. *З огляду на величезну потребу у відновлюваних енергетичних ресурсах, сонячна енергія стала ключовою сферою розв'язання проблеми зростання попиту на електроенергію. За останні роки сонячна фотоелектрична техніка отримала значну увагу з боку дослідників.* ***Мета***. *Для створення майже реалістичних кривих для моделі сонячних батарей необхідно оцінити невідомі параметри з максимальною точністю. П'ять невідомих параметрів включають коефіцієнт ідеальності діодів, опір шунту, фотонний струм, струм темного насичення діодів і послідовний опір.* ***Новизна***. *Запропонований метод дослідження поєднує алгоритм запилення квітів із методом найменших квадратів для кращої оцінки невідомих параметрів та отримання більш реалістичних кривих.* ***Методологія***. *Запропонований метод демонструє багато перспективних результатів, які є більш реалістичними за своєю природою, порівняно з іншими методами. Розглянуто опір шунта і послідовний опір, і в цьому підході, який раніше застосовувався на практиці, не нехтують постійною діода. Значення послідовного опору та коефіцієнта ідеальності діодів визначаються за допомогою алгоритму запилення квіток, тоді як опір шунту, струм темного насичення діодів і фотонний струм - методом найменших квадратів.* ***Результати***. *Поєднання цих методів забезпечило кращі результати у порівнянні з іншими методами. Моделювання проводиться на MATLAB/Simulink.* Бібл. 34, табл. 5, рис. 10.
Ключові слова: **максимальна точка потужності, максимальна похибка точки потужності, генетичний алгоритм, алгоритм запилення квіток.**

1. Introduction. Electrical energy demand is increasing day by day due to high consumption by industries and competition among industrial community [1]. Also the electrical faults and interconnected power system make the cost and emission ratio very high [2, 3]. To meet the need of good quality electrical energy, the research interest in solar cell have increased considerably to increase the application of solar power [4]. A large amount of time and money has been invested to accurately estimate the unknown parameters of solar cell [5]. There are various methods to accurately estimate parameters i.e., analytical, numerical and meta-heuristic methods. In [6, 7] an analytical method is proposed that relies on the correct placement of the data for the exact estimation of parameters. So to better optimize and control the photovoltaic (PV) systems it is imperative to simulate the P-V characteristics before the installation of the solar panel [4, 5]. This data is collected from the data-sheet and characteristic curve of solar cell. Despite having a number of benefits like accuracy and less computational time these methods have some demerits as well i.e., in case if number of unknown parameters are large one can expect errors in result [8] and a higher computational time is also required. While in numerical methods, in contrast to analytical, every sample point from the characteristic curve of the solar cell is considered. This method generates better results as compared to the analytical methods [8, 9]. The numerical-methods, i.e., Gauss Seidel [6, 10] and Newton-Raphson [11, 12] have been in frequent use by researchers for the estimation of solar cell parameters. Although the accuracy of numerical methods is high but their dependence on accurate initial guesses has been found very difficult in case of larger number of unknowns [13, 14]. That can cause a solution to converge to local-minima rather than a global-minima. So, it is necessary to solve current optimization challenges [15-17] to sort out issues in numerical and analytical techniques. Many meta-heuristic techniques have been proposed which are genetic algorithm (GA) [18], particle swarm optimization (PSO) algorithm [19, 20], simulated annealing (SA) [21], differential algorithm (DA) [22], and teaching learning algorithm (TLA) [23].

Aforementioned techniques have been proved to be more efficient in estimating the unknown parameters of solar cell, as compared to the numerical and analytical techniques, but these techniques were slow-convergent and sometimes unable to track accurate characteristics [8, 9]. Computational time got considerably reduced in some of these research works either by ignoring shunt resistance R_{sh} [24, 25], series resistance R_s [26, 27] or by presuming the ideality factor n of the diode [8]. These efforts lead to a less-accurate estimation of maximum power point error (MPPE) [14, 28]. To enhance the

accuracy, this research works takes in account all the five electrical model parameters.

Aims and goals. The research work has following contributions:

1. Series resistance R_s and ideality factor V_{di} are estimated using flower pollination algorithm (FPA).
2. The other 3 remaining parameters, namely shunt resistance R_{sh}, photon current I_{phn}, and saturation current I_d are estimated using the least square (LS) method. The LS method helps to improve the FPA.
3. Two different PV cells are opted and used to examine the performance of the proposed method. Performance parameters such as maximum power point (MPP), MPPE and P-V characteristics curve are checked compared with the existing and proposed method to prove the effectiveness of proposed method.

The research paper is organized in sections and the detail is as: Section 2 encompasses the work done related to this topic which is already published. Section 3 presents the mathematical modelling and objective function derivation of single-diode cell model. Section 4 contains explanation of proposed technique. In section 5, the results and discussions about application of technique on different solar cells will be presented and a comparison will be made with different works already published. Section 6 presents the conclusion.

Literature review. From 2006 to 2016, the PV installations across the globe are increased from 7 GW to 300 GW. The foremost reason for large upsurge in the installations of PV systems is an increase in costs by the amount of 2.5 to 3.5 times. The elementary code for the PV systems is to seizure light of sun with a PV module and convert it direct into electrical energy. The output for a PV module, is dependent on the climatical circumstances i.e., temperature and irradiance, is denoted with a single-diode-model [14].

The model of single-diode imitates extremely precise yield characteristics of diverse types of PV cells and modules for any type climatic circumstances. For the analysis of PV systems, it is frequently favored over the contemporaries' ones because of it having fewer parameters and fewer complexities in computations

$$I = I_L - I_0 \cdot \left(e^{\frac{q \cdot (V + I \cdot R_s)}{n \cdot K \cdot T}} - 1 \right) - \frac{V + I \cdot R_S}{R_{sh}}, \qquad (1)$$

where I_L is the current generated by light; I_0 is the reverse saturation current; q is the elementary charge ($1.602 \cdot 10^{-19}$ C); V is the voltage; n is the ideality factor of the diode; K is the Boltzmann constant ($1.38 \cdot 10^{-23}$ J/K); T is the temperature; R_s is the series resistance; R_{sh} is the shunt resistance.

The 5 factors to be defined are: I_L, I_0, R_s, R_{sh} and n. In equation (1) I is an understood function, such that $I = f(V, I)$. Therefore, the precise analytic explanation for I is not feasible and the solution is taken with the help of iterative methods, i.e., Gauss-Seidel and Newton-Raphson. To devise $I = f(V)$ and to alleviate the process of solution, numerous explicit expressions of analytical methods occur in the published work. They employ calculations for example polynomial, Taylor series, Padé, and Chebyshev. For the single diode model, the 5 undetermined parameters determine functionality of a PV module in any climatic circumstances. Two approaches exist to discover the parameters:

1) with investigational information;
2) from the key-power points stated in the manufacturer's datasheet.

The highlights in the datasheet has problem that they can only devise 4 equations alongside 5 parameters to be resolved. To ease the problem, a discrete n value is supposed to resolve the 4 equations, but the parameters acquired may not be appropriate. To design 5th equation, De Soto [29] utilized the open-circuit situation at a temperature which is not according to the standard test conditions. Although, the final explanation's vulnerable to a selected range of a temperature. An enhanced 5th equation is developed that correlates n and the open circuit voltage (V_{oc}). The slope dI/dV at short circuit condition is believed to be 5th equation that is equivalent to negative inverse of R_{sh}, but it is only valid if $R_{sh} >> R_s$ and is mainly applicable for modules of silicon and it might flunk for solar cells of thin-film solar. Consequently, the dilemma is there to choose the 5th equation that achieves the process of solution. This research presents technique that approximate the 5 unknown parameters of the single-diode model is produced. Highlight of the method is that the design of the 5th equation uses an accurate area under the I–V curve with other 4 equations derived from datasheet values. The recommended technique deems an I–V set of data of a PV cell/module as it requires the area under the curve. This technique also demonstrates an approach for pondering for 5 parameters' initial guesses. The recommended technique gets applied to earlier state few cells like copper indium gallium selenide, silicon, dye-sensitized and perovskite.

2. Related works. Many research works have been published which propose different methods to extract unknown parameters of solar cells. All the methods have advantages and merits related to it but they also have some demerits.

2.1. Numerical methods. The numerical methods are still in use, but they still depend on initial guesses for accuracy. If initial guesses are wrong, the solution gets converged to local minima that is a disadvantage. Gauss Seidel [6, 10] and Newton-Raphson [11, 12] are the examples of some numerical methods.

2.2. Meta-heuristic methods. Meta-heuristic techniques are mostly inspired by nature optimization problems which give accurate and close to real optimization results with very small uncertainty possibilities. Even with slightly wrong initial guesses they give accurate results. They are more likely to make solution convergence at global optima, but these methods can cause the convergence time to be long and iteration to be large making it a little unfeasible. GA [18], PSO [19], [20], SA [21], DA [22], and TLA [23] are some meta-heuristic algorithms.

It is concluded from above discussion that every technique possesses some merits and demerits related to it that doesn't make it to be a perfect choice for parameter estimation. The proposed technique hybridized both

numerical and meta-heuristic methods to devise a new reliable and effective method.

3. Mathematical modelling of solar cell and objective function. Simplicity and accuracy of single diode model makes it a good choice for considering it to use for parameter estimation [30, 31], and is shown in Fig. 1, in which R_s represents the bulk and metal contact resistance, R_{sh} represents electron holes pairs recombination, I_d is the diode dark saturation current, I_o is output current, I_{phn} is photon current and V_L is output voltage.

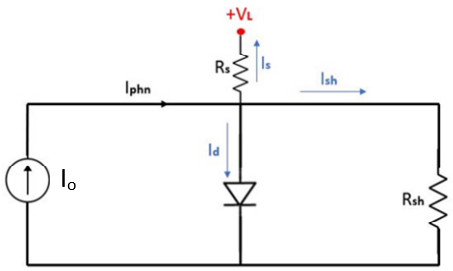

Fig. 1. Electrical circuit diagram for single diode model

The relationship between I_o and V_L is given in next equation:

$$I_o = I_{phn} - I_d \cdot \left(e^{\left(\frac{V_L + I_o \cdot R_s}{V_{di}} \right)} - 1 \right) - \frac{V_L + I_o \cdot R_s}{R_{sh}}, \quad (2)$$

where V_{di} is the diode internal voltage:

$$V_{di} = \frac{n \cdot K \cdot T \cdot S_{cs}}{q},$$

where S_{cs} is the number of cells connected in series.

The parameters that aren't stated in manufacturer datasheet and are yet to be determined are: I_{phn}, I_d, R_s, R_{sh}, and V_{di}. It is evident from (1), (2) that the characteristic curve relies on unknown parameters stated earlier. So, precise and accurate estimation of these unknown parameters is imperative.

So, the necessary set of equations that are needed for estimating undetermined parameters are following:

1. I_s is obtained by putting load voltage V_L = 0 in Eq. (1) and making a short circuit at the load

$$I_o = I_{phn} - I_d \cdot \left(e^{\left(\frac{I_s \cdot R_s}{V_{di}} \right)} - 1 \right) - \frac{I_s \cdot R_s}{R_{sh}}. \quad (3)$$

2. Following equation is obtained by putting I_o = 0 in Eq. (1) and open circuiting the load terminal of the solar PV

$$I_{phn} - I_d \cdot \left(e^{\left(\frac{V_{oc}}{V_{di}} \right)} - 1 \right) - \frac{V_{oc}}{R_{sh}} = 0. \quad (4)$$

3. By putting maximum power point voltage V_{mp} and maximum power point current I_{mp} in (1):

$$I_{mpp} = I_{phn} - I_d \cdot \left(e^{\left(\frac{V_{mpp} + I_{mpp} \cdot R_s}{V_{di}} \right)} - 1 \right) - \frac{V_{mpp} + I_{mpp} \cdot R_s}{R_{sh}}. \quad (5)$$

4. *P-V* curve at MPP is obtained by drawing a tangent parallel to the voltage axis

$$dP / dv_{mpp} = 0. \quad (6)$$

After solving (6) we have:

$$dI_o / dV_{L\,mpp} = -I_{mpp} / V_{mpp}. \quad (7)$$

Using Eq. (1) and (7), the following final equation is obtained:

$$I_{mpp} = \left(V_{mpp} - I_{mpp} \cdot R_s \right) \cdot \left(\frac{I_d}{V_{di}} \cdot e^{\left(\frac{V_{mpp} + I_{mpp} \cdot R_s}{V_{di}} \right)} - \frac{1}{R_{sh}} \right) = 0. \quad (8)$$

5. At short circuit condition, the obtained slope:

$$dI_o / dV_{L\,I-I_s} = -1 / R_{sh}. \quad (9)$$

6. By solving Eq. (9):

$$\frac{I_d}{V_{di}} \cdot e^{\left(\frac{I_s \cdot R_s}{V_{di}} \right)} \cdot \left(R_{sh} - R_s \right) = \frac{R_s}{R_{sh}}. \quad (10)$$

So, (3), (4), (5), (8), and (10) are needed for estimating 5 unknown parameters.

The R_s and V_{di} will be used to derive the characteristic equation for solar P-V curve. FPA is applied on characteristic equation to estimate the 2 unknowns (R_s and V_{di}). Since characteristic equation depends on 2 parameters only so it makes solutions to convergence faster and accurate.

Following are the steps to derive the proposed characteristics equation.

The value of I_{phn} is taken from Eq. (4) and is substituted in (3), (5) to get the expression for I_s and I_{mp}, as follows:

$$I_s = (y - x) \cdot I_d + \frac{V_{oc} - I_s \cdot R_s}{R_{sh}}; \quad (11)$$

$$I_{mpp} = (y - z) \cdot I_o + \frac{V_{oc} - V_{mpp} - I_{mpp} \cdot R_s}{R_{sh}}; \quad (12)$$

where:

$$x = e^{\left(\frac{I_{sc} \cdot R_s}{V_{di}} \right)} - 1; \quad y = e^{\left(\frac{V_{oc}}{V_{di}} \right)} - 1; \quad z = e^{\left(\frac{V_{mpp} + I_{mpp} \cdot R_s}{V_{di}} \right)} - 1.$$

To find expressions for I_s and I_{mp} in terms of R_s, R_{sh} and V_{di}, the value of I_o is taken from Eq. (10) and is substituted in (8), (11), (12) which gives:

$$I_s = \frac{(y - x) \cdot V_{di} \cdot R_s}{R_{sh} \cdot (1 + x) \cdot (R_{sh} - R_s)} + \frac{V_{oc} - I_s \cdot R_s}{R_{sh}}; \quad (13)$$

$$I_{mpp} = \frac{(y - z) \cdot V_{di} \cdot R_s}{R_{sh} \cdot (1 + x) \cdot (R_{sh} - R_s)} + \frac{V_{oc} - V_{mpp} - I_{mpp} \cdot R_s}{R_{sh}}; \quad (14)$$

$$I_{mpp} = \left(V_{mpp} - I_{mpp} \cdot R_s \right) \cdot \left(\frac{R_s + (1 + z)}{R_{sh} \cdot (1 + x) \cdot (R_{sh} - R_s)} + \frac{1}{R_{sh}} \right); \quad (15)$$

Equations (14), (15) are equated to get R_{sh}:

$$R_{sh} = R_s + \left(\frac{R_s}{2 \cdot V_{mpp} - V_{oc}} \right) \times \left(\frac{V_{di} \cdot (y - z) - (1 + z) \cdot \left(V_{mpp} - I_{mpp} \cdot R_s \right)}{1 + x} \right); \quad (16)$$

The R_{sh} can also be derived (13), (14) as follows:

$$R_{sh}=\frac{V_{oc}\cdot(x-z)+I_s\cdot R_s\cdot(z-y)+(V_{mpp}+I_{mpp}\cdot R_s)\cdot(y-x)}{I_{sc}\cdot(y-z)+I_{mpp}\cdot(x-y)}; \quad (17)$$

The proposed equation is derived by using Eq. (16) and (17), as follows:

$$f(R_s,V_{di})=\left[R_s+\frac{R_s}{2\cdot V_{mpp}-V_{oc}}\cdot\left(\frac{V_{di}\cdot(y-z)}{1+x}\right)-\left(\frac{-(1+z)\cdot(V_{mpp}-I_{mpp}\cdot R_s)}{1+x}\right)\right]-R_{sh}=0. \quad (18)$$

So, (18) can only be used to estimate the values of R_s and V_{di}. This model has only 2 unknowns instead 5 that makes it converge at a faster rate and generate accurate results. Equation (18) is a non-linear single-objective optimization function, and FPA is used to minimize it. The edge of this thing is that computation time is reduced number of equations required (five) have been reduced to 4 for estimating 5 parameters.

4. Proposed technique. The proposed technique employs FPA and least square method to estimate 5 unknown parameters. FPA is a nature inspired meta-heuristic optimization algorithm, and least square is a numerical method. Both the methods are briefly explained below and depicted in Fig. 2.

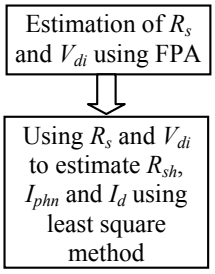

Fig. 2. Flow chart for proposed technique

4.1. Flower pollination algorithm (FPA). In 2012 Yang proposed a meta-heuristic algorithm called FPA that is inspired by the process of pollination in flowering plants [32]. This cross-pollination is considered as global pollination while self-pollination is considered as local pollination for the process of evolution. Optimization capability of FPA is very good and it also has fast convergence rate. Many research studies have proven FPA to be better than contemporaries like PSO and GA in multi-peak test functions [32].

There are 2 ways of pollination in flowering plants, one is cross pollination and other is self-pollination as shown in Fig. 3. Birds, bees and insects act as pollinators in cross-pollination that carry pollens at long distances so that they cross the gap among flowers and facilitate in pollen exchange with flowers far away. So, this heterogeneous pollination in FPA is called global pollination. The transfer of pollens with flowers around with help of pollinators i.e., air/wind is called self-pollination and it is termed as local pollination in FPA.

The decision whether pollination is going to be cross or self is being dealt by a parameter p called probability switch. To make the problem easy, it's supposed that each plant possesses one flower and every flower owns only one pollen that is a possible solution to the problem.

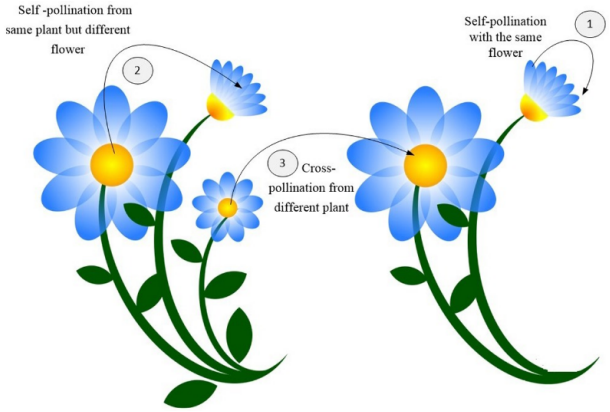

Fig. 3. Process of flower pollination

4.1.1. Global pollination. Global pollination is carried by birds or insects which follow Levy flight characteristics which means the step size for global pollination obeys Levy distribution. Global pollination is described mathematically as:

$$X_i^{t+1}=X_i^t+\gamma\cdot L\cdot\left(X_{best}-X_i^t\right); \quad (19)$$

where X_{best} represents the best individual solution in the iterations happened so far; X_i^t is the t^{th} generation solution (current generation); X_i^{t+1} is the $(t+1)^{\text{th}}$ generation solution (next generation); L represents the intensity of global pollination that is the step size of pollen movement; γ is a scaling factor that controls step size.

The mathematical description of Levy distribution is as follows:

$$L=\frac{\lambda\cdot\Gamma(\lambda)\cdot\sin\left(\frac{\lambda\cdot\pi}{2}\right)}{\pi}\cdot\frac{1}{S^{1+\lambda}},\left(S>>S^0>0\right), \quad (20)$$

where $\Gamma(\lambda)$ represents the standard gamma function; S is Levy flight step size; S^0 is the minimum step size; λ is a constant ($\lambda=1.5$).

The S is generated by use of technique in [28] as follows:

$$S=\frac{U}{|V|^{1/\lambda}};\ \text{for}\ U\sim N\left(0,\sigma^2\right),V\sim N(0,1), \quad (21)$$

$$\Sigma^2=\frac{\Gamma(1+\lambda)\cdot\sin(\lambda\cdot\pi/2)}{\Gamma\left[\left(\frac{1+\lambda}{2}\right)\right]\cdot\lambda\cdot2^{\frac{\lambda-1}{2}}}, \quad (22)$$

where U and V obey the Gaussian distribution [32].

4.1.2. Local pollination. Local pollination happens between nearby plants and is done by abiotic sources like

wind. The mathematical representation of local pollination is:

$$X_i^{t+1} = X_i^t + \varepsilon \cdot \left(X_j^t - X_k^t\right), \quad \varepsilon \sim U(0,1); \qquad (23)$$

where X_i^{t+1} is the single solution generated at $(t+1)^{\text{th}}$ generation; X_j^t and X_k^t represent the j^{th} and k^{th} individual solutions respectively in the t^{th} generation, and ε represents the local pollination coefficient which is uniformly distributed in [0, 1].

4.1.3. Switching probability. Among global and local pollination, the decisive factor is called switch of probability that is represented by p. In [32], it has been proved that when p = 0.8, it gives good results. How p decides is given as:

$$\text{Pollination Mode} = \begin{cases} \text{Global Pollination}, & r < p; \\ \text{Local Pollination}, & \text{otherwise}, \end{cases}$$

where $r \in [0, 1]$.

The fitness evaluation of FPA is calculated as

$$Fitness = fit(X), \qquad (24)$$

where X is an individual solution in the population, and the t represents the abstract expression of the optimization problem. It is to be noted that for different optimization problems, the mathematical expressions could be different.

The flowchart of FPA is shown in Fig. 4.

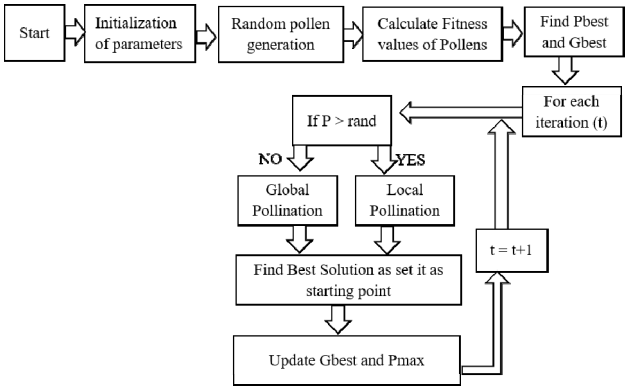

Fig. 4. Flowchart of FPA

4.2. Least square method. The LS method [33] is an important numerical method which is used to obtain a regression line or a line that best-suits for a provided pattern. It's defined with an equation that contains particular parameters. It's mostly utilized in evaluation and regression. When used in regression, known as a standard approach for the approximation of set of equations that contains more number of equations than the number of unknowns.

The LS in fact explains the solution for the minimization of the sum of squares of deviations or the errors in the result of each equation, and finds the formula for sum of squares of errors, which facilitates to look for the fluctuations and variations in observed or experimental data.

The LS is mostly utilized in data fitting. The result which best-fits is expected to reduce the sum of squared errors or residuals that are differences between the observed/experimental values, and corresponding fitted value given in the model.

4.2.1. Least square method graph. For linear regression, the straight line is a best fitting line, as shown in the Fig. 5.

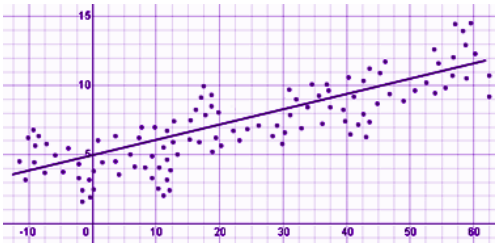

Fig. 5. Linear regression – line of best fit

The given data points are aimed to be minimized using the technique of reducing residuals or offsets of each data point from the straight line. Surface, polynomial, and hyperplane problems often use vertical offset. While in common practices, perpendicular offsets are utilized as shown in Fig. 6.

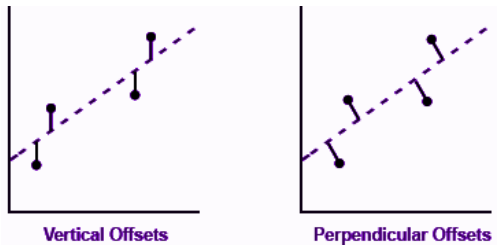

Fig. 6. Method of reducing offsets

5. Results and discussion. Two solar cell models are considered from [34], and are mentioned in Table 1, 2. Using values from tables, parameters are estimated using proposed technique and are compared with recently published research works to prove the efficiency.

Table 1

STM-640-36-Manufacturer's datasheet

Datasheet parameters variables	STM-640-36
$P_{\max}$, W	25.47
V_{mp}, V	16.98
I_{mp}, mA	1.50
V_{oc}, V	21.02
I_{sc}, mA	1.663
S_{cs}, units	36
T, °C	51

Table 2

JP-270-M60-Manufacturer's datasheet

Datasheet parameters variables	JP-270-M60
$P_{\max}$, W	269.948
V_{mp}, V	31.10
I_{mp}, mA	8.68
V_{oc}, V	38.60
I_{sc}, mA	9.20
S_{cs}, units	60
T, °C	25

5.1. Estimation of P-V characteristic curve with LS, GA, LS hybrid with GA and proposed method is represented in Table 3, 4.

Table 3

Estimated parameters of STM-640-36
with LS, GA, LS hybrid with GA and proposed method

Name of the solar cell	Parameters to be estimated	Least square (LS)	Genetic algorithm (GA)	LS hybrid with GA [31]	Proposed method
STM-640-36	I_{phn}, mA	1.6634	1.6637	1.664	1.6642
	I_d, mA	$1.1225e^{-6}$	$9.8541 \cdot 10^{-7}$	$9.0122 \cdot 10^{-7}$	$9.0081 \cdot 10^{-7}$
	R_s, Ω	0.2704	0.23695	0.2254	0.235
	R_{sh}, Ω	504.234	502.9223	488.2172	484
	V_{di}, V	1.4891	1.4678	1.4582	2.356
	A, W	–	–	1.57636	1.5781

Table 4

Estimated parameters of JP-270-M60
with LS, GA, LS hybrid with GA and proposed method

Name of the solar cell	Parameters to be estimated	Least square (LS)	Genetic algorithm (GA)	LS hybrid with GA [31]	Proposed method
JP-270-M60	I_{phn}, mA	9.1987	9.2003	9.1974	9.1976
	I_d, mA	$1.0259 \cdot 10^{-9}$	$1.1940 \cdot 10^{-9}$	$1.0110 \cdot 10^{-9}$	$1.013 \cdot 10^{-9}$
	R_s, Ω	0.3142	0.30985	0.3043	0.09095
	R_{sh}, Ω	9100.1	9137.8	9192.9	9198
	V_{di}, V	1.6844	1.69706	1.684	2.3
	A, W	–	–	1.0906032	1.0307

Using these results from Table 3, 4, the *P-V* characteristics curve are obtained and are shown in Fig. 7–10.

It is clear from the *P-V* curves that the proposed approach is much closer to the MPP as compared to the other contemporary methods. Evaluation of parameters show that more realistic curves are produced using the proposed method in comparison to other methods. So, it is conclude that the proposed method produces way better results as compared to contemporary methods.

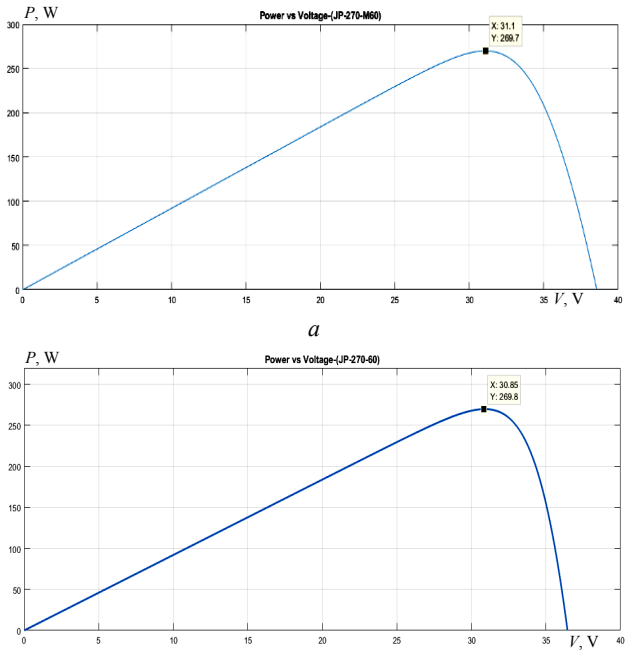

Fig. 7. Solar cell JP-270-M60:
(*a*) *P-V* curve of LS-GA; (*b*) *P-V* curve of proposed method

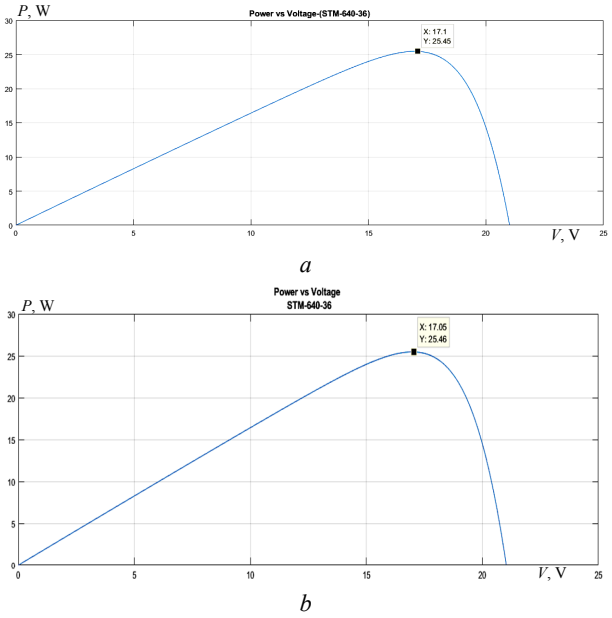

Fig. 8. Solar cell STM-640-36:
(*a*) *P-V* curve of LS-GA; (*b*) *P-V* curve of proposed method

Figure 7 shows that out of JP-270-M60 of 270 W, and LS-GA was able to extract 269.7 W of power where proposed approach succeeded to extract 269.8 W that surpasses the LS-GA proving it to be the better in terms of parameter extraction.

Figure 8 shows that out of STM-640-36 of 25.47 W, and LS-GA extracted 25.45 W while proposed method extracted 25.46 W.

Figures 9, 10 show the comparative analysis of both Fig. 7, 8 to prove the effectiveness of proposed scheme.

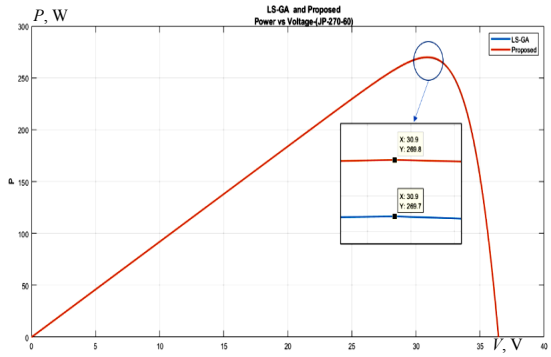

Fig. 9. JP-270-60 comparison between LS-GA and proposed method

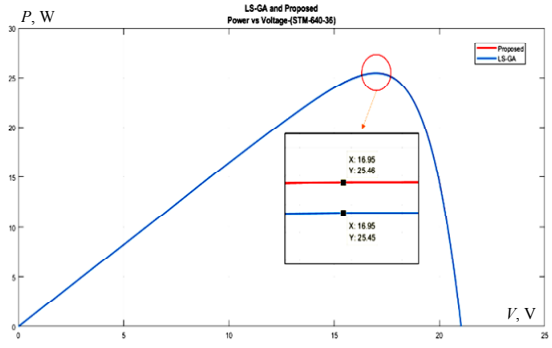

Fig. 10. STM-640-36 comparison between LS-GA and proposed method

5.2. Estimation of *P-V* maximum power point error with proposed, SA and Newton-Raphson and

least square method. MPPE is defined as the measured difference between the rated power P_{rated} and the calculated power. This MPPE for different techniques have been summarized in Table 5. It is observed from Table 5 that the MPPE for the proposed method is least among all as compared to other methods.

Table 5

Comparison of MPP, MPPE between LS, GA, LS-GA and proposed method

Parameter	Methods	JP-270-M60	STM-640-36
P_{rated}, W		269.948	25.47
P_{mpp}, W	LS	269.4701	25.4251
	GA	269.6605	25.4391
	LS-GA	269.7208	25.4585
	Proposed	269.8	25.46
MPPE	LS	0.17703	0.17628
	GA	0.10650	0.12131
	LS-GA	0.08416	0.04515
	Proposed	0.0548	0.000392

6. Conclusions.

In this paper, characteristic equation in terms series resistance and diode-ideality factor are derived. Flower pollination algorithm is utilized on characteristic equation to estimate series resistance and diode-ideality factor. Least square method is utilized to estimate the remaining parameters such as shunt-resistance, photon-current, and diode dark saturation current. For the purpose of simulations and validations, 2 different solar cell models are considered. *P-V* curves and maximum power point error are calculated using proposed technique. Solar panel of 270 W, hybrid least square and genetic algorithm was able to extract 269.7 W of power where proposed approach succeeded to extract 269.8 W that surpasses the hybrid least square and genetic algorithm proving it to be the better in terms of parameter extraction. Shunt and series resistances are considered and are not neglected in this approach that previously has been in practice. Also the number of equations is reduced that brings the edge of less computation burden. This will help producers and consumers in acquiring efficient solar panels that will increase electricity output and better revenue. This research for solar cell/panel can be utilized in energy storage system of distribution static compensator to efficiently improve the power quality in distribution system.

Conflict of interest. The authors declare that they have no conflicts of interest.

REFERENCES

1. Ullah M.F., Hanif A. Power quality improvement in distribution system using distribution static compensator with super twisting sliding mode control. *International Transactions on Electrical Energy Systems*, 2021, vol. 31, no. 9, art. no. e12997 doi: https://doi.org/10.1002/2050-7038.12997.

2. Anwar N., Hanif A.H., Khan H.F., Ullah M.F. Transient stability analysis of the IEEE-9 bus system under multiple contingencies. *Engineering, Technology & Applied Science Research*, 2020, vol. 10, no. 4, pp. 5925-5932. doi: https://doi.org/10.48084/etasr.3273.

3. Mehdi M.F., Ahmad A., Ul Haq S.S., Saqib M., Ullah M.F. Dynamic economic emission dispatch using whale optimization algorithm for multi-objective function. *Electrical Engineering & Electromechanics*, 2021, no. 2, pp. 64-69. doi: https://doi.org/10.20998/2074-272x.2021.2.09.

4. Ahmed W., Sheikh J.A., Ahmad S., Farjana S.H., Mahmud M.A.P. Impact of PV system orientation angle accuracy on greenhouse gases mitigation. *Case Studies in Thermal Engineering*, 2021, vol. 23, p. 100815. doi: https://doi.org/10.1016/j.csite.2020.100815.

5. Ahmed W., Sheikh J.A., Kouzani A.Z., Mahmud M.A.P. The Role of single end-users and producers on GHG mitigation in Pakistan – a case study. *Sustainability*, 2020, vol. 12, no. 20, p. 8351. doi: https://doi.org/10.3390/su12208351.

6. Shongwe S., Hanif M. Comparative analysis of different single-diode PV modeling methods. *IEEE Journal of Photovoltaics*, 2015, vol. 5, no. 3, pp. 938-946. doi: https://doi.org/10.1109/jphotov.2015.2395137.

7. Sarquis Filho E.A., Fernandes C.A.F., Da Costa Branco P.J. A complete framework for the simulation of photovoltaic arrays under mismatch conditions. *Solar Energy*, 2021, vol. 213, pp. 13-26. doi: https://doi.org/10.1016/j.solener.2020.10.055.

8. Appelbaum J., Peled A. Parameters extraction of solar cells – a comparative examination of three methods. *Solar Energy Materials and Solar Cells*, 2014, vol. 122, pp. 164-173. doi: https://doi.org/10.1016/j.solmat.2013.11.011.

9. Yetayew T.T., Jyothsna T.R. Parameter extraction of photovoltaic modules using Newton Raphson and simulated annealing techniques. *2015 IEEE Power, Communication and Information Technology Conference (PCITC)*, 2015, pp. 229-234. doi: https://doi.org/10.1109/pcitc.2015.7438166.

10. Shongwe S., Hanif M. Gauss-Seidel iteration based parameter estimation for a single diode model of a PV module. *2015 IEEE Electrical Power and Energy Conference (EPEC)*, 2015, pp. 278-284. doi: https://doi.org/10.1109/EPEC.2015.7379963.

11. Chatterjee A., Keyhani A., Kapoor D. Identification of photovoltaic source models. *IEEE Transactions on Energy Conversion*, 2011, vol. 26, no. 3, pp. 883-889. doi: https://doi.org/10.1109/TEC.2011.2159268.

12. Uoya M., Koizumi H. A calculation method of photovoltaic array's operating point for MPPT evaluation based on one-dimensional Newton–Raphson method. *IEEE Transactions on Industry Applications*, 2015, vol. 51, no. 1, pp. 567-575. doi: https://doi.org/10.1109/tia.2014.2326083.

13. Accarino J., Petrone G., Ramos-Paja C.A., Spagnuolo G. Symbolic algebra for the calculation of the series and parallel resistances in PV module model. *2013 International Conference on Clean Electrical Power (ICCEP)*, 2013, pp. 62-66. doi: https://doi.org/10.1109/ICCEP.2013.6586967.

14. Huang P., Xiao W., Peng J.C.-H., Kirtley J.L. Comprehensive parameterization of solar cell: improved accuracy with simulation efficiency. *IEEE Transactions on Industrial Electronics*, 2016, vol. 63, no. 3, pp. 1549-1560. doi: https://doi.org/10.1109/TIE.2015.2498139.

15. Shahzad A., Lee M., Lee Y.-K., Kim S., Xiong N., Choi J.-Y., Cho Y. Real time MODBUS transmissions and cryptography security designs and enhancements of protocol sensitive information. *Symmetry*, 2015, vol. 7, no. 3, pp. 1176-1210. doi: https://doi.org/10.3390/sym7031176.

16. Zhang Q., Zhou C., Xiong N., Qin Y., Li X., Huang S. Multimodel-based incident prediction and risk assessment in dynamic cybersecurity protection for industrial control systems. *IEEE Transactions on Systems, Man, and Cybernetics: Systems*, 2016, vol. 46, no. 10, pp. 1429-1444. doi: https://doi.org/10.1109/TSMC.2015.2503399.

17. Huang K., Zhang Q., Zhou C., Xiong N., Qin Y. An efficient intrusion detection approach for visual sensor networks based on traffic pattern learning. *IEEE Transactions on Systems, Man, and Cybernetics: Systems*, 2017, vol. 47, no. 10, pp. 2704-2713. doi: https://doi.org/10.1109/TSMC.2017.2698457.

18. Zagrouba M., Sellami A., Bouaïcha M., Ksouri M. Identification of PV solar cells and modules parameters using

the genetic algorithms: Application to maximum power extraction. *Solar Energy*, 2010, vol. 84, no. 5, pp. 860-866. doi: https://doi.org/10.1016/j.solener.2010.02.012.
19. Ye M., Wang X., Xu Y. Parameter extraction of solar cells using particle swarm optimization. *Journal of Applied Physics*, 2009, vol. 105, no. 9, p. 094502. doi: https://doi.org/10.1063/1.3122082.
20. Khanna V., Das B.K., Bisht D., Vandana, Singh P.K. A three diode model for industrial solar cells and estimation of solar cell parameters using PSO algorithm. *Renewable Energy*, 2015, vol. 78, pp. 105-113. doi: https://doi.org/10.1016/j.renene.2014.12.072.
21. El-Naggar K.M., AlRashidi M.R., AlHajri M.F., Al-Othman A.K. Simulated Annealing algorithm for photovoltaic parameters identification. *Solar Energy*, 2012, vol. 86, no. 1, pp. 266-274. doi: https://doi.org/10.1016/j.solener.2011.09.032.
22. Jiang L.L., Maskell D.L., Patra J.C. Parameter estimation of solar cells and modules using an improved adaptive differential evolution algorithm. *Applied Energy*, 2013, vol. 112, pp. 185-193. doi: https://doi.org/10.1016/j.apenergy.2013.06.004.
23. Patel S.J., Panchal A.K., Kheraj V. Extraction of solar cell parameters from a single current–voltage characteristic using teaching learning based optimization algorithm. *Applied Energy*, 2014, vol. 119, pp. 384-393. doi: https://doi.org/10.1016/j.apenergy.2014.01.027.
24. Celik A.N., Acikgoz N. Modelling and experimental verification of the operating current of mono-crystalline photovoltaic modules using four- and five-parameter models. *Applied Energy*, 2007, vol. 84, no. 1, pp. 1-15. doi: https://doi.org/10.1016/j.apenergy.2006.04.007.
25. Vijayakumari A., Devarajan A.T., Devarajan N. Design and development of a model-based hardware simulator for photovoltaic array. *International Journal of Electrical Power & Energy Systems*, 2012, vol. 43, no. 1, pp. 40-46. doi: https://doi.org/10.1016/j.ijepes.2012.04.049.
26. Tan Y.T., Kirschen D.S., Jenkins N. A model of PV generation suitable for stability analysis. *IEEE Transactions on Energy Conversion*, 2004, vol. 19, no. 4, pp. 748-755. doi: https://doi.org/10.1109/tec.2004.827707.
27. Benavides N.D., Chapman P.L. Modeling the effect of voltage ripple on the power output of photovoltaic modules. *IEEE Transactions on Industrial Electronics*, 2008, vol. 55, no. 7, pp. 2638-2643. doi: https://doi.org/10.1109/TIE.2008.921442.
28. Bharadwaj P., Chaudhury K.N., John V. Sequential optimization for PV panel parameter estimation. *IEEE Journal of Photovoltaics*, 2016, vol. 6, no. 5, pp. 1261-1268. doi: https://doi.org/10.1109/JPHOTOV.2016.2574128.
29. De Soto W., Klein S.A., Beckman W.A. Improvement and validation of a model for photovoltaic array performance. *Solar Energy*, 2006, vol. 80, no. 1, pp. 78-88. doi: http://dx.doi.org/10.1016/j.solener.2005.06.010.
30. Xiao W., Edwin F.F., Spagnuolo G., Jatskevich J. Efficient approaches for modeling and simulating photovoltaic power systems. *IEEE Journal of Photovoltaics*, 2013, vol. 3, no. 1, pp. 500-508. doi: https://doi.org/10.1109/JPHOTOV.2012.2226435.
31. Silva E.A., Bradaschia F., Cavalcanti M.C., Nascimento A.J. Parameter estimation method to improve the accuracy of photovoltaic electrical model. *IEEE Journal of Photovoltaics*, 2016, vol. 6, no. 1, pp. 278-285. doi: https://doi.org/10.1109/JPHOTOV.2015.2483369.
32. Yang X.-S. Flower Pollination Algorithm for Global Optimization. In: Durand-Lose J., Jonoska N. (eds) *Unconventional Computation and Natural Computation. UCNC 2012. Lecture Notes in Computer Science*, vol. 7445. Springer, Berlin, Heidelberg. doi: https://doi.org/10.1007/978-3-642-32894-7_27.
33. Nayak B.K., Mohapatra A., Mohanty K.B. Parameters estimation of photovoltaic module using nonlinear least square algorithm: A comparative study. *2013 Annual IEEE India Conference (INDICON)*, 2013, pp. 1-6. doi: https://doi.org/10.1109/INDCON.2013.6726120.
34. Tong N.T., Pora W. A parameter extraction technique exploiting intrinsic properties of solar cells. *Applied Energy*, 2016, vol. 176, pp. 104-115. doi: https://doi.org/10.1016/j.apenergy.2016.05.064.
35. Zain-Ul-Abdin, Mahmood T., Shorfuzzaman M., Xiong N.N., Mehmood R.M. Aiding prosumers by solar cell parameter optimization using a hybrid technique for achieving near realistic P-V characteristics. *IEEE Access*, 2020, vol. 8, pp. 225416-225423. doi: https://doi.org/10.1109/ACCESS.2020.3043941.

Received 25.07.2021
Accepted 30.10.2021
Published 03.12.2021

Faizan Akbar[1], *MS,*
Tahir Mahmood[1], *Professor,*
Kamran Sadiq[1], *MS,*
Mian Farhan Ullah[2], *PhD Scholar, Lecturer*,
[1] Department of Electrical Engineering,
University of Engineering and Technology, Taxila, Pakistan,
e-mail: engr.faizanakbar@gmail.com,
tahir.mehmood@uettaxila.edu.pk,
kamransadiqawan@gmail.com
[2] Department of Mechatronics Engineering,
Wah Engineering College, University of Wah,
Quaid Avenue, Wah Cantt, Rawalpindi District,
Punjab 47040, Pakistan,
e-mail: farhan.ullah@wecuw.edu.pk (Corresponding author)

How to cite this article:
Akbar F., Mehmood T., Sadiq K., Ullah M.F. Optimization of accurate estimation of single diode solar photovoltaic parameters and extraction of maximum power point under different conditions. *Electrical Engineering & Electromechanics*, 2021, no. 6, pp. 46-53. doi: https://doi.org/10.20998/2074-272X.2021.6.07.

UDC 620.91 https://doi.org/10.20998/2074-272X.2021.6.08

S.A. Khan, T. Mahmood, K.S. Awan

A nature based novel maximum power point tracking algorithm for partial shading conditions

Introduction. *The huge demand of green energy over past few decades have drawn the interest of scientists and researchers. Solar energy is the most abundant and easily available source but there have been so many problems with its optimum extraction of output. The factors affecting the maximum power point tracking of PV systems are input irradiance, temperature, load etc. The variations in irradiance level lead to partial shading that causes reduction in performance by not letting system to operate at maximum power point. Many methods have been proposed in literature to optimize the performance of PV systems but each method has shortcomings that have failed all of them. The actual problem occurs when partial shading is very strong; this is where most of the methods totally fail. So proposed work addresses this issue and solves it to the fullest.* ***The novelty*** *in the proposed work is that it introduces a new nature-based algorithm that works on the principle of plant propagation. It is a natural optimization technique that plants follow to survive and propagate in different environmental conditions. The proposed method efficiently tracks the global peak under all shading conditions and is simple to implement with high accuracy and tracking speed.* ***Purpose.*** *Building an algorithm that can track global peak of photovoltaic systems under all shading conditions and extracts the maximum possible power from the system, and is simple and easy to implement.* ***Methods.*** *The method is implemented in MATLAB / Simulink on an electrical model that uses a PV array model. Different shadings are applied to check for the results.* ***Results.*** *The results have shown that for different photovoltaic configurations the algorithm performs very good under uniform and partial shadings conditions. Its accuracy, tracking efficiency and tracking time has increased reasonably.* ***Practical value.*** *The project can be very beneficial to people as it enhances the performances of PV systems that can make them self-sufficient in electrical energy, focuses on sustainable development and reduces pollution. This way it can have huge impact on human life.* References 40, tables 5, figures 18.

Key words: **renewable energy, partial shading conditions, maximum power point, global maximum power point, local maximum power point, seeds, runners.**

Вступ. *Величезний попит на зелену енергію за останні кілька десятиліть привернув увагу вчених та дослідників. Сонячна енергія є найбільш поширеним і доступним джерелом, але мало місце дуже багато проблем з оптимальним отриманням виробленої енергії. Факторами, що впливають на відстеження точки максимальної потужності фотоелектричних систем, є вхідна освітленість, температура, навантаження та ін. Зміни рівня освітленості призводять до часткового затемнення, яке викликає зниження продуктивності, не дозволяючи системі працювати на максимальній точці потужності. У літературі було запропоновано багато методів для оптимізації роботи фотоелектричних систем, але кожен метод має недоліки, які стримують їх використання. Реальні проблеми виникають, коли часткове затемнення дуже сильне; саме в цьому випадку більшість методів демонструють свої найбільші недоліки. Отже, запропонована робота присвячена цій проблемі та вирішує її повною мірою.* ***Новизна*** *запропонованої роботи полягає в тому, що вона запроваджує новий природний алгоритм, що працює за принципом розмноження рослин. Це природний метод оптимізації, якому слідують рослини, щоб вижити і розмножуватися в різних умовах навколишнього середовища. Запропонований метод ефективно відстежує глобальний пік за всіх умов затемнення, є простим у реалізації з високою точністю та швидкістю відстеження.* ***Мета***. *Побудова алгоритму, який може відстежувати глобальні піки фотоелектричних систем при всіх умовах затінення та виділяти з системи максимально можливу потужність, є простим і легким у реалізації.* ***Методи.*** *Метод реалізований у MATLAB/Simulink на електричній моделі, яка використовує модель фотоелектричних елементів. Для перевірки результатів застосовуються різні затемнення.* ***Результати***. *Результати показали, що для різних фотоелектричних конфігурацій алгоритм дуже добре працює в умовах рівномірного та часткового затемнення. Його точність, ефективність відстеження та час відстеження значно збільшились.* ***Практична цінність***. *Проект може бути дуже корисним, оскільки він покращує характеристики фотоелектричних систем, що може зробити їх самодостатніми в електроенергетиці, концентрується на сталому розвитку та скорочує забруднення довкілля. Таким чином, це може мати величезний вплив на життя людини.* Бібл. 40, табл. 5, рис. 18.

Ключові слова: **відновлювана енергія, умови часткового затемнення, точка максимальної потужності, глобальна точка максимальної потужності, локальна точка максимальної потужності, насіння, пагони.**

1. Introduction. Immense use of electronic appliances in this era [1], rapid consumption of fossil fuels [2], atmospheric issues, and energy crisis [3] have attracted wide attention toward usage and exploration of renewable energy (RE). But, these sources have the disadvantage of limited storage of the energy and tapping of power. Due to the lacking of storage mechanism, there is a high need for extraction of this abundant energy, especially during day-time [1]. The high yield from these RE sources is obtained only when researchers are able to enhance the efficiencies in both outstanding parameters like conversion and energy storage. The photovoltaic (PV) energy is abundantly available source among RE sources because it is universal, it is easily and freely available, eco-friendly, has less operational and maintenance cost, it is economically attractive for longer duration of time, driving an increasing load with greenhouse source and technologically expanding in its material usage, and is noiseless [1, 3]. PV systems have been in high demand over the past decade with its total global installation amount of more than 500 GW [4]. Clean electrical energy can be obtained form solar energy using PV arrays. PV arrays are made by making parallel and series combination of PV modules and that make a basic part of PV systems. The PV array has a high nonlinear relation between output current and voltage and it depends mainly on atmospheric conditions like temperature and irradiance. Under uniform conditions the P-V curve contains one peak while multiple peaks appear when in partial shading conditions (PSCs) that includes local peaks (LMPPs) and a global peak (GMPP) [2]. However, the main hinderance for PV panels have been their low energy efficiency because of nonlinearity

in I-V behavior that has its dependence on atmospheric conditions [3]. Solar PV systems are being controlled with many maximum power point tracking (MPPT) techniques to optimize the output power of PV array. Furthermore, there are many internal and external factors affecting the output efficiency of PV system such as solar irradiation, series and parallel resistance, internal temperature, diode factor, load, PV array surface, shadow, dirt, and so on. For improving efficiency of system, it is imperative to have an MPPT that can improve converter output power efficiency and tracking speed [5]. The output power mainly depends on the parameters like cell temperature (T), irradiation (G) and load connected to it [1]. We know that MPPT matches the operating point and it is usually mounted between PV arrays and converters as shown in Fig. 1.

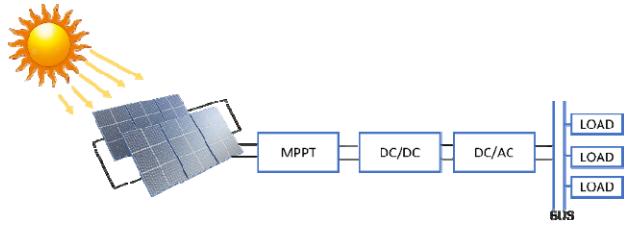

Fig. 1. Solar PV system with MPPT mechanism

Temperature and irradiance levels are utilized by MPPT methods to harvest optimum power from PV system and to determine the output characteristics. Unfortunately, there is a negative effect of non-linear behavior of irradiance and temperature on PV system's efficiency. Due to these reasons, when irradiance is varying the I-V and P-V curves of PV system get multiple peaks on them that are referred as LMPPs and a GMPP. This condition is shown in Fig. 2, 3 [5].

Fig. 2. PV array

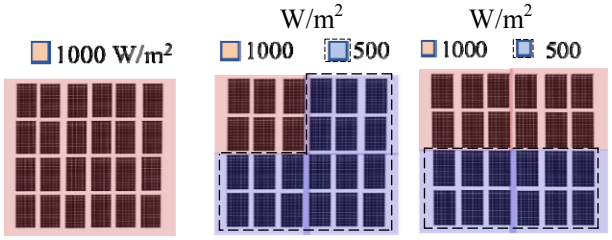

a *b* *c*

Fig. 3. Shading over a PV array (*a*) uniform shading (*b*, *c*) partial shading

Many MPPTs have been suggested to optimize the PV system's performance, but the confusion occurs when one has to pick one technique for a particular PV system as each method has their merits and demerits [5]. Generally the evaluation criteria for performance of MPPT techniques include accuracy of tracking and a response that is stable at steady and transient state [6]. To make a successful MPPT technique to work on PV arrays, it's imperative for it to operate at GMPP not LMPP and it should work under varying irradiance conditions [2].

This manuscript is divided into sections as: section 2 describes other MPPT techniques in literature. Section 3 presents the proposed technique, section 4 presents the simulation studies and discussion, and section 5 gives the concluding remarks.

2. Literature review. The work [7] presented a two-step method that is based on the GMPP tracking that tracks more effectively than Particle Swarm Optimization (PSO) in PSCs. But the problem with it is that this is a complex algorithm that makes use of three different methods to look for GMPP and for sudden changes. In [8] C. Huang proposed a technique that tracks the MPP at a faster speed based on a natural cubic-spline-based prediction model and it is incorporated into the iterative search process. The iterative processes are computationally burdening and also since the proposed method is a model-free algorithm that has a demerit that the environmental dynamics can't be judged with it. R.F. Coelho et al. in [9] presented a new method that proposes an MPPT sensor that is temperature based and from the aspect of design it is very sophisticated. This method works on the fact that the voltage of module depends directly on the surface temperature of PV panel. But because of dependence on temperature the effects of irradiation changes and load changes get ignored and ultimately attaining MPPT gets affected. N. Karami et al. in [10] described at least 40 methods that include advanced classical methods for example three-point weight comparison method, parasitic comparison, method, intelligent, and optimized techniques. The methods are not effective enough to be used in all the conditions.

Perturb and Observe (P&O) algorithm is among classical algorithms which uses slope of PV curve to extract the maximum power from the PV panel, but there are oscillations around MPP in the output of the P&O algorithm [11]. The work in [12] presented a method that changes the perturbation steps during transient operation by utilizing a fixed scaling factor with Incremental Conductance (IC) to solve the problems occurred in P&O algorithm. It removes the oscillations that occur around MPP and increases the efficiency. The method still is comparatively more time consuming and hard to implement. In [13] the authors designed an MPPT method that is called delta P&O in which a variable step size is advised to enhance MPP Tracking but oscillations around MPP are still there that causes power fluctuations at steady state. The paper [14] proposed an MPPT technique that perturbs the voltage and the duty cycle but still isn't effective in PSCs and has oscillations around MPP. In [15] another hybrid technique of P&O was proposed that hybridized fuzzy logic with P&O. The performance analysis of the technique has shown some overshoots and oscillations at output. The article [16] proposed a technique that lacks the current-sensor and where PV voltage and cell temperature is measured and from where PV current can be calculated using a look up table [17]. However, this technique is complex and is unreliable because of difficulties in temperature calculation and accuracy in model.

The paper [5] reviewed nearly all necessary and in-stream methods that have been tried to extract MPP under shading conditions. In the category for uniform shading it mentioned some online and offline methods. In online methods, P&O method [18], IC method [19], Hill Climbing (HC) method [20], Beta (β) method [21], Current Sweep (CS) method [22], Constant Current (CC) method [23], Curve Fitting (CF) method [24], Pilot Cell (PC) method [25], Lookup Table (LT) method [26], Load Voltage and Load Current (LV & LC) maximization method [27], and PV output senseless (PVOS) method [28]. All the techniques used for uniform shading have oscillations around MPP which decreases the power and also they can't perform under partial shading conditions. For non-uniform shading conditions, there are many hybrid techniques that have been proposed to serve the purpose of GMPP tracking that include Perturb & Observe with Genetic Algorithm (P&O-GA) [29] & Perturb & Observe with Particle Swarm Optimization (P&O-PSO) [30], Incremental Conductance with Particle Swarm Optimization (INC-PSO) [31], Hybrid Grey Wolf Optimization with Fuzzy Logic Controller (GWO-FLC) [32], Hill Climbing with Adaptive Neuro-Fuzzy Inference System (HC-ANFIS) [33], Modified Hill-Climbing with Fuzzy Logic Control (MHCL-FLC) [34], Improved Artificial Neural Network with Particle Swarm Optimization (IANN-PSO) [35], and Incremental Conductance with Simple Moving voltage Average (INC-SMVA) [36]. The above mentioned methods have been effective in dealing with uniform shading conditions but when shading is strong they fail to track GMPP and stuck at local peaks. The research work [37] proposed Flower Pollination algorithm (FPA) for GMPP tracking in PSCs and [38] utilized FPA and hybridized it with Opposition based Learning (FPA-OBL) that has a great potential of performing under partial shading conditions but this technique gets complicated when implementation is done as it involves a machine learning technique as well.

All above mentioned methods have been effective to some extent to track MPP in uniform shading and GMPP in non-uniform shading conditions but still there is a need of more work and exploration to increase the efficiency and output. The diversity in algorithms is always better as it gives number of choices to adopt a technique on the basis of their merits and demerits. This paper proposes a novel nature inspired algorithm that has been in use for some other scientific purposes [39] but has never been utilized in MPPT. In this paper it has been used for GMPP tracking under uniform and PSCs.

The aim of the paper is development of an algorithm that can track global maximum power point of photovoltaic systems under all shading conditions and extracts the maximum possible power from the system, and is simple and easy to implement.

This research work advises a new technique to attain GMPP of PV arrays in PSCs. The algorithm is naturally inspired by the process of plant propagation specifically the strawberry plant propagation. The proposed technique is a single algorithm and is easily to implement with less parameters, and its approximation strength is so strong that it catches GMPP even in hardest of the irradiance changes. The simulation studies are carried in MATLAB / Simulink and are compared to other frequently used MPPT algorithms.

3. Proposed technique.

The survival approach of strawberry plant through an adapted propagation strategy:

The plant of strawberry [39] lies in Rose family category. The industry of strawberry fruit started from Paris in the 17th century with its European type. Amedee-Francois Frezier (mathematician and engineer) was hired for drawing South America's Map, when returned from Chile in 1714, brought Chilean type of strawberry plant that has a bigger size fruit. The modern plant is a result of different crossings and evolution.

A. Propagation Strategy

The pure plants generally propagate using seeds, but the most modern hybrid species are infertile that they can't propagate using seeds so they use runners. The runners work in this way: the parent plant send runners or root that when they touch ground, they grow roots from where daughter plants grow. The runners are produced on a principle that follows a reaction to stimuli, for example a stronger plant will grow a concentration of small plants around it but a weaker plant will grow small number of plant but at a longer distance. That means stronger plant which is at a good atmospheric condition i.e., light and humidity, sends short runners but a weak plant which isn't at a good atmospheric condition sends runners less in number but longer in length to look for a good atmospheric condition for its survival. The runners are sent in all directions but more runners are sent towards a better spot. This happens because of what we call tropism or a response of growth to a stimulus [40].

B. Assumptions from Observations

Keeping in view the observations made above, it is supposed that the plant in order to flourish in an atmospheric condition, goes through a survival optimization problem and those who can solve it they survive. The inspiration got from this survival of plant makes us use this approach as an optimization tools that looks for good solutions to an objective function in a solution space and gives best values in the end.

C. Designing an Optimization Problem from Strawberry Plant's Survival Strategy

Let's say the problem to be optimized is:

$$f(x) = \max_{x \in S} Z \,, \tag{1}$$

where x represents a point in search space S.

The job of survival optimization is to look for the finest position x in the domain S that can provide the finest growth $f(x)$ for the daughter generation.

The Algorithm Strawberry Plant Propagation (SPPA)

The algorithms who search for global optimization usually have two characteristics i.e., concentration and exploration. In concentration, the algorithm searches locally and converges at a local optimum while in exploration it avoids local optimum and goes for global optimum solution. Both these characteristics are conflicting and a successful algorithm will have a balance between them. In strawberry propagation, concentration is implemented by sending short runners in large number to search for good solutions and diversification is

implemented when fewer runners are sent that are longer in length as compared to the solutions that are not at good spot. The pseudo code of algorithm is presented in Fig. 4.

Require: objective $f(x)$, $x \in R^n$
Generate a population P = $\{p_i, i = 1,...,m\}$
g ← 1
  for g ← 1 to g_{max}
      do
      compute $N_i = f(p_i)$, $\forall\, p_i \in$ P
      sort P in descending order of N
      create new population ϕ
          for each pi; $i = 1,..., m$
              do {best m only}
              r_i ← set of runners where both the size of the set and the distance for each runner (individually) is proportional to the fitness N_i
              $\phi \leftarrow \phi \cup r_i$ {append to population; death occurs by omission above}
          end for
          P ← ϕ {new population}
  end for
return P, the population of solutions

Fig. 4. The plant propagation algorithm (PPA)

Similar too many other algorithms in nature, SPPA also need some variables, functions and initial values. For SPPA they are a fitness function, population size, number of generations, number of runners and distance if each runner.

The algorithm works on the basis of population of shoots where every shoot in a population is a representative of a solution in the *S*. Every shoot is supposed that it has grown a root that is similar as the evaluation of an objective function. Every shoot sends out runners to explore *S*. The number of shoots is denoted by a variable *m* in the algorithm.

The SPPA is naturally iteration based and at each generation, all shoots send out runner. There is a parameter g_{max} that gives a termination criteria on the basis of which it is decided that how many times to send out runners.

Solutions are sorted based on their fitness values. The fitness value of runners is dependent on objective function's values, but the real relation among values of objective function and fitness could be modified for a specific problem. However, the SPPA believes that $f(x) \in [0, 1]$; if it doesn't, the equations are needed to be modified that are utilized to decide the numbers of runners and the distance for each. Presented below are some case studies and the actual fitness functions for each case will be presented along with the problem statements.

The number of runners and the distance each runs are determined by the functions that are presented below. The functions have a requirement that the fitness must lie in the range (0, 1). The mapping of fitness value, $f(x)$, is done to satisfy the following equation:

$$N(x) = (\tanh(4 \cdot f(x) - 2) + 1). \quad (2)$$

Figure 5 depicts the effect of mapping function. The necessity of this mapping is described below. This mapping facilitates with a way of finding even more better solutions over less-good ones.

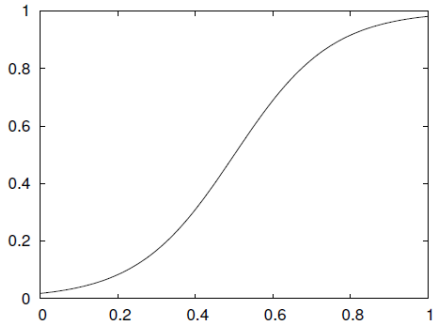

Fig. 5. Effects of mapping function that is used to convert fitness values from [0; 1] to (0; 1) and emphasizing more better solutions

The numbers of runners that are produced are proportional to fitness values. The function used by default is:

$$n_r = [n_{max} \,.\, N_i \,.\, r], \quad (3)$$

where n_r represents the numbers of runners generated for the solution i in the present population; n_{max} gives the max number of runners to be generated; N_i represents the fitness, that is mapped (using (2)), of solution i, and $r \in [0, 1]$ is a random number for every solution in every generation.

Fitness mapping function and ceiling operator when combined make sure that at least one runner is generated by each single solution, and even for the solutions that least in the fittests, and ones that have $f_i(x) = 0$. The n_{max} number of runners is generated by fittest solutions. And for different studies here, n_{max} is kept $n_{max} = 5$. The distance travelled by every runner obeys a same principle. That distance is described as:

$$d_{r,j} = 2 \cdot (1 - N_i) \cdot (r - 0.5), \quad (4)$$

where n is the search space dimension.

For $j = 1,...,n$ each $d_{r,j}$ belongs from (–1, 1). It is made sure by the fitness mapping function that the best solutions will possess the capacity to throw runners out at a distance > 0 even if $f_i(x) = 1$. The distance computed will be utilized to renew the solution i on the basis of the bounds on x_j:

$$x^*_j = x_j + (b_j - a_j) \cdot d_{r,j}. \quad (5)$$

The values of x^*_j are managed in such a way that it is made sure that the newly created points are within the limits $[a_j, b_j]$.

4. Simulations, results and discussions. The electrical model used for simulations is shown in Fig. 6 and values of components are listed in Table 1. The PV module used is SunPower SPR-305E-WHT-D and its characteristics are shown in Table 2, 3.

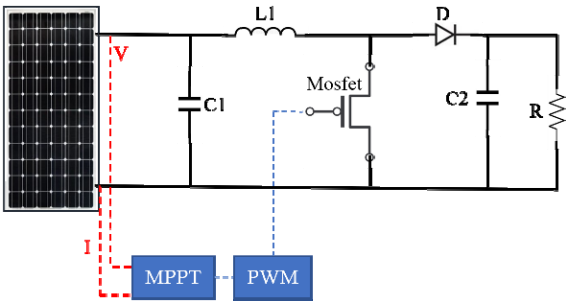

Fig. 6. Electrical circuit for simulation studies

Table 1

Values of electrical components used for simulations

Components	Symbols	Values
Capacitor 1	C1	1×10^{-5} F
Capacitor 2	C2	1×10^{-5} F
Inductor	L1	10×10^{-3} H
Resistor	R	variable Ω

Table 2

Characteristic parameters of SunPower SPR-305E-WHT-D

Parameters	Symbols	Values
Max power	P_{MPP}	305 W
Open circuit voltage	V_{OC}	64.2 V
Short circuit current	I_{SC}	5.96 A
Current at P_{max}	I_{MPP}	5.58 A
Voltage at P_{max}	V_{MPP}	54.7 V
Temp. coefficient of current I_{sc}	K_I	0.06 %/K
Temp. coefficient of voltage V_{oc}	K_V	–0.173 V/K
No. of cells per module	N_S	96

Table 3

Boost converter's parameters

Parameters	Symbols	Values
Device on state resistance	R_{ON}	1×10^{-3} Ω
Snubber resistance	R_S	1×10^{6} Ω
Snubber capacitance	C_S	inf F
Forward voltages [device V_f, diode V_{fd}]	V_F	[0, 0] V
Diode forward voltage	V_{fd}	1×10^{-3} V
Current source snubber resistance	R_{Is}	inf Ω

The configurations of PV arrays used are 1s1p, 2s1p and 3s1p as shown in Fig. 7. The simulation results for configurations are elaborated separately below.

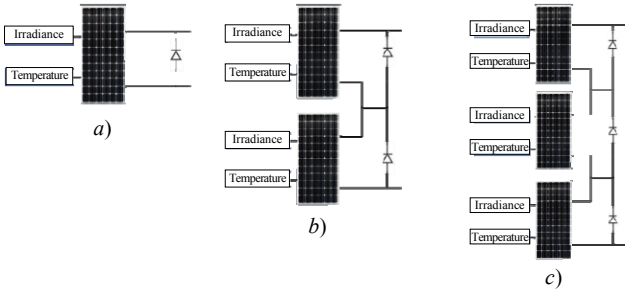

Fig. 7. PV arrays configurations: (*a*) 1s1p; (*b*) 2s1p; (*c*) 3s1p

The simulations done on above configuration are discussed here as:

Configuration 1s1p.

Since 1s1p has only one PV module in it so it can have only uniform shading conditions as in the Fig. 7 is shown. The characteristic curves and power extraction curves using proposed technique for 1s1p are at 100 and 500 W/m^2 shown in Fig. 8, 9. For 1000 W/m^2 the rated power is 300.88204 W and power extracted using PPA is 300.88054 W which is 99.99 % efficient in this case.

While for 500 W/m^2 the rated power is 148.77592 W and extracted power using PPA is 148.67529 W which has an efficiency of 99.93 %. The MPP tracking ability of PPA is very high in uniform shading conditions as it is seen from above discussed results.

Configuration 2s1p.

Figures 10–13 show output results of 2s1p configurations under different shading patterns. Figure 10 shows rated curves and output power curve of 2s1p at 1000, 1000 W/m^2. The rated power is 605.64547 W and power extracted using PPA is 605.14782 W with efficiency of 99.91 %. Figure 11 shows curves for 1000, 500 W/m^2 where rated power is 324.38211 W while that extracted using PPA is 323.75138 W, which has an efficiency of 99.8 %. This was partial shading conditions where shading at two PV panels was different that makes shift the MPP and PPA quite accurately tracked MPP.

Figure 12 shows curves for 500, 500 W/m^2 that has rated power of 301.27333 W while extracted power is 301.04306 W with efficiency of 99.92 %. Similarly, Fig. 13 also shows graphs for rated power and extracted power at 200, 100 W/m^2. The rated power in that case is 61.74939 W and extracted power is 61.26584 W with efficiency of 99.21 %.

Configuration 3s1p.

Figures 14–18 present characteristic curves and output curves for 3s1p at different shading patterns. Figure 14 shows curves for 1000, 1000, 1000 W/m^2 where rated power is 912.51031 W while extracted power is 912.16287 W that has an efficiency of 99.95 %.

Figure 15 shows curves for 1000, 750, 500 W/m^2 where rated power is 496.11087 W and extracted power is 495.49489 W that has an efficiency of 99.87 %.

Figure 16 shows curves for 1000, 750, 750 W/m^2 where rated power 705.90873 W and extracted power is 705.52431 W with 99.94 % efficiency.

Figure 17 shows curves for 1000, 500, 500 W/m^2 where rated power is 474.246 W and extracted output power is 474.19434 W with efficiency of 99.98 %.

Figure 18 shows curves for 500, 500, 500 W/m^2 where rated power 451.81051 W and extracted power is 451.16105 W which has an efficiency of 99.85 %.

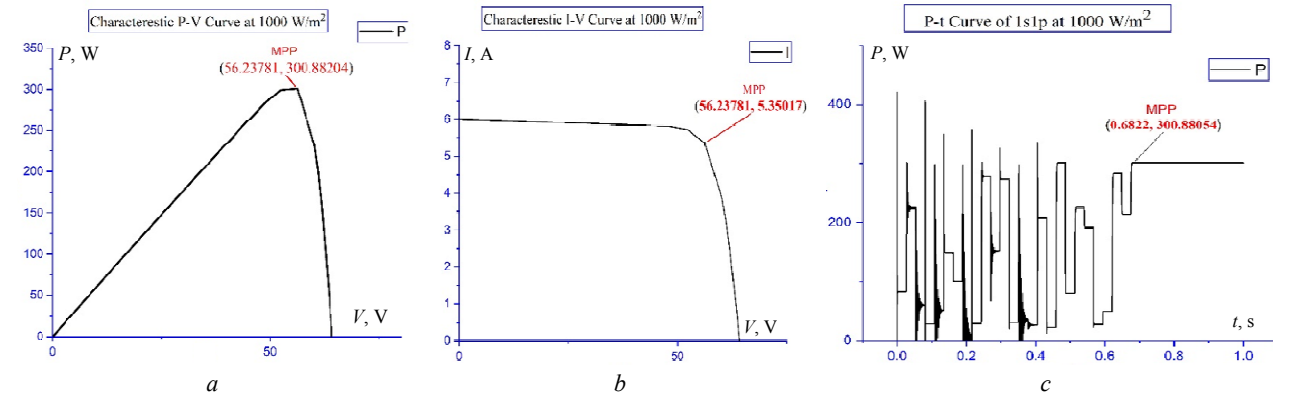

Fig. 8. 1s1p at irradiance of 1000 W/m^2:
(*a*) – characteristic P-V curve; (*b*) – characteristic I-V curve; (*c*) – power extracted using proposed method

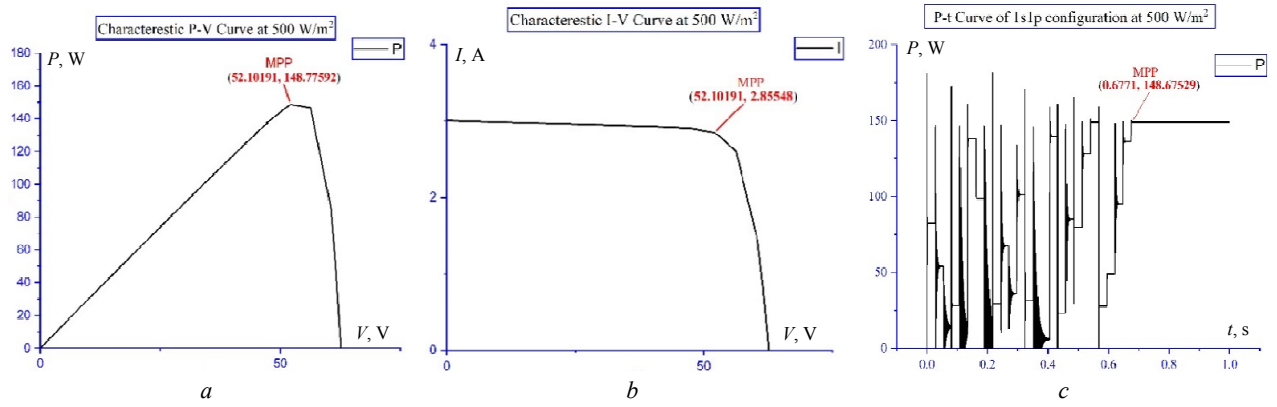

a *b* *c*

Fig. 9. 1s1p at irradiance of 500 W/m^2:
(*a*) – characteristic P-V curve; (*b*) – characteristic I-V curve; (*c*) – power extracted using proposed method

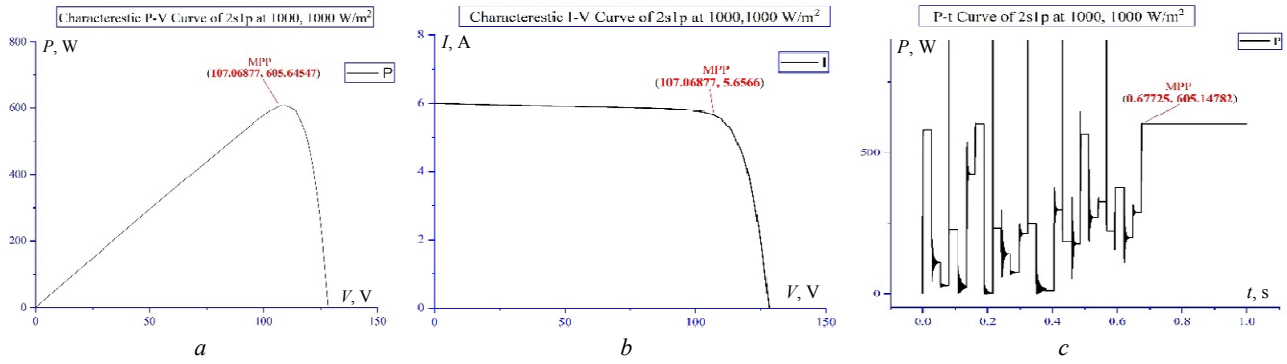

a *b* *c*

Fig. 10. 2s1p at irradiance of 1000, 1000 W/m^2:
(*a*) – characteristic P-V curve; (*b*) – characteristic I-V curve; (*c*) – power extracted using proposed method

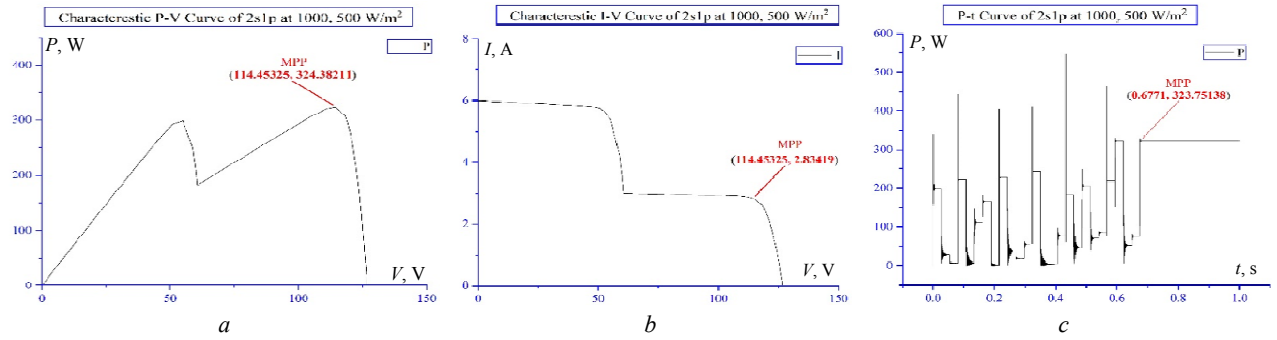

a *b* *c*

Fig. 11. 2s1p at irradiance of 1000, 500 W/m^2:
(*a*) – characteristic P-V curve; (*b*) – characteristic I-V curve; (*c*) – power extracted using proposed method

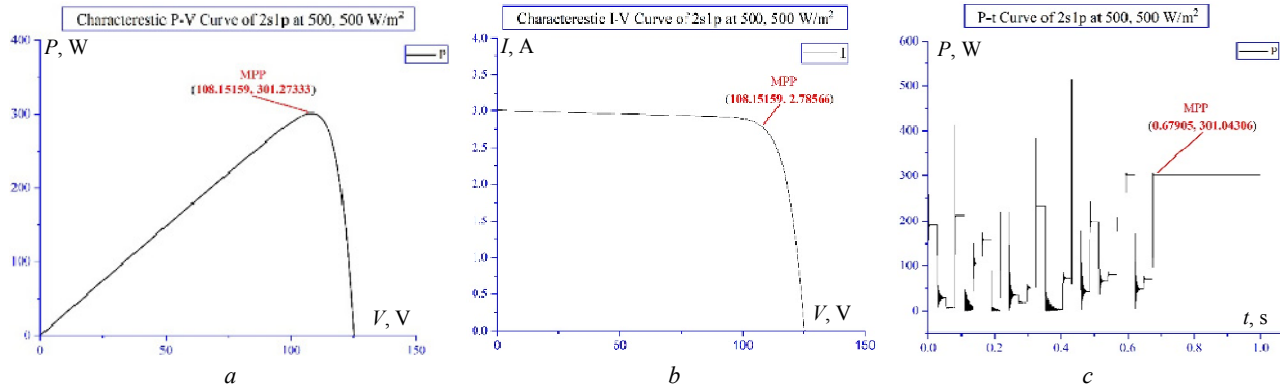

a *b* *c*

Fig. 12. 2s1p at irradiance of 500, 500 W/m^2:
(*a*) – characteristic P-V curve; (*b*) – characteristic I-V curve; (*c*) – power extracted using proposed method

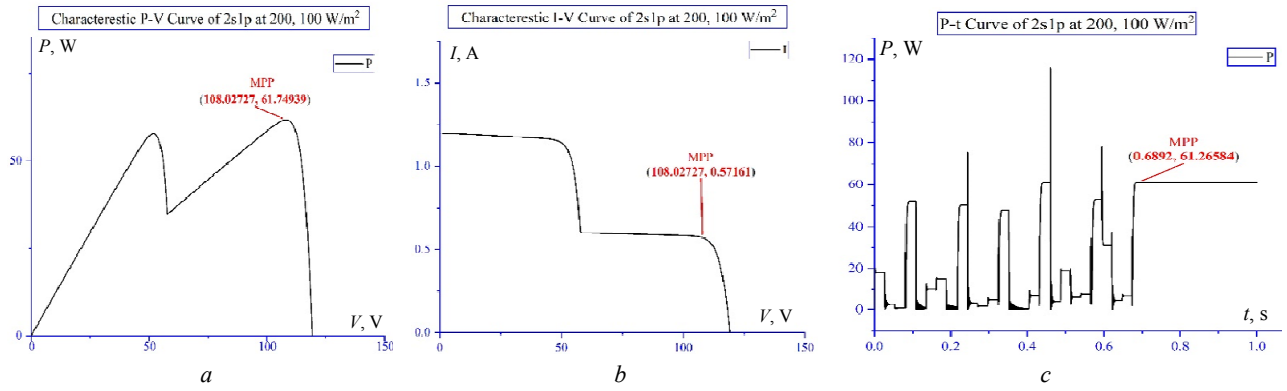

a *b* *c*

Fig. 13. 2s1p at irradiance of 200, 100 W/m^2:
(*a*) – characteristic P-V curve; (*b*) – characteristic I-V curve; (*c*) – power extracted using proposed method

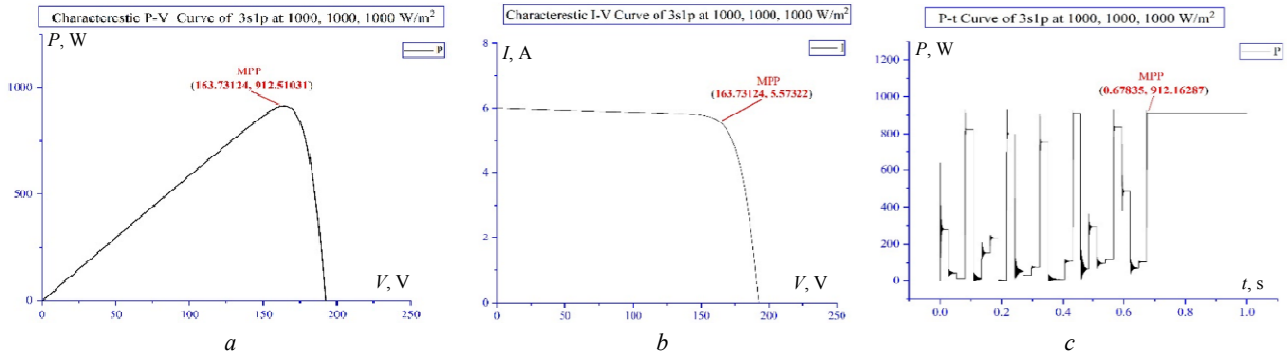

a *b* *c*

Fig. 14. 3s1p at irradiance of 1000, 1000, 1000 W/m^2:
(*a*) – characteristic P-V curve; (*b*) – characteristic I-V curve; (*c*) – power extracted using proposed method

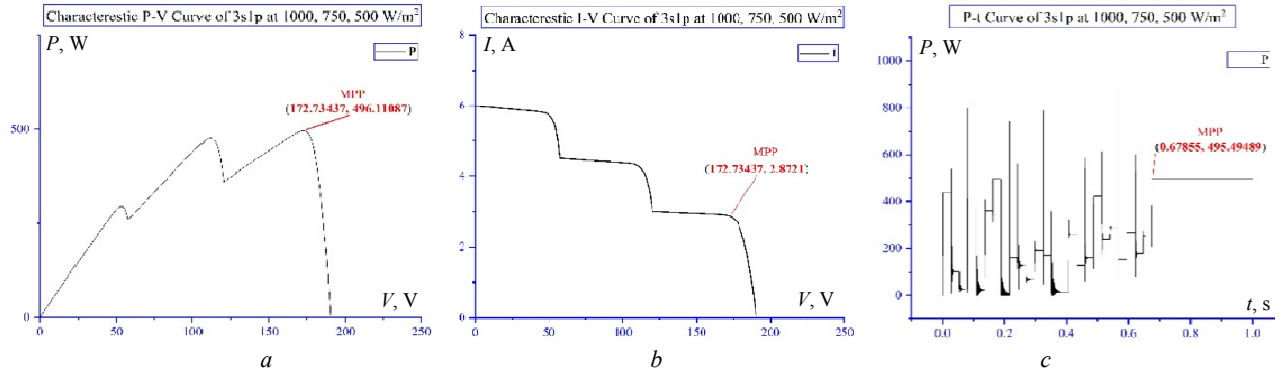

a *b* *c*

Fig. 15. 3s1p at irradiance of 1000, 750, 500 W/m^2:
(*a*) – characteristic P-V curve; (*b*) – characteristic I-V curve; (*c*) – power extracted using proposed method

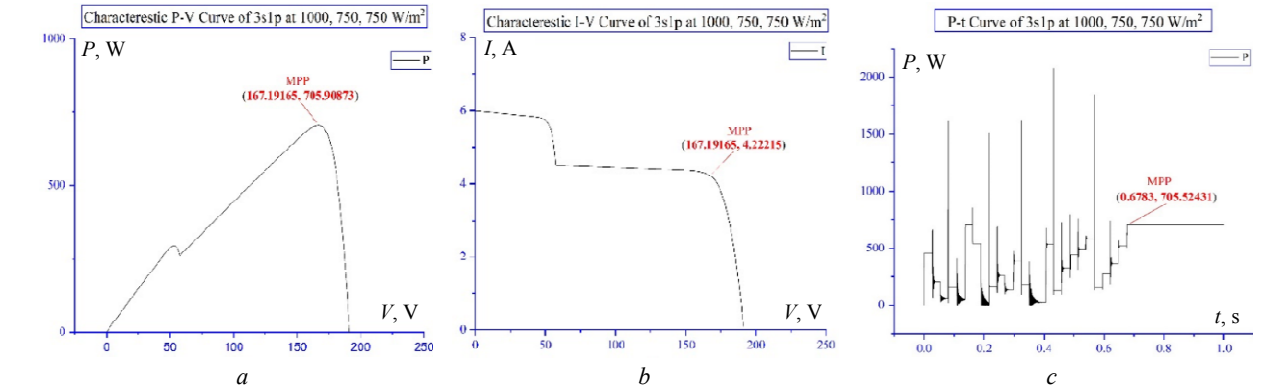

a *b* *c*

Fig. 16. 3s1p at irradiance of 1000, 750, 750 W/m^2:
(*a*) – characteristic P-V curve; (*b*) – characteristic I-V curve; (*c*) – power extracted using proposed method

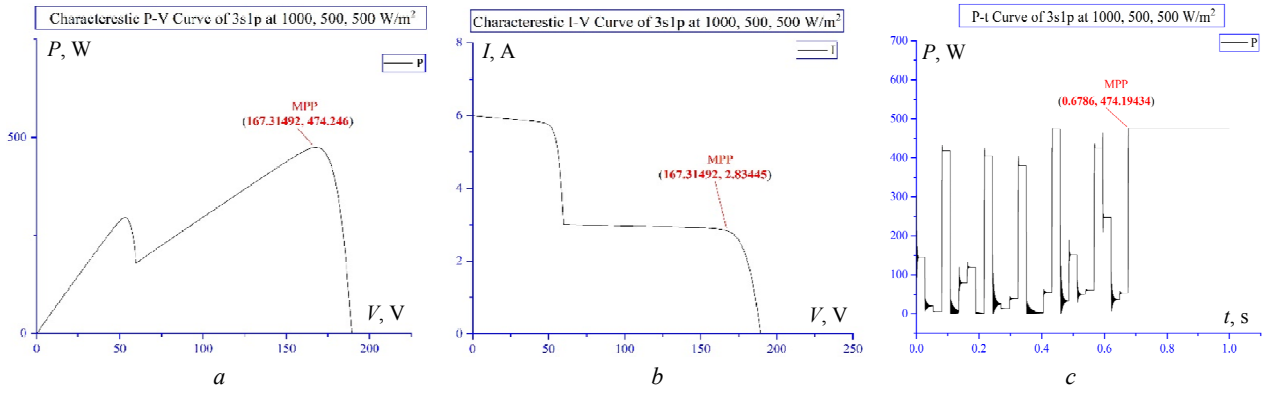

a *b* *c*

Fig. 17. 3s1p at irradiance of 1000, 500, 500 W/m^2:
(*a*) – characteristic P-V curve; (*b*) – characteristic I-V curve; (*c*) – power extracted using proposed method

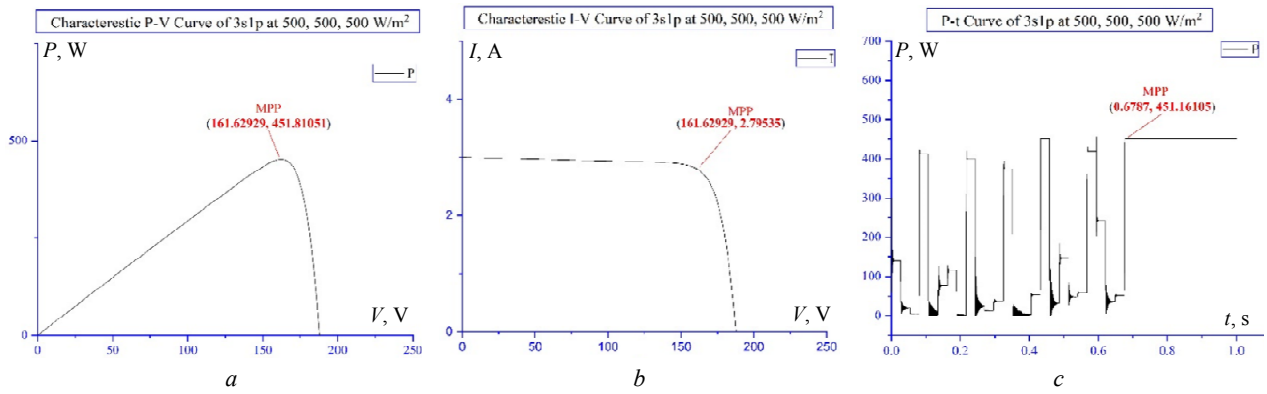

a *b* *c*

Fig. 18: 3s1p at irradiance of 500, 500, 500 W/m^2:
(*a*) – characteristic P-V curve; (*b*) – characteristic I-V curve; (*c*) – power extracted using proposed method

Comparison to other techniques. The most commonly used MPPT algorithms are P&O, HC, IC, PSO, GA, FPA, etc. The algorithms are effective for uniform and weak shading pattern but they fail to track MPP when shading is strong. The FPA-OBL is another technique used for strong shading that has very good MPP tracking ability. The proposed PPA also performs very good under all shading conditions. The simulation results have shown its effectiveness in all shadings. In Table 4 one can see that under strong shading conditions the efficiency of PPA has been 99.8 % that is the sign of its effectiveness. It is simple and has high MPP tracking and short tracking time. It doesn't have oscillations around MPP. The efficiency of PPA is 99 % in all the cases which makes it very effective and a good choice among other popular methods.

Table 5 shows the brief comparison of techniques.

Table 4

Detailed description of results for all configurations

Config.	Shading patterns, W/m^2	Rated power, W	Extracted power, W	*t*, s	Efficiency, %
1s1p	1000	300.882	300.880	0.6822	99.99
	500	148.775	148.675	0.6771	99.93
2s1p	1000, 1000	605.645	605.147	0.67725	99.91
	1000, 500	324.382	323.751	0.6771	99.80
	500, 500	301.273	301.043	0.67905	99.92
	200, 100	61.7493	61.2658	0.6892	99.21
3s1p	1000, 1000, 1000	912.510	912.162	0.67835	99.96
	1000, 750, 500	496.110	495.494	0.67855	99.87
	1000, 750, 750	705.908	705.524	0.6783	99.94
	1000, 500, 500	474.246	474.194	0.6786	99.98
	500, 500, 500	451.810	451.161	0.6787	99.85

Table 5

Comparison of Proposed technique with P&O, HC, IC and FPA

Algorithm	Oscillations at MPP	Falling to local maxima	Complexity
P&O	Yes	Yes	Complex
HC	Yes	Yes	Complex
IC	Yes	Yes	Complex
FPA	No	No	Less complex
SPPA	No	No	Less complex

5. Conclusions.

The paper presented a novel technique for maximum power point tracking that is based on the plant propagation technique.

The technique is effective in all type of shading conditions i.e., uniform, weak and strong.

It is a simple, less complex and fast converging technique with lesser number of parameters that has an edge of being easily computable technique as compared to its contemporary techniques.

The simulation studies are carried on MATLAB / Simulink and results are promising in all shading

conditions especially in strong shading conditions. The output efficiency is 99 % plus in all cases and has a tracking time less than 0.7 s in all cases.

Conflict of interest. The authors declare that they have no conflicts of interest.

REFERENCES

1. Bollipo R.B., Mikkili S., P. Bonthagorla K. Hybrid, optimal, intelligent and classical PV MPPT techniques: A review. *CSEE Journal of Power and Energy Systems*, 2021, vol. 7, no. 1, pp. 9-33. doi: https://doi.org/10.17775/cseejpes.2019.02720.

2. Li W., Zhang G., Pan T., Zhang Z., Geng Y., Wang J. A Lipschitz Optimization-Based MPPT Algorithm for Photovoltaic System Under Partial Shading Condition. *IEEE Access*, 2019, vol. 7, pp. 126323-126333. doi: https://doi.org/10.1109/ACCESS.2019.2939095.

3. Padmanaban S., Priyadarshi N., Sagar Bhaskar M., Holm-Nielsen J.B., Ramachandaramurthy V.K., Hossain E. A Hybrid ANFIS-ABC Based MPPT Controller for PV System With Anti-Islanding Grid Protection: Experimental Realization. *IEEE Access*, 2019, vol. 7, pp. 103377-103389. doi: https://doi.org/10.1109/ACCESS.2019.2931547.

4. Metry M., Balog R.S. An Adaptive Model Predictive Controller for Current Sensorless MPPT in PV Systems. *IEEE Open Journal of Power Electronics*, 2020, vol. 1, pp. 445-455. doi: https://doi.org/10.1109/OJPEL.2020.3026775.

5. Ali A., Almutairi K., Padmanaban S., Tirth V., Algarni S., Irshad K., Islam S., Zahir M.H., Shafiullah M., Malik M.Z. Investigation of MPPT Techniques Under Uniform and Non-Uniform Solar Irradiation Condition – A Retrospection. *IEEE Access*, 2020, vol. 8, pp. 127368-127392. doi: https://doi.org/10.1109/ACCESS.2020.3007710.

6. Abdel-Rahim O., Wang H. A new high gain DC-DC converter with model-predictive-control based MPPT technique for photovoltaic systems. *CPSS Transactions on Power Electronics and Applications*, 2020, vol. 5, no. 2, pp. 191-200. doi: https://doi.org/10.24295/CPSSTPEA.2020.00016.

7. Ghasemi M.A., Foroushani H.M., Parniani M. Partial Shading Detection and Smooth Maximum Power Point Tracking of PV Arrays Under PSC. *IEEE Transactions on Power Electronics*, 2016, vol. 31, no. 9, pp. 6281-6292. doi: https://doi.org/10.1109/TPEL.2015.2504515.

8. Huang C., Wang L., Yeung R.S., Zhang Z., Chung H.S., Bensoussan A. A Prediction Model-Guided Jaya Algorithm for the PV System Maximum Power Point Tracking. *IEEE Transactions on Sustainable Energy*, 2018, vol. 9, no. 1, pp. 45-55. doi: https://doi.org/10.1109/TSTE.2017.2714705.

9. Coelho R.F., Concer F.M., Martins D.C. A MPPT approach based on temperature measurements applied in PV systems. *2010 IEEE International Conference on Sustainable Energy Technologies (ICSET)*, 2010, pp. 1-6. doi: https://doi.org/10.1109/ICSET.2010.5684440.

10. Karami N., Moubayed N., Outbib R. General review and classification of different MPPT Techniques. *Renewable and Sustainable Energy Reviews*, 2017, vol. 68, pp. 1-18. doi: https://doi.org/10.1016/j.rser.2016.09.132.

11. Mei Q., Shan M., Liu L., Guerrero J.M. A Novel Improved Variable Step-Size Incremental-Resistance MPPT Method for PV Systems. *IEEE Transactions on Industrial Electronics*, 2011, vol. 58, no. 6, pp. 2427-2434. doi: https://doi.org/10.1109/TIE.2010.2064275.

12. Abdourraziq M.A., Maaroufi M., Ouassaid M. A new variable step size INC MPPT method for PV systems. *2014 International Conference on Multimedia Computing and Systems (ICMCS)*, 2014, pp. 1563-1568. doi: https://doi.org/10.1109/ICMCS.2014.6911212.

13. Pandey A., Dasgupta N., Mukerjee A.K. High-Performance Algorithms for Drift Avoidance and Fast Tracking in Solar MPPT System. *IEEE Transactions on Energy Conversion*, 2008, vol. 23, no. 2, pp. 681-689. doi: https://doi.org/10.1109/TEC.2007.914201.

14. Elgendy M.A., Zahawi B., Atkinson D.J. Assessment of Perturb and Observe MPPT Algorithm Implementation Techniques for PV Pumping Applications. *IEEE Transactions on Sustainable Energy*, 2012, vol. 3, no. 1, pp. 21-33. doi: https://doi.org/10.1109/TSTE.2011.2168245.

15. Mohd Zainuri M.A.A., Mohd Radzi M.A., Soh A.C., Rahim N.A. Development of adaptive perturb and observe-fuzzy control maximum power point tracking for photovoltaic boost DC–DC converter. *IET Renewable Power Generation*, 2014, vol. 8, no. 2, pp. 183-194. doi: https://doi.org/10.1049/iet-rpg.2012.0362.

16. Elgendy M.A., Zahawi B., Atkinson D.J. Comparison of Directly Connected and Constant Voltage Controlled Photovoltaic Pumping Systems. *IEEE Transactions on Sustainable Energy*, 2010, vol. 1, no. 3, pp. 184-192. doi: https://doi.org/10.1109/TSTE.2010.2052936.

17. Samrat P.S., Edwin F.F., Xiao W. Review of current sensorless maximum power point tracking technologies for photovoltaic power systems. *2013 International Conference on Renewable Energy Research and Applications (ICRERA)*, 2013, pp. 862-867. doi: https://doi.org/10.1109/ICRERA.2013.6749872.

18. Kumar N., Hussain I., Singh B., Panigrahi B.K. Framework of Maximum Power Extraction From Solar PV Panel Using Self Predictive Perturb and Observe Algorithm. *IEEE Transactions on Sustainable Energy*, 2018, vol. 9, no. 2, pp. 895-903. doi: https://doi.org/10.1109/TSTE.2017.2764266.

19. Elgendy M.A., Atkinson D.J., Zahawi B. Experimental investigation of the incremental conductance maximum power point tracking algorithm at high perturbation rates. *IET Renewable Power Generation*, 2016, vol. 10, no. 2, pp. 133-139. doi: https://doi.org/10.1049/iet-rpg.2015.0132.

20. Boukenoui R., Bradai R., Mellit A., Ghanes M., Salhi H. Comparative analysis of P&O, modified hill climbing-FLC, and adaptive P&O-FLC MPPTs for microgrid standalone PV system. *2015 International Conference on Renewable Energy Research and Applications (ICRERA)*, 2015, pp. 1095-1099. doi: https://doi.org/10.1109/ICRERA.2015.7418579.

21. Jain S., Agarwal V. A new algorithm for rapid tracking of approximate maximum power point in photovoltaic systems. *IEEE Power Electronics Letters*, 2004, vol. 2, no. 1, pp. 16-19. doi: https://doi.org/10.1109/LPEL.2004.828444.

22. Tsang K.M., Chan W.L. Maximum power point tracking for PV systems under partial shading conditions using current sweeping. *Energy Conversion and Management*, 2015, vol. 93, pp. 249-258. doi: https://doi.org/10.1016/j.enconman.2015.01.029.

23. Anoop K., Nandakumar M. A novel maximum power point tracking method based on particle swarm optimization combined with one cycle control. *2018 International Conference on Power, Instrumentation, Control and Computing (PICC)*, 2018, pp. 1-6. doi: https://doi.org/10.1109/PICC.2018.8384777.

24. Leedy A.W., Garcia K.E. Approximation of P-V characteristic curves for use in maximum power point tracking algorithms. *45th Southeastern Symposium on System Theory*, 2013, pp. 88-93. doi: https://doi.org/10.1109/SSST.2013.6524945.

25. Chandra S., Gaur P., Srishti. Maximum Power Point Tracking Approaches for Wind-Solar Hybrid Renewable Energy System – A Review. In: Singh S., Wen F., Jain M. (eds) *Advances in Energy and Power Systems. Lecture Notes in Electrical Engineering*, 2018, vol. 508. Springer, Singapore. doi: https://doi.org/10.1007/978-981-13-0662-4_1.

26. Esram T., Chapman P.L. Comparison of Photovoltaic Array Maximum Power Point Tracking Techniques. *IEEE*

Transactions on Energy Conversion, 2007, vol. 22, no. 2, pp. 439-449. doi: https://doi.org/10.1109/TEC.2006.874230.
27. Shmilovitz D. On the control of photovoltaic maximum power point tracker via output parameters. *IEE Proceedings: Electric Power Applications*, 2005, vol. 152, no. 2, pp. 239-248. doi: https://doi.org/10.1049/ip-epa:20040978.
28. Shabaan S., Abu El-Sebah M.I., Bekhit P. Maximum power point tracking for photovoltaic solar pump based on ANFIS tuning system. *Journal of Electrical Systems and Information Technology*, 2018, vol. 5, no. 1, pp. 11-22. doi: https://doi.org/10.1016/j.jesit.2018.02.002.
29. Sundareswaran K., Vigneshkumar V., Palani S. Development of a hybrid genetic algorithm/perturb and observe algorithm for maximum power point tracking in photovoltaic systems under non-uniform insolation. *IET Renewable Power Generation*, 2015, vol. 9, no. 7, pp. 757-765. doi: https://doi.org/10.1049/iet-rpg.2014.0333.
30. Manickam C., Raman G.R., Raman G.P., Ganesan S.I., Nagamani C. A Hybrid Algorithm for Tracking of GMPP Based on P&O and PSO With Reduced Power Oscillation in String Inverters. *IEEE Transactions on Industrial Electronics*, 2016, vol. 63, no. 10, pp. 6097-6106. doi: https://doi.org/10.1109/TIE.2016.2590382.
31. Abdulkadir M., Yatim A.H.M. Hybrid maximum power point tracking technique based on PSO and incremental conductance. *2014 IEEE Conference on Energy Conversion (CENCON)*, 2014, pp. 271-276. doi: https://doi.org/10.1109/CENCON.2014.6967514.
32. Eltamaly A.M., Farh H.M.H. Dynamic global maximum power point tracking of the PV systems under variant partial shading using hybrid GWO-FLC. *Solar Energy*, 2019, vol. 177, pp. 306-316. doi: https://doi.org/10.1016/j.solener.2018.11.028.
33. Lasheen M., Abdel-Salam M. Maximum power point tracking using Hill Climbing and ANFIS techniques for PV applications: A review and a novel hybrid approach. *Energy Conversion and Management*, 2018, vol. 171, pp. 1002-1019. doi: https://doi.org/10.1016/j.enconman.2018.06.003.
34. Alajmi B.N., Ahmed K.H., Finney S.J., Williams B.W. Fuzzy-Logic-Control Approach of a Modified Hill-Climbing Method for Maximum Power Point in Microgrid Standalone Photovoltaic System. *IEEE Transactions on Power Electronics*, 2011, vol. 26, no. 4, pp. 1022-1030. doi: https://doi.org/10.1109/TPEL.2010.2090903.
35. Sher H.A., Murtaza A.F., Noman A., Addoweesh K.E., Al-Haddad K., Chiaberge M. A New Sensorless Hybrid MPPT Algorithm Based on Fractional Short-Circuit Current Measurement and P&O MPPT. *IEEE Transactions on Sustainable Energy*, 2015, vol. 6, no. 4, pp. 1426-1434. doi: https://doi.org/10.1109/TSTE.2015.2438781.
36. Ali A., Li W., He X. Performance Analysis of Incremental Conductance MPPT with Simple Moving Voltage Average Method for Distributed PV System. *The Open Electrical & Electronic Engineering Journal*, 2016, vol. 10, no. 1, pp. 118-128. doi: https://doi.org/10.2174/1874129001610010118.
37. Shang L., Zhu W., Li P., Guo H. Maximum power point tracking of PV system under partial shading conditions through flower pollination algorithm. *Protection and Control of Modern Power Systems*, 2018, vol. 3, no. 1, art. no. 38. doi: https://doi.org/10.1186/s41601-018-0111-3.
38. Awan K.S., Mahmood T., Shorfuzzaman M., Ali R., Mehmood R.M. A Machine Learning Based Algorithm to Process Partial Shading Effects in PV Arrays. *Computers, Materials & Continua*, 2021, vol. 68, no. 1, pp. 29-43. doi: https://doi.org/10.32604/cmc.2021.014824.
39. Salhi A., Fraga E.S. Nature-Inspired Optimisation Approaches and the New Plant Propagation Algorithm. *Proceedings of the International Conference on Numerical Analysis and Optimization (ICeMATH '11)*, Yogyakarta, Indonesia. 2011. Available at: http://repository.essex.ac.uk/9974/ (accessed 26 May 2021).
40. Gilroy S., Masson P.H. *Plant Tropisms, 1st ed*. Blackwell Publisher, Ames, IA, USA, 2008. Available at: https://www.cell.com/current-biology/pdf/S0960-9822(08)00179-6.pdf (accessed 26 May 2021).

Received 03.09.2021
Accepted 31.10.2021
Published 03.12.2021

Shayan Ali Khan[1], *MSc Student,*
Tahir Mahmood[1], *Professor,*
Kamran Sadiq Awan[2], *PhD Student,*
[1] Department of Electrical Engineering,
University of Engineering and Technology,
Taxila 47050, Pakistan,
e-mail: shayan.alikhan@yahoo.com,
tahir.mehmood@uettaxila.edu.pk
[2] Department of Electrical & Electronic Engineering,
Newcastle University,
NE1 7RU, Newcastle Upon Tyne, United Kingdom,
e-mail: k.s.awan2@newcastle.ac.uk (Corresponding author)

How to cite this article:
Khan S.A., Mahmood T., Awan K.S. A nature based novel maximum power point tracking algorithm for partial shading conditions. *Electrical Engineering & Electromechanics*, 2021, no. 6, pp. 54-63. doi: https://doi.org/10.20998/2074-272X.2021.6.08.

UDC 621.31 https://doi.org/10.20998/2074-272X.2021.6.09

Z.E.Z. Laggoun, H. Benalla, K. Nebti

A power quality enhanced for the wind turbine with sensorless direct power control under different input voltage conditions

Introduction. *The quality of electrical energy is essential during disturbances, at the level of power electronic devices will suffer serious operating problems causing dangerous damage.* ***Aim.*** *A new approach to direct power control without grid voltage sensor improves the quality and control of instantaneous active and reactive power converters.* ***Methodology.*** *First, the technique without network voltage sensor with a direct power control based on a switching table, which is a classic approach, is discussed and its performance is analyzed under increasing and decreasing load. In addition, the performance of the proposed technique is also analyzed under the same circumstances and their performance is compared.* ***Originality.*** *The new method consists of a nonlinear grid voltage modulated controller and a conventional controller which guarantees very good results in a polluted network. The proposed method is verified using MATLAB/Simulink.* ***Results.*** *The simulation results under different input voltage conditions show that the proposed method not only has good tracking performance in active and reactive power, but also reduces the current total harmonic distortion to 1.9 %, which is good lower than the requirement for network operation.* References 17, tables 2, figures 11.
Key words: **direct power control, virtual flux, grid voltage modulated, constant switching frequency.**

Вступ. *Якість електроенергії має важливе значення під час збоїв, на рівні силових електронних пристроїв будуть мати місце серйозні проблеми експлуатації, що викликають небезпечні пошкодження.* ***Мета***. *Новий підхід до прямого керування потужністю без датчика напруги мережі покращує якість та контроль перетворювачів миттєвої активної та реактивної потужності.* ***Методологія***. *Спочатку обговорюється методика без датчика напруги мережі з прямим керуванням потужністю на основі таблиці перемикання, що є класичним підходом, та аналізується його продуктивність при збільшенні та зменшенні навантаження. Крім того, ефективність запропонованої методики також аналізується за тих же обставин, і їхня продуктивність порівнюється.* ***Оригінальність***. *Новий метод складається з нелінійного мережевого контролера з модуляцією напруги і звичайного контролера, який гарантує дуже хороші результати в забрудненій мережі. Запропонований метод перевіряється за допомогою MATLAB/Simulink.* ***Результати***. *Результати моделювання за різних умов вхідної напруги показують, що запропонований метод не тільки має хороші характеристики відстеження активної та реактивної потужності, але також знижує поточний THD до 1,9 %, що значно нижче, ніж вимоги для роботи мережі.*. Бібл. 17, табл. 2, рис. 11.
Ключові слова: **пряме керування потужністю, віртуальний потік, модуляція напруги мережі, постійна частота перемикання.**

1. Introduction. Grid-connected converters are widely used in the application of smart grids, Flexible Alternating Current Transmission Systems (FACTS) and renewable energy sources (e.g., wind and solar) and various control methods have been investigated so that converters improve their performance [1].

Many studies have focused on the advanced control of the functioning of renewable energies that have been proposed with the same main objective which is the power quality which focuses on an almost sinusoidal input current waveform with a higher power factor and regardless of the input condition whether balanced or distorted but their different principles.

The instantaneous power theory proposed by Japanese researchers [2] is inspired by the Direct Torque Control (DTC) proposed for asynchronous motors [3]. The Direct Power Control (DPC) strategy has received a lot of attention from researchers in recent years due to its many benefits. They have shown that the use of DPC in various converters and applications whether it be matrix [4] or Voltage Source Converter (VSC) at two and three levels based on Fuzzy-Q-Learning algorithm is applied [5] or on active filters [6] is more advantageous.

A DPC switching table has been formulated in which the appropriate switching states are selected from a predefined optimal switching table based on the digitized signals of the instantaneous errors between the commanded and estimated values of active and reactive power extracted by a hysteresis controller and the angular position of the voltage at the terminals of the converter thus guarantees a decoupled control of the powers and good dynamic performance [7].

However, the varying switching frequency results in broadband harmonic spectra, which complicates the design of line filters. To solve the downshift associated with variable frequency operation, various DPC algorithms have been developed for constant switching frequency. One can find various publications studies on how to fix the switching frequency of the DPC. The authors [8] suggest to associate the principle of the DPC with a vector modulation Space Vector Modulation (SVM) in order to obtain a switching frequency constant without the use of a switching table. Other authors [9] combine other technique with DPC to improve the result even more by using Sliding-Mode Control (SMC) it allows to obtain a stabilization response faster than that of the PI controller and a greater robustness. Backstepping improves transient performance [10]. The SVM modulation based on a predictive controller was developed in [11] and even the new method proposed by [12], called Multiple Switching Tables (MST-DPC), performs a real-time selection of the most suitable switching table among four alternatives depending on the operating conditions of the device.

The performance of conventional DPC under unbalanced and/or distorted input voltages deteriorates when this occurs. In recent years, researchers are increasingly interested in control methods to improve the performance of DPC strategies under unbalanced grid voltage conditions. Most solutions to improve the performance of three-phase Pulse Width Modulation (PWM) rectifiers are based on the extraction of the

positive/negative voltage/current sequences. These solutions are complicated and difficult to implement for real-time applications since they require a great deal of computation.

In Virtual Flux-based (VF) methods, the VF space vector is obtained by integrating the voltage space vector. The use of a pure integrator induces a shift of the direct current in the estimated VF in order to remedy this drawback. Several methods of practical implementation of VF estimation have been proposed, with the aim of avoiding saturation of the estimated signals. This integration is generally performed via a First Order Low Pass (FLOP) filter to avoid the saturation and DC drift problems associated with pure integrators [13]. The DPC Control Based Virtual Flux (VF-DPC) uses the detected AC line currents and the estimated VF to calculate the input powers. However, FLOP filters lead to amplitude and phase errors. Although these errors can be minimized by reducing the cut-off frequency of the filter, this reduction leads to a reduction in the passband of the filter and therefore to a degradation of its dynamics. And for that, the authors [14, 15] propose a second order generalized integrator (SOGI) estimator exploiting the concept of virtual flow. Recent research in [16] presents a combination of two cascade filters to achieve a VF-based timing scheme, to ensure that the gate currents emulate the desirable sine waveform even when the supply voltage is unbalanced and/or harmonized.

Although the Grid Voltage Modulated Direct Power Control (GVM-DPC) is first introduced in [17], the main contribution of this paper is the proposal for an improvement in the technique using VF incorporated in a DPC scheme (GVM-DPC), for a three-phase PWM rectifier in our case. The results of the simulation of VF-GVM-DPC are compared with GVM-DPC under a polluted network which gives better performance than the classical method. The VF algorithm has an open loop structure and uses the fundamental orthogonal output signals which are obtained directly from the estimation of the fundamental active and reactive powers. This method provides quasi-sinusoidal input current waveform under different input voltage condition and achieves good stability, improves the performance of GVM-DPC.

The goal of the paper is the mathematical analysis and the numerical implementation of an improved method of grid voltage modulated based on direct power control for three phase pulse width modulation rectifiers.

The rest of the paper is organized as follows. In Section 2 the system modeling and the design of the GVM-DPC controls are presented. Section 3 shows the simulation results using MATLAB/Simulink. Finally, conclusions are given in the last Section 4.

2. Virtual flux grid voltage modulated direct power control.

2.1. Modeling VSC.

Figure 1 shows a simplified circuit of a two-level VSC connected to the grid with an LR filter all of these are considered ideal switches. The DC side could be connected to renewable energy sources or energy storage systems with a capacitor C and even at transmission scale High Voltage DC.

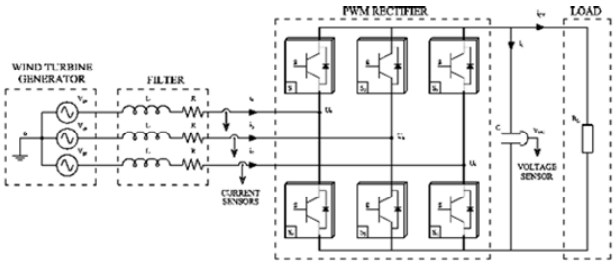

Fig. 1. Representation of a VSC connected to wind turbine generator

The relationship among the VSC output voltages, the grid voltages, and the output currents in the stationary reference frame by using the Clark transformation can be expressed as:

$$\begin{cases} U_\alpha = R \cdot i_\alpha + L \cdot \dfrac{\mathrm{d}i_\alpha}{\mathrm{d}t} + V_{g\alpha}; \\ U_\beta = R \cdot i_\beta + L \cdot \dfrac{\mathrm{d}i_\beta}{\mathrm{d}t} + V_{g\beta}, \end{cases} \quad (1)$$

where U_α and U_β indicate the VSC output voltage; i_α and i_β indicate the output currents; $V_{g\alpha}$ and $V_{g\beta}$ indicate the grid voltage in $\alpha\beta$ frame, and L and R are the filter inductance and resistance, respectively.

2.2. Modeling VF.

The concept of VF is based on the voltage integral and can be applied as an estimation method for voltage-sensor-less control of VSCs:

$$\Psi_{\alpha\beta} = \int U_{\alpha\beta}\mathrm{d}t = \int \left(R \cdot i_{\alpha\beta} + L \cdot \frac{\mathrm{d}i_{\alpha\beta}}{\mathrm{d}t} + V_{g\alpha\beta} \right) \mathrm{d}t \,, \quad (2)$$

where $\Psi_{\alpha\beta}$ is the estimated VF.

The use of the proposed Dual Virtual Flux Phase Locked Loop (DVF-PLL), based on the cascade of two adaptive filters illustrated in Fig. 2, is an optimized solution.

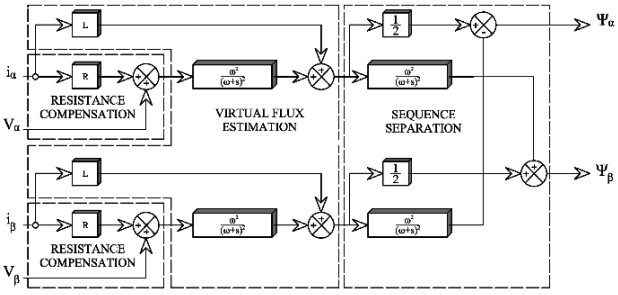

Fig. 2. The diagram of the proposed Dual Virtual Flux estimator

The DVF-PLL filter function is based on the estimated voltage and measurements current. First, the voltage reference signals are expressed in the stationary reference frame ($\alpha\beta$). Then the resistive voltage drop included in the model is subtracted. The latter is shifted in phase (90°) and gains unity for the fundamental frequency used to estimate the VF components with the second-order-low-pass filters. The estimated components of the VF are separated in positive and negative sequences with the same transfer function as that used for the estimation of the VF components. By using the estimated VF components in the stationary reference frame, the flux angles can be estimated by using a conventional PLL. The cutoff frequency is equal to 50 Hz and only the positive

sequence is used to ensure adequate operation under faulty network conditions [16].

2.3 Fuzzy Controller for PLL. To have good PLL control performance, especially in case of voltage disturbance variation and load disturbance the PI controller will be replaced by a fuzzy controller. The schematic diagram of this control is given in Fig. 3.

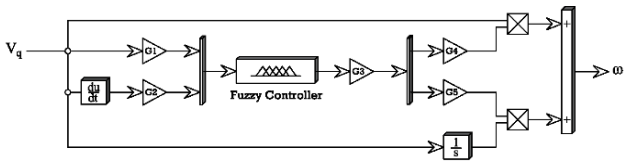

Fig. 3. The PLL fuzzy control

The fuzzy regulator uses two inputs. He first input is the error between the reference and the measured value of the quadratic voltage V_q. The second one represents the variation of this error.

These two signals are expressed by:

$$\begin{cases} e = V_{qref}(n) - V_q(n); \\ \Delta e = e(n) - e(n-1), \end{cases} \quad (3)$$

where e and Δe are the error of the quadratic voltage and its variation of the error.

For fuzzification, we used triangular membership functions for the error. We chose the seven fuzzy sets: NL (negative large), NM (negative middle), NS (negative small), ZE (zero), PS (positive small), PM (positive middle), PL (positive large). The rate of change $\Delta E\omega$ includes 3 fuzzy subsets, it is not necessary to subdivide it, because it is changing quickly in DPC. Output membership KP and KI, both contain four fuzzy subsets as shown in Fig. 4. There are total of 21 rules as listed in Table 1.

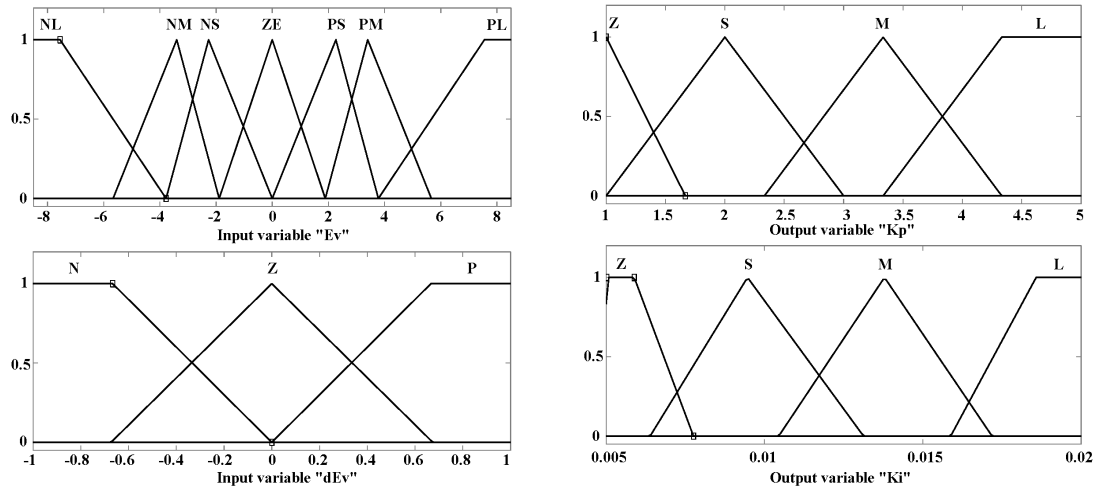

a *b*

Fig. 4. The fuzzy membership functions of input (*a*) and output (*b*) variables

Table 1

Fuzzy rules

KP / KI		$E\omega$						
		NL	NM	NS	ZE	PS	PM	PL
ΔE	N	L	M	S	M	S	M	L
		Z	S	M	L	M	S	Z
ΔE	Z	L	M	L	Z	L	M	L
		Z	S	M	L	M	S	Z
ΔE	P	L	M	L	Z	L	M	L
		Z	M	L	L	L	M	Z

2.4 Modeling DPC. Line current and VF components are used in power calculations. It should be noted that electrical resistance is included in the estimation process VF, they can be calculated by the following expressions:

$$\begin{cases} P = \omega \cdot (\Psi_\alpha \cdot i_\beta - \Psi_\beta \cdot i_\alpha), \\ Q = \omega \cdot (\Psi_\alpha \cdot i_\alpha + \Psi_\beta \cdot i_\beta), \end{cases} \quad (4)$$

where P is the estimate active power; Q is the estimate reactive power; ω is the angular frequency of the grid fundamental wave; Ψ_α, Ψ_β, i_α, i_β are respectively the virtual flow and the currents in the reference $\alpha\beta$.

By deriving (3) with respect to time, instantaneous variations in active and reactive power dP/dt and dQ/dt respectively can be expressed as a function of variations in network voltage and output current as follows:

$$\begin{cases} \dfrac{dP}{dt} = i_\beta \cdot \dfrac{d\Psi_\alpha}{dt} + \Psi_\alpha \cdot \dfrac{di_\beta}{dt} - i_\alpha \cdot \dfrac{d\Psi_\beta}{dt} - \Psi_\beta \cdot \dfrac{di_\alpha}{dt}; \\ \dfrac{dQ}{dt} = i_\alpha \cdot \dfrac{d\Psi_\alpha}{dt} + \Psi_\alpha \cdot \dfrac{di_\beta}{dt} + i_\beta \cdot \dfrac{d\Psi_\beta}{dt} - \Psi_\beta \cdot \dfrac{di_\beta}{dt}. \end{cases} \quad (5)$$

If we consider a non-distorted grid, the following relationship could be obtained

$$\begin{cases} \dfrac{d\Psi_\alpha}{dt} = -\omega \cdot \Psi_\beta; \\ \dfrac{d\Psi_\beta}{dt} = \omega \cdot \Psi_\alpha, \end{cases} \quad (6)$$

where $\omega = 2 \cdot \pi \cdot f$ is the angular frequency of the grid voltage and f is the frequency of the grid voltage.

By substituting (4) in (5), the state-space model of the active and reactive powers is obtained as follows:

$$\begin{cases} \dfrac{dP}{dt} = -\dfrac{R}{L} \cdot P - \omega \cdot Q + \dfrac{1}{L} \cdot \left(\omega \cdot (\Psi_\alpha \cdot U_\beta + \Psi_\beta \cdot U_\alpha) - \Psi_g^2\right), \\ \dfrac{dQ}{dt} = \omega \cdot P - \dfrac{R}{L} \cdot Q + \dfrac{\omega}{L} \cdot (\Psi_\alpha \cdot U_\beta + \Psi_\beta \cdot U_\alpha), \end{cases} \quad (7)$$

where

$$\Psi_g^2 = \omega^2 \cdot \left(\Psi_\alpha^2 + \Psi_\beta^2\right)$$

2.5 Grid voltage modulated direct power control. As mentioned in point (6), our main idea is to decouple the outputs from the inputs. The definition of the control inputs of the GVM is given as follows:

$$\begin{cases} \upsilon_P = \omega \cdot \left(\Psi_\alpha \cdot U_\beta - \Psi_\beta \cdot U_\alpha\right); \\ \upsilon_Q = \omega \cdot \left(\Psi_\alpha \cdot U_\alpha + \Psi_\beta \cdot U_\beta\right) \end{cases} \tag{8}$$

The space-state model of the active and reactive powers becomes again as follows:

$$\begin{cases} \dfrac{\mathrm{d}P}{\mathrm{d}t} = -\dfrac{R}{L} \cdot P - \omega \cdot Q + \dfrac{1}{L} \cdot \left(\upsilon_P - \Psi_g^2\right); \\ \dfrac{\mathrm{d}Q}{\mathrm{d}t} = \omega \cdot P - \dfrac{R}{L} \cdot Q + \dfrac{1}{L} \cdot \upsilon_Q. \end{cases} \tag{9}$$

A controller is designed to let the active and reactive powers track their references. Define errors of the active and reactive powers as follows:

$$\begin{cases} e_P = P_{ref} - P; \\ e_Q = Q_{ref} - Q, \end{cases} \tag{10}$$

where P_{ref} and Q_{ref} are the active and reactive power references, respectively.

$$\begin{cases} U_P = \underbrace{\Psi_g^2 + R \cdot P + L \cdot \omega \cdot Q}_{Feedforward} + \underbrace{L \cdot \upsilon_P}_{Feedback}; \\ U_Q = \underbrace{-\omega \cdot L \cdot P + R \cdot Q}_{Feedforward} + \underbrace{L \cdot \upsilon_Q}_{Feedback}, \end{cases} \tag{11}$$

where U_P and U_Q are the new control inputs; υ_P and υ_Q are the feedback control inputs.

If the feedback control inputs are designed as follows:

$$\begin{cases} \upsilon_P = \dot{P}_{ref} + K_P \cdot e_P + K_P \cdot \int_0^t \dot{e}_P(t)\mathrm{d}t + K_P \cdot \mathrm{sgn}(e_P); \\ \upsilon_Q = \dot{Q}_{ref} + K_Q \cdot e_Q + K_Q \cdot \int_0^t \dot{e}_Q(t)\mathrm{d}t + K_Q \cdot \mathrm{sgn}(e_Q), \end{cases} \tag{12}$$

where υ_P and υ_Q are the new control inputs; K_P and K_Q are controller gains.

If we consider a non-distorted grid, the following relationship could be obtained

$$\begin{bmatrix} \Psi_{\alpha-1}(t) \\ \Psi_{\beta-1}(t) \end{bmatrix} = \begin{bmatrix} \Psi_1 \cdot \sin(\omega_1 \cdot t + \theta_1) \\ \Psi_1 \cdot \cos(\omega_1 \cdot t + \theta_1) \end{bmatrix} + \begin{bmatrix} A_0 \\ B_0 \end{bmatrix} + Z, \tag{13}$$

with

$$Z = \sum_{n=2}^{\infty} \begin{bmatrix} \Psi_n \cdot \sin(\omega_n \cdot t + \theta_n) \\ \Psi_n \cdot \cos(\omega_n \cdot t + \theta_n) \end{bmatrix},$$

where Ψ_n is the magnitude of the n^{th} term; ω_n its pulsation; θ_n its initial phase; A_0 and B_0 are, respectively, the DC offsets of $\Psi_{\alpha-i}$ and $\Psi_{\beta-i}$; Ψ_1 is the magnitude of fundamental components of the $\Psi_{\alpha i}$ and $\Psi_{\beta i}$.

While the fundamental VF value is expressed as follows:

$$\begin{bmatrix} \Psi_\alpha(t) \\ \Psi_\beta(t) \end{bmatrix} = \begin{bmatrix} \Psi_1 \cdot \sin(\omega_1 \cdot t + \theta_1) \\ \Psi_1 \cdot \cos(\omega_1 \cdot t + \theta_1) \end{bmatrix}, \tag{14}$$

where Ψ_1, ω_1 and θ_1 is the magnitude components, pulsation and initial phase of fundamental.

Based on the grid voltage (13), the GVM inputs can be represented as follows:

$$\begin{bmatrix} U_P \\ U_Q \end{bmatrix} = \Psi_g \begin{bmatrix} \sin(\omega \cdot t + \theta_1) & -\cos(\omega \cdot t + \theta_1) \\ \cos(\omega \cdot t + \theta_1) & \sin(\omega \cdot t + \theta_1) \end{bmatrix} \begin{bmatrix} \Psi_\alpha \\ \Psi_\beta \end{bmatrix}. \tag{15}$$

The original control inputs can be calculated as follows:

$$\begin{cases} U_\alpha = \dfrac{\Psi_\alpha \cdot U_P - \Psi_\beta \cdot U_Q}{\Psi_g^2}; \\ U_\beta = \dfrac{\Psi_\beta \cdot U_P - \Psi_\alpha \cdot U_Q}{\Psi_g^2}. \end{cases} \tag{16}$$

Figure 5 shows the block diagram of the proposed method.

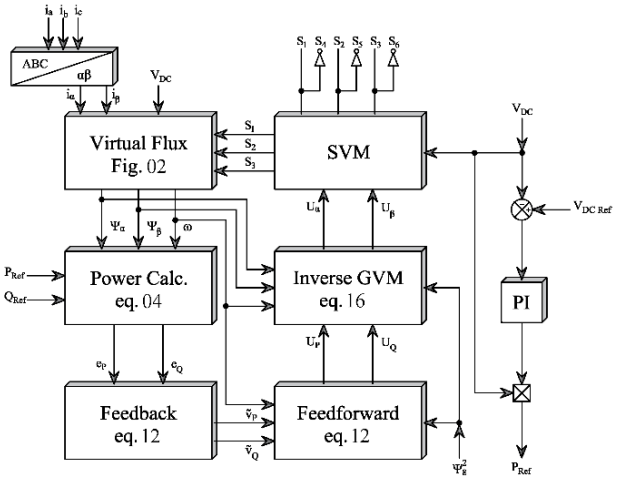

Fig. 5. Structure of VF-GVM-DPC controller

3. Simulation results. In order to provide a complete comparison work, the classical control and the proposed method are exposed to disturbed voltages which are implemented with the help of MATLAB / Simulink software. In a first step, a voltage unbalance and injection of the 7th order harmonic are created and included in phase A at a cost of 20 %. Then, harmonics 5 and 7 with an amplitude of 20 % is applied. A voltage unbalance of 20 % and a 5th order harmonic of 20 % are created and included in phase A. Finally, which is the worst case that can occur with mains voltages, an asymmetrical disturbance with harmonics 5 and 7 with an amplitude of 20 % is applied. We define the power fluctuation and the total harmonic distortion (THD) factor of input current as comparative criteria to demonstrate the superiority of the proposed strategy using simulation results. During all simulations, the Q_{ref} is kept at zero to ensure the functioning of the Unit Power Factor, which is an indispensable criterion.

The two compared methods are simulated under conditions shown in Fig. 6.

The following simulation results are obtained using the values of the parameters given in Table 2.

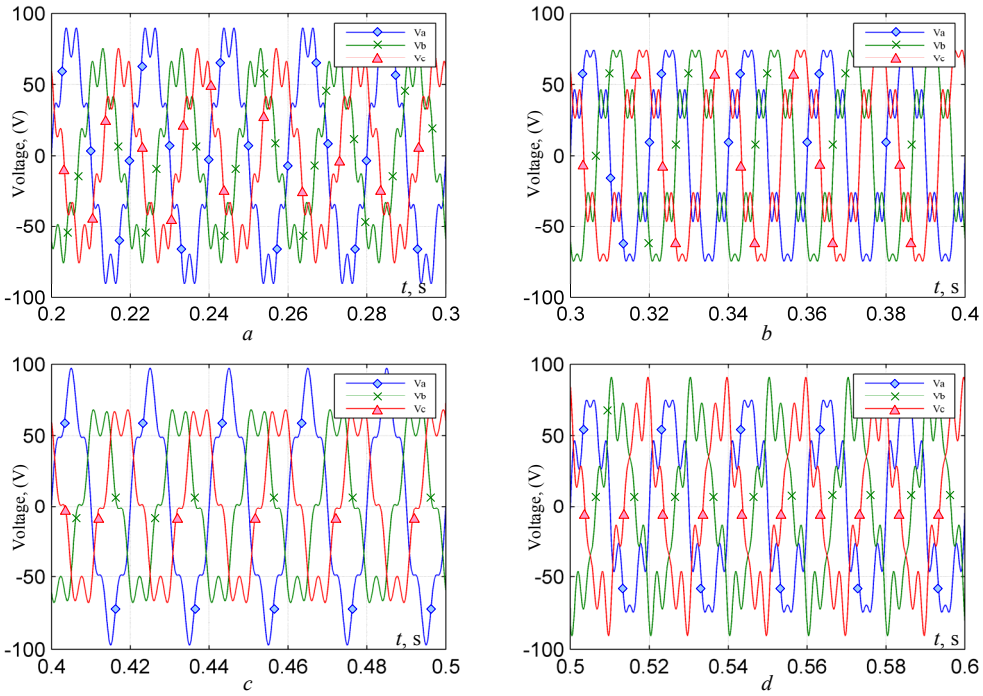

Fig. 6. The different voltage source condition applied to the rectifier:
(*a*) – unbalanced and harmonic 7 to 20 %; (*b*) – harmonic 5 and 7 to 20 %;
(*c*) – unbalanced and harmonic 5 to 20 %; (*d*) – harmonic 5 and 7 to 20 % asymmetric;

Table 2

System parameters used in simulation

Parameters	Symbol	Values	Parameters	Symbol	Values	Parameters	Symbol	Values
The resistance of reactors	R	0.56 Ω	DC-bus capacitor	C	1100 μF	Switching frequency	F_{sw}	7500 Hz
Load resistance	RL	68.6 Ω	The line-to-line AC voltage	E	85 V	DC-bus voltage	VDC	180 V
Inductance of reactors	L	19.5 mH	Frequency	F	50 Hz	Sampling period	T_S	20 μs

Figure 7 shows the results for GVM-DPC:

- (*a*) – the bus voltage curve;
- (*b*) – the grid current;
- (*c*) – the estimated voltages $U_{\alpha\beta}$;
- (*d*) – the superimposition current *i* and voltage *V* in phase A;
- (*e*) – the active *P* and reactive *Q* powers.

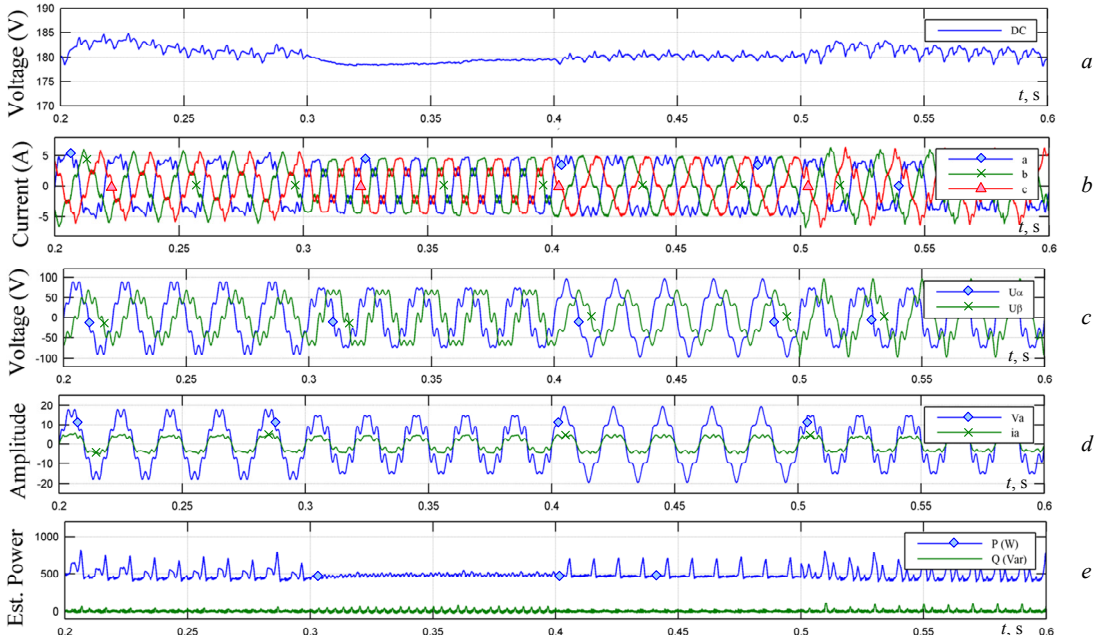

Fig. 7. The simulation results GVM-DPC

Figure 8 shows the results for VF-GVM-DPC:

- (*a*) – the bus voltage curve;
- (*b*) – the grid current;
- (*c*) – the estimated virtual flux $\Psi_{\alpha\beta}$;
- (*d*) – the superposition current *i* and the voltage *V* in phase A;
- (*e*) – the active *P* and reactive *Q* powers.

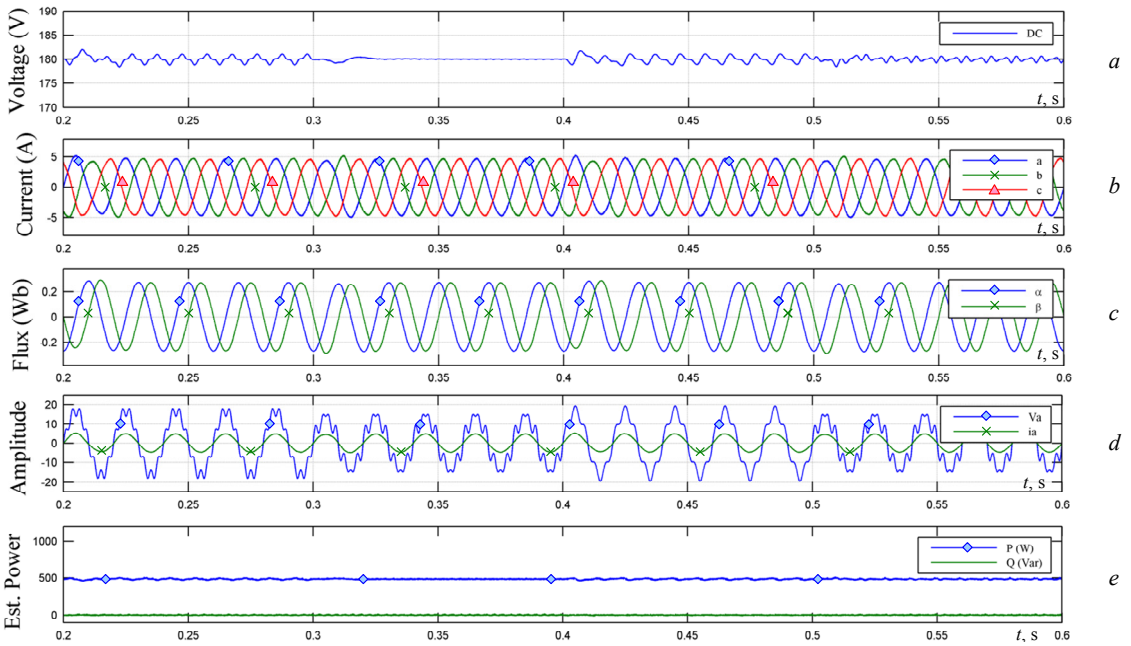

Fig. 8. The simulation result VF-GVM-DPC

The distribution of Fig. 7 is the same as that of Fig. 8. We can see in Fig. 7 the GVM-DPC which leads to fluctuations in the voltage curve of the bus. In addition, the grid current is affected by disturbed grid voltage conditions, with a high THD rate, which reduces the accuracy of the estimates of active and reactive power as can be seen in Fig. 7. In addition, the DC bus seriously oscillates around 5 V and the system does not operate under a unit power factor which is a very important criterion during our comparison.

On the other hand, we can see in Fig. 8 VF-GVM-DPC which gives us the current and the voltage are in phase. Although there are still some low order harmonics, we can observe that they have a limited influence compared to that of Fig. 7. The oscillations of the vector component of the estimated flux are sinusoidal and out of phase without disturbance and fluctuation.

Figure 9 shows the bus voltage stabilizers at about minus 2 V and the system is operating at unity power factor.

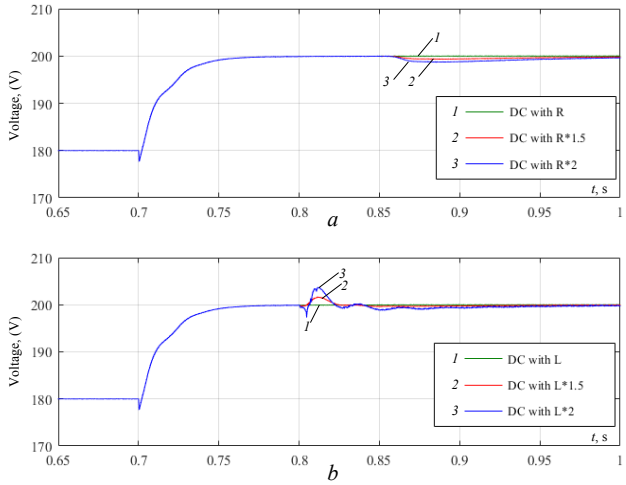

Fig. 9. System parameters influence on the evolution of the DC bus voltage: R (*a*); L (*b*)

Figure 10 shows the difference between the application of an SRF-PLL and a PLL which operates on the basis of a fuzzy logic controller to detect the fundamental frequency positive sequence component of the mains voltage in unbalanced and distorted conditions as well as fast and smooth tracking.

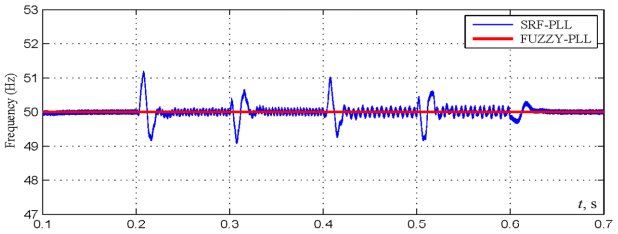

Fig. 10. The difference between Synchronous Reference Frame based Phase Locked Loop and proposed fuzzy-PLL

From Fig. 11 we can note that the THD rate of the network current has been improved compared to traditional control while respecting the standard of the electrical network. To highlight the contribution of the oscillatory terms, first of all, the results of the proposed control structure are shown in Fig. 2. The design and optimization process were carried out in the same manner as the procedure presented above. This result expressly shows how the components of the low order harmonics (5 and 7) with symmetrical and asymmetrical fault of the network voltage affect the network current. To summarize the results, Fig. 11 below presents an analysis based on the current THD of the VF-GVM-DPC strategies studied in this article.

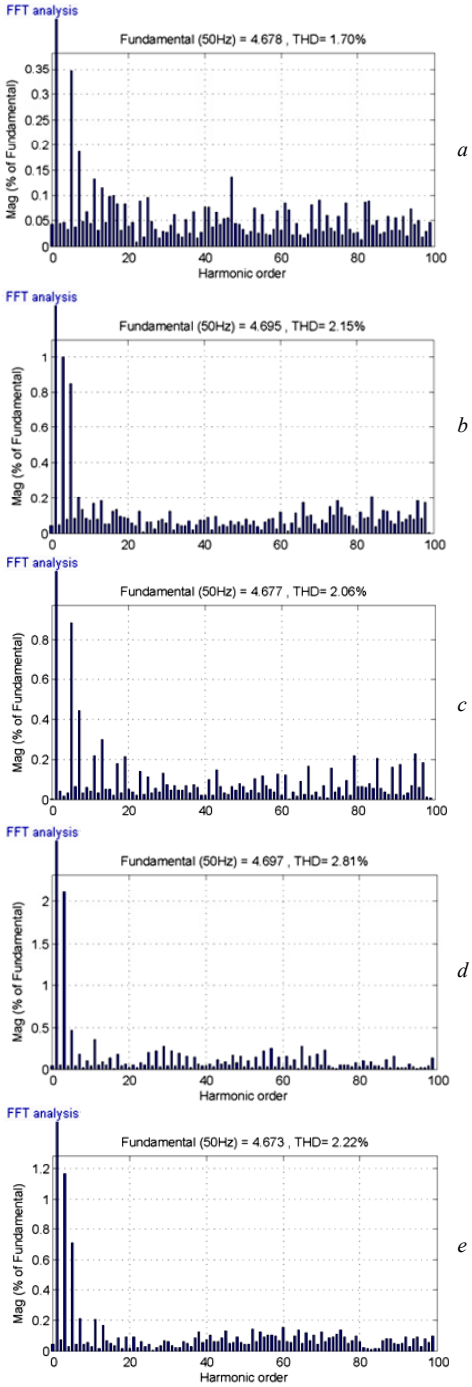

Fig. 11. Fast Fourier Transform analysis showing THD in source current of the proposed method:
a) ideal network voltage conditions;
b) unbalance and injection of the 7th order harmonic;
c) injection harmonics 5 and 7;
d) an asymmetrical disturbance with harmonics 5;
e) an asymmetrical disturbance with harmonics 5 and 7

4. Conclusions.

This paper presented the mathematical analysis and the numerical implementation of an improved method of Grid Voltage Modulated based on Direct Power Control or we introduced them for three phase rectifiers. The main objectives of the proposed control strategy are to obtain sinusoidal input currents under different input voltage conditions and to maintain the DC bus voltage at the level required as part of the improvement of the wind chain.

In these situations, harmonic components appear on the grid voltage, which causes distortion and current imbalance if the power reference is kept constant. However, the use of the proposed Virtual Flux-Grid Voltage Modulated method has the same control structure as the classic Grid Voltage Modulated, except for the use of virtual flux instead of voltages, which results in the optimization of the cost, since the voltage sensors will not be used, which is based on the principle of disturbance rejection, makes it possible to obtain an input current of low THD compared to the conventional method.

The proposed control method could offer many advantages and allows to obtain good performances with a THD of 1.7 % under ideal conditions and during disturbances it varies between 2.06 % to 2.81 % which respects the standard, without forgetting with a load lower calculation, without it being necessary to specify the power calculation term, nor to extract the positive / negative voltage sequence. We can therefore say that this control method is able to improve the quality of the input current.

Conflict of interest. The authors declare that they have no conflicts of interest.

REFERENCES

1. Bayoumi E.H.E. Power electronics in smart grid power transmission systems: a review. *International Journal of Industrial Electronics and Drives*, 2015, vol. 2, no. 2, p. 98. doi: https://doi.org/10.1504/ijied.2015.069784.

2. Akagi H., Watanabe E.H., Aredes M. *The Instantaneous Power Theory. In Instantaneous Power Theory and Applications to Power Conditioning* (eds H. Akagi, E.H. Watanabe and M. Aredes). 2017. doi: https://doi.org/10.1002/9780470118931.ch3.

3. Depenbrock M. *Direct self-control of the flux and rotary moment of a rotary-field machine*. US Patent no. 4678248A, Jul. 07, 1987. Available at: https://patentimages.storage.googleapis.com/89/13/c0/9d04c667c8003f/US4678248.pdf (accessed 14 March 2021).

4. Yousefi-Talouki A., Zalzar S., Pouresmaeil E. Direct Power Control of Matrix Converter-Fed DFIG with Fixed Switching Frequency. *Sustainability*, 2019, vol. 11, no. 9, p. 2604. doi: https://doi.org/10.3390/su11092604.

5. Berkani A., Bey M., Araria R., Allaoui T. A new approach based on Fuzzy-Q-Learning algorithm to control 3 level T-type voltage source converter. *Journal Européen des Systèmes Automatisés*, 2020, vol. 53, no. 6, pp. 845-852. doi: https://doi.org/10.18280/jesa.530610.

6. Chaoui A., Gaubert J.-P., Krim F. Power quality improvement using DPC controlled three-phase shunt active filter. *Electric Power Systems Research*, 2010, vol. 80, no. 6, pp. 657-666. doi: https://doi.org/10.1016/j.epsr.2009.10.020.

7. Laggoun Z.E.Z., Khalile N., Benalla H. A Comparative study between DPC-SVM and PDPC-SVM. *2019 International Conference on Advanced Electrical Engineering (ICAEE)*, 2019, pp. 1-5. doi: https://doi.org/10.1109/ICAEE47123.2019.9014796.

8. Malinowski M., Jasinski M., Kazmierkowski M.P. Simple direct power control of three-phase PWM rectifier using space-vector modulation (DPC-SVM). *IEEE Transactions on Industrial Electronics*, 2004, vol. 51, no. 2, pp. 447-454. doi: https://doi.org/10.1109/TIE.2004.825278.

9. Shang L., Hu J. Sliding-Mode-Based Direct Power Control of Grid-Connected Wind-Turbine-Driven Doubly Fed Induction Generators Under Unbalanced Grid Voltage Conditions. *IEEE Transactions on Energy Conversion*, 2012, vol. 27, no. 2, pp. 362-373. doi: https://doi.org/10.1109/TEC.2011.2180389.

10. Wai R., Yang Y. Design of Backstepping Direct Power Control for Three-Phase PWM Rectifier. *IEEE Transactions on*

Industry Applications, 2019, vol. 55, no. 3, pp. 3160-3173. doi: https://doi.org/10.1109/TIA.2019.2893832.
11. Bouafia A., Gaubert J., Krim F. Predictive Direct Power Control of Three-Phase Pulsewidth Modulation (PWM) Rectifier Using Space-Vector Modulation (SVM). *IEEE Transactions on Power Electronics*, 2010, vol. 25, no. 1, pp. 228-236. doi: https://doi.org/10.1109/TPEL.2009.2028731.
12. Norniella J.G., Cano J.M., Orcajo G.A., Rojas C.H., Pedrayes J.F., Cabanas M.F., Melero M.G. Multiple switching tables direct power control of active front-end rectifiers. *IET Power Electronics*, 2014, vol. 7, no. 6, pp. 1578-1589. doi: https://doi.org/10.1049/iet-pel.2013.0492.
13. Tao Y., Wu Q., Wang L., Tang W. Voltage sensorless predictive direct power control of three-phase PWM converters. *IET Power Electronics*, 2016, vol. 9, no. 5, pp. 1009-1018. doi: https://doi.org/10.1049/iet-pel.2014.0713.
14. Suul J.A., Luna A., Rodríguez P., Undeland T. Virtual-Flux-Based Voltage-Sensor-Less Power Control for Unbalanced Grid Conditions. *IEEE Transactions on Power Electronics*, 2012, vol. 27, no. 9, pp. 4071-4087. doi: https://doi.org/10.1109/TPEL.2012.2190301.
15. Ketzer M.B., Jacobina C.B. Virtual Flux Sensorless Control for Shunt Active Power Filters With Quasi-Resonant Compensators. *IEEE Transactions on Power Electronics*, 2016, vol. 31, no. 7, pp. 4818-4830. doi: https://doi.org/10.1109/TPEL.2015.2487298.
16. Laggoun Z.E.Z., Benalla H., Nebti K. Dual Virtual Flux-based Direct Power Control for rectifier under harmonically distorted voltage condition. *Archives of Electrical Engineering*, 2020, vol. 69, no. 4, pp. 951-966. doi: https://doi.org/10.24425/aee.2020.134641.
17. Gui Y., Kim C., Chung C.C., Guerrero J.M., Guan Y., Vasquez J.C. Improved Direct Power Control for Grid-Connected Voltage Source Converters. *IEEE Transactions on Industrial Electronics*, 2018, vol. 65, no. 10, pp. 8041-8051. doi: https://doi.org/10.1109/TIE.2018.2801835.

Received 15.10.2021
Accepted 18.11.2021
Published 03.12.2021

Zakaria El Zair Laggoun[1]*, PhD Student,*
Hocine Benalla[1]*, Doctor of Electrical Engineering, Professor,*
Khalil Nebti[1]*, PhD, MCA,*
[1] Laboratory of Electrotechnics of Constantine (LEC),
Mentouri Brothers University, Constantine 1,
Campus Ahmed Hamani Zerzara,
Route d'Ain el Bey, Constantine, 25000, Algeria,
e-mail:
zakaria-el-zair.laggoun@lec-umc.org (Corresponding author),
benalladz@yahoo.fr,
idor2003@yahoo.fr

How to cite this article:
Laggoun Z.E.Z., Benalla H., Nebti K. A power quality enhanced for the wind turbine with sensorless direct power control under different input voltage conditions. *Electrical Engineering & Electromechanics*, 2021, no. 6, pp. 64-71. doi: https://doi.org/10.20998/2074-272X.2021.6.09.

Матеріали приймаються за адресою:
Кафедра "Електричні апарати", НТУ "ХПИ", вул. Кирпичова, 21, м. Харків, 61002, Україна
Електронні варіанти матеріалів по e-mail: a.m.grechko@gmail.com

Довідки за телефонами: +38 050 653 49 82 Клименко Борис Володимирович
+38 067 359 46 96 Гречко Олександр Михайлович

Передплатний індекс: 01216